NATIONAL HELLENIC RESEARCH FOUNDATION

THEORETICAL AND PHYSICAL CHEMISTRY INSTITUTE

&

UNIVERSITY OF THE PELOPONNESE

SCHOOL OF ECONOMY, MANAGEMENT AND INFORMATICS

DEPARTMENT OF INFORMATICS AND TELECOMMUNICATIONS

THEORETICAL STUDY AND DEVELOPMENT OF PHOTONIC DEVICES AND SENSORS

by

Afroditi Petropoulou

Thesis submitted for the degree of Doctor of Philosophy

2020

ΕΘΝΙΚΟ ΙΔΡΥΜΑ ΕΡΕΥΝΩΝ

ΙΝΣΤΙΤΟΥΤΟ ΘΕΩΡΗΤΙΚΗΣ ΚΑΙ ΦΥΣΙΚΗΣ ΧΗΜΕΙΑΣ

&

ΠΑΝΕΠΙΣΤΗΜΙΟ ΠΕΛΟΠΟΝΝΗΣΟΥ

ΣΧΟΛΗ ΟΙΚΟΝΟΜΙΑΣ ΚΑΙ ΤΕΧΝΟΛΟΓΙΑΣ

ΤΜΗΜΑ ΠΛΗΡΟΦΟΡΙΚΗΣ ΚΑΙ ΤΗΛΕΠΙΚΟΙΝΩΝΙΩΝ

ΘΕΩΡΗΤΙΚΗ ΜΕΛΕΤΗ ΚΑΙ ΑΝΑΠΤΥΞΗ ΦΩΤΟΝΙΚΩΝ ΔΙΑΤΑΞΕΩΝ ΚΑΙ ΑΙΣΘΗΤΗΡΩΝ

Αφροδίτη Πετροπούλου

Διδακτορική Διατριβή

2020

Contents

Table of Figures

Acknowledgements

This thesis would not have been possible without the support of the organizations and the people around me. I would like to acknowledge the Theoretical and Physical Chemistry Institute of the National Hellenic Research Foundation (NHRF) for providing financial support during my studies as well as the host department (Department of Informatics and Telecommunications at University of the Peloponnese).

I would like to express my gratitude to my supervisor, Dr. Christos Riziotis, for his guidance and assistance throughout my Doctoral studies.

My sincere thanks also go to Dr. Grigoris Antonopoulos for his help in the experimental procedures and the constructive discussions on theoretical physics.

I would also like to thank Dr. George Kakarantzas for helping me with his laboratory experience.

Many thanks to Prof. Michalis N. Zervas for his advice and help on plasmonic devices during my visit to Optoelectronic Research Centre (ORC) and throughout my studies and to Prof. Dan Hewak for providing me the hybrid micro-fibers which were used for much experimental and theoretical work during my studies.

A very special thank to Prof. Dimitris Drikakis for the fruitful discussions about microfluidic phenomena.

I would also like to acknowledge Dr. Stergios Pispas and Prof. Efrosyni Themistou for providing me polymeric materials for my experimental work as well as useful discussions on chemical mechanisms and Prof. Thedora Krasia-Christoforou for the electrospun fiber samples and for the useful discussions during the experiments.

Last but not least I would like to thank my family and friends for their constant source of inspiration.

Abstract

In this thesis emerging photonic platforms based on either plasmonic structures or sensing schemes using functional polymeric materials are studied both theoretically and experimentally.

The first studied structure is metal-coated optical fiber tips with integrated plasmonic slot nanoresonators (PSNRs). The guiding and modal properties of metal-coated optical fiber tips with embedded PSNRs are investigated through Finite Element Method (FEM) simulations towards the identification of their optimization parameters. It was found that the placement of a PSNR at the cut-off radius of a metal-coated fiber tip, where the group velocity tends to zero, leads to considerable intensity enhancement of the field confined beyond the diffraction limit. Maximum intensity enhancement of optimally placed PSNRs at different radii shows a linear dependence between excitation wavelength and radius, making it feasible to engineer the proper radius for a specific wavelength for maximum enhancement.

The second studied plasmonic platform are metal tips which can offer high field intensity at the tip apex and high confinement on the nanoscale. The proposed platform based on hybrid composite glass metal microwires can offer robustness, ease of light coupling as well as continuous re-excitation of the plasmon modes due to repeated total internal reflection at the glass/air interface which can dramatically reduce the high losses induced by the metal core. An optimized fabrication process of high-quality all-fiber plasmonic tips by tapering such hybrid metal core/dielectric cladding microfibers is proposed and demonstrated experimentally. For this purpose the Plateau-Rayleigh instability in such hybrid fibers is theoretically investigated by inducing surface tension perturbations and by comparing them to the Tomotika instability theory. The continuous-core breakup time is calculated via FEM microfluidic simulations for different temperatures. The theoretical results are in close agreement with the experimental observations providing insight into the engineering of fibers, towards the development of plasmonic tips. Plasmonic tips were successfully demonstrated in a highly controllable manner, and their performance was related to simulation results predicting high field enhancement factors up to 10^5.

Optical fibers coated with novel polymers are also studied towards biosensing applications. The sensing mechanism is based on the variations of the measured power at the distal end of the fiber due to the interaction between the fiber's evanescent field and the changes induced to the polymeric film by the adsorption of the under study molecules. Two novel amphiphilic block copolymers, the cationic $PMMA_{117}$-b-$PDMAEMA_{16}$ and the cationic vinyl-sulfone functionalized $PMMA_{117}$-b-P($DMAEMA_{17}$-$VSTEMA_2$), having both hydrophobic poly(methyl methacrylate) (PMMA) and hydrophilic poly[2-(dimethylamino)ethyl methacrylate] (PDMAEMA) blocks have been designed and synthesized for efficient protein detection in photonic-based sensing. The presence of the cationic PDMAEMA block and the vinyl-sulfone double bonds led to reversible electrostatic binding of negatively charged proteins like bovine serum albumin (BSA) and non-reversible chemical binding by thiol-ene reactions with cysteine in proteins, respectively. The sensing properties of these materials were assessed and confirmed by ATR-FTIR analysis and by the characterization of fabricated sensing heads on silica optical fibers functionalized with suitably deposited overlayers. The

sensing assessment revealed the requirements for deposited overlayer characteristics towards proteins' detection sensitivity and selectivity enhancement.

The fabrication of cost-effective, polymer-based electrospun fluorescent fibrous grids and their evaluation as candidates for sensing is also reported. The formation of 3D grids can provide large interaction area with gas analytes and thus overcome quenching limitations induced by polymeric films, for more efficient sensing. Two different polymer-based electrospun fibers having fluorescent moieties were fabricated. The first was fabricated by a well-defined, methacrylic homopolymer functionalized with anthracene moieties as fluorescent elements that has been blended with a commercially available poly(methyl methacrylate) for the production of fluorescent electrospun polymer fibers. These materials have been evaluated for ammonia sensing based on the fluorescence quenching of the anthracene fluorophores in the presence of ammonia vapors, exhibiting fast response at concentration up to 10000 ppm. For the fabrication of the second fluorescent electrospun fiber system, ferrous core-shell nanoparticles consisting of a magnetic γ-Fe_2O_3 multi-nanoparticle core and an outer silica shell have been synthesized and covalently functionalized with Rhodamine B (RhB) fluorescent molecules (γ-Fe_2O_3/SiO_2/RhB NPs). The resulting γ-Fe_2O_3/SiO_2/RhB NPs were integrated with a renewable and naturally-abundant cellulose derivative (i.e. cellulose acetate, CA) that was processed in the form of electrospun fibers to yield multifunctional fluorescent fibrous nanocomposites. The encapsulation of the nanoparticles within the fibers and the covalent anchoring of the RhB fluorophore onto the nanoparticle surfaces prevented the fluorophore’s leakage from the fibrous mat, enabling thus stable fluorescence-based operation of the developed materials. These materials were further evaluated as dual fluorescent sensors (i.e. ammonia gas and pH sensors), demonstrating consistent response for very high ammonia concentrations (up to 12000 ppm) and fast and linear response in both alkaline and acidic environments. The superparamagnetic nature of embedded nanoparticles provides means of electrospun fibers morphology control by magnetic field-assisted processes and additional means of electromagnetic-based manipulation making possible their use in a wide range of sensing applications.

Περίληψη

Στην παρούσα διδακτορική διατριβή μελετώνται θεωρητικά και πειραματικά καινοτόμες φωτονικές πλατφόρμες που βασίζονται είτε σε πλασμονικές δομές είτε σε συστήματα αισθητήρων που χρησιμοποιούν λειτουργικά πολυμερικά υλικά. Η πρώτη δομή που μελετάται είναι οπτικές ίνες κωνικής δομής επικαλυμμένες με λεπτό στρώμα μετάλλου. Η ενσωμάτωση στον μανδύα μιας μικρής επιφανειακής ασυνέχειας (Plasmonic Slot Nano-Resonators - PSNRs), η οποία μπορεί να έχει μία ποικιλία σχημάτων, προκαλεί τη συγκέντρωση του πεδίου στην ασυνέχεια αυτή λόγω πλασμονικού συντονισμού με αποτέλεσμα να ενισχυθεί η έντασή του μερικές τάξεις μεγέθους. Οι ιδιότητες των τρόπων διάδοσης σε αυτές τις δομές διερευνώνται μέσω προσομοιώσεων με μέθοδο πεπερασμένων στοιχείων (Finite Element Method - FEM) για τον προσδιορισμό των παραμέτρων βελτιστοποίησής τους. Διαπιστώθηκε ότι η τοποθέτηση ενός PSNR στην ακτίνα αποκοπής μίας επιστρωμένης με μέταλλο οπτικής ίνας κωνικής δομής, όπου η ομαδική ταχύτητα τείνει στο μηδέν, οδηγεί σε σημαντική ενίσχυση της έντασης του πεδίου. Η μέγιστη ένταση του πεδίου εντός των PSNRs παρουσιάζει γραμμική εξάρτηση μεταξύ του μήκους κύματος διέγερσης και της ακτίνας της οπτικής ίνας όπου είναι τοποθετημένο το PSNR, καθιστώντας εφικτή την επιλογή της κατάλληλης ακτίνας για την τοποθέτησή του για ένα συγκεκριμένο μήκος κύματος διέγερσης προκειμένου να επιτευχθεί η μέγιστη ενίσχυση του πεδίου.

Η δεύτερη πλασμονική δομή που μελετήθηκε είναι μεταλλικές ακίδες που μπορούν να προσφέρουν υψηλή ένταση πεδίου στην κορυφή τους. Η προτεινόμενη πλατφόρμα που βασίζεται σε υβριδικές μικροΐνες γυάλινου μανδύα-μεταλλικού πυρήνα παρέχει μηχανική αντοχή και επιτρέπει την επαναδιέγερση των πλασμονικών κυμάτων λόγω ολικής ανάκλασης στην διεπιφάνεια γυαλιού/αέρα με αποτέλεσμα να μειώνονται δραματικά οι υψηλές απώλειες που προκαλούνται από τον μεταλλικό πυρήνα. Μια βελτιστοποιημένη διαδικασία κατασκευής υψηλής ποιότητας πλασμονικών ακίδων μπορεί να επιτευχθεί με λέπτυνση των ινών με θέρμανση και ταυτόχρονο εφελκυσμό ώστε να δημιουργηθούν περιοχές μειούμενης διαμέτρου. Για το σκοπό αυτό, η αστάθεια Plateau-Rayleigh σε τέτοιες υβριδικές ίνες διερευνάται θεωρητικά μέσω προσομοιώσεων FEM για διαφορετικές θερμοκρασίες και συγκρίνεται με τη θεωρία αστάθειας του Tomotika ώστε να υπολογιστεί ο χρόνος διάσπασης του συνεχούς πυρήνα. Τα θεωρητικά αποτελέσματα είναι σε συμφωνία με τις πειραματικές παρατηρήσεις και παρέχουν γνώση της μηχανικής των υβριδικών αυτών ινών για την ανάπτυξη πλασμονικών ακίδων. Οι πλασμονικές ακίδες αναπτύχθηκαν επιτυχώς με ελεγχόμενο τρόπο και η απόδοσή τους συγκρίνεται με τα αποτελέσματα των προσομοιώσεων που προβλέπουν υψηλούς συντελεστές ενίσχυσης του πεδίου έως 10^5.

Οπτικές ίνες επικαλυμμένες με καινοτόμα πολυμερή μελετώνται επίσης για την ανάπτυξη βιο-αισθητήρων. Ο μηχανισμός ανίχνευσης βασίζεται στις μεταβολές της μετρούμενης

ισχύος στο απομακρυσμένο άκρο της ίνας λόγω της αλληλεπίδρασης μεταξύ του αποσβενυόμενου πεδίου της ίνας και των αλλαγών που προκαλούνται στο πολυμερικό στρώμα λόγω της προσρόφησης των υπό μελέτη μορίων. Δύο νέα αμφίφιλα συμπολυμερή κατά συστάδες, το κατιονικό $PMMA_{117}$-b-$PDMAEMA_{16}$ και το κατιονικό $PMMA_{117}$-bP ($DMAEMA_{17}$-$VSTEMA_2$), που έχουν τόσο υδρόφοβο πολυ(μεθακρυλικού μεθυλεστέρα) (PMMA) όσο και υδρόφιλο πολυ(μεθακρυλικός εστέρας της 2-διμεθυλαμινο αιθανόλης) (PDMAEMA) σχεδιάστηκαν και συντέθηκαν για την ανίχνευση πρωτεϊνών. Η παρουσία του κατιονικού μέρους PDMAEMA και των διπλών δεσμών βινυλοσουλφόνης επιτρέπει την αναστρέψιμη ηλεκτροστατική προσρόφηση αρνητικά φορτισμένων πρωτεϊνών όπως η bovine serum albumin (BSA) καθώς και τη μη αναστρέψιμη χημική σύνδεση λόγω αντίδρασης της θειολίνης με την κυστεΐνη των πρωτεϊνών, αντίστοιχα. Η ικανότητα ανίχνευσης αυτών των υλικών αξιολογήθηκε και επιβεβαιώθηκε τόσο με ανάλυση ATR-FTIR όσο και με τον χαρακτηρισμό οπτικών ίνων πυριτίας επικαλυμμένες με λεπτό στρώμα συμπολυμερούς.

Μελετήθηκε επίσης η κατασκευή πλεγμάτων μικρο-ινών φθορισμού από πολυμερή και ο χαρακτηρισμός τους ως αισθητήρες. Ο σχηματισμός τρισδιάστατων πλεγμάτων ινών προσφέρει μεγάλη περιοχή αλληλεπίδρασης με τα προς ανίχνευση μόρια και έτσι μπορούν να ξεπεραστούν οι περιορισμοί κορεσμού που παρατηρούνται σε πολυμερικές επιφάνειες με συνέπεια την ανάπτυξη πιο αποτελεσματικών αισθητήρων. Αναπτύχθηκαν δύο διαφορετικά πλέγματα μικρο-ινών με βάση πολυμερή που περιείχαν φθορίζουσες ουσίες. Το πρώτο κατασκευάστηκε από ένα καλά καθορισμένο μεθακρυλικό ομοπολυμερές που περιείχε ανθρακένιο ως φθορίζουσα ουσία για την παραγωγή πλέγματος φθοριζόντων ινών πολυμερούς. Αυτά τα υλικά χαρακτηρίστηκαν ως προς την ανίχνευση αμμωνίας και παρουσίασαν γρήγορη απόκριση σε συγκέντρωση έως 10000 ppm ατμών αμμωνίας. Για την κατασκευή του δεύτερου φθορίζοντος πλέγματος μικρο-ινών συντέθηκαν νανοσωματίδια (NPs) πυρήνα σιδήρου-κελύφους πυριτίας που αποτελούνται από πολυ-νανοσωματιδιακό μαγνητικό πυρήνα γ-Fe_2O_3 και εξωτερικό κέλυφος πυριτίας και συνδέονται ομοιοπολικά με φθορίζοντα μόρια ροδαμίνης Β (RhB) (γ-Fe_20_3/SiO_2/RhB NPs). Τα προκύπτοντα γ-Fe_2O_3/$Si0_2$/RhB NPs ενσωματώθηκαν σε ένα ανανεώσιμο και φυσικά άφθονο παράγωγο κυτταρίνης (οξική κυτταρίνη - CA) το οποίο χρησιμοποιήθηκε για την κατασκευή πλεγμάτων μικρο-ινών φθορισμού. Η ενσωμάτωση των νανοσωματιδίων εντός των ινών και η ομοιοπολική σύνδεση του Rhb στις επιφάνειες των νανοσωματιδίων εμποδίζουν τη διαρροή της φθορίζουσας ουσίας από το ινώδες πλέγμα, επιτρέποντας έτσι τη σταθερή λειτουργία φθορισμού των αναπτυγμένων υλικών. Η απόδοση των υλικών αυτών αξιολογήθηκε τόσο ως προς την ανίχνευση αέριας αμμωνίας όσο και για τη μέτρηση pH, επιδεικνύοντας συνεπή απόκριση σε πολύ υψηλές συγκεντρώσεις αμμωνίας (μέχρι 12000 ppm) και γρήγορη και γραμμική απόκριση σε αλκαλικά και όξινα περιβάλλοντα. Επιπλέον η μαγνητική φύση των ενσωματωμένων νανοσωματιδίων παρέχει τη δυνατότητα ελέγχου της μορφολογίας των πλεγμάτων μικρο-ινών με την εφαρμογή εξωτερικού μαγνητικού πεδίου καθιστώντας δυνατή τη χρήση τους σε ένα ευρύ φάσμα εφαρμογών ανίχνευσης.

Principal Abbreviations

2D	Two Dimensional
3D	Three Dimensional
ATR	Attenuated Total Reflection
BSA	Bovine Serum Albumin
CA	Cellulose Acetate
DLS	Dynamic Light Scattering
FEM	Finite Element Method
FIB	Focused Ion Beam
FTIR	Fourier-Transform Infrared Spectroscopy
GPC	Gel Permeation Chromatography
NMR	Nuclear Magnetic Resonance
NP	Nanoparticle
PDI	Polydispersity Index
PEC	Perfect Electric Conductor
PML	Perfectly Matched Layer
PNR	Plasmonic Nano-Resonators
PR	Plasmon Resonance
PRI	Plateau-Rayleigh Instability
PSNR	Plasmonic Slot Nano-Resonators
RAFT	Reversible Addition-Fragmentation Chain Transfer
RhB	Rhodamine B
SBC	Scattering Boundary Condition
SEM	Scanning Electron Microscopy
SERS	Surface-Enhanced Raman Spectroscopy
SPP	Surface Plasmon Polariton
TE	Transverse Electric
TEM	Transmission Electron Microscopy
THF	Tetrahydrofuran
TM	Transverse Magnetic

Symbols

d, D	Diameter
E_f	Enhancement Factor
I	Intensity
k	Wavenumber
M_n	Molecular Weight
M_s	Magnetization
n	Refractive Index
n_{eff}	Effective Refractive Index
r, R	Radius
s	Surface Tension
u_g	Group Velocity
u_{ph}	Phase Velocity
z_b	Beat Length Between Two Modes
z_t	Characteristic Taper Length
α	Semi-Angle
β	Propagation Constant
ε	Relative Permittivity
θ	Angle of Incidence
θ_c	Critical Angle
λ	Wavelength
λ_c	Capillary Length
μ	Viscosity
τ_B	Breakup Time

Chapter 1

Introduction

1.1 Overview

In recent years, photonic devices and sensors have attracted much attention and have been widely used due to their unique properties. Photonic sensing covers a wide range of technology operational principles, from free space optical sensors, where the optical signal is propagated freely in the propagation medium, waveguide and fiber based sensors, plasmonic sensors as well as other categories like fluorescent and photoluminescent sensors by indirect laser illumination. The photonic sensors rely on the interaction of light with the environment and the measurement of the resulting change in its characteristics. A measurable parameter of photonic sensors may be the change in intensity, wavelength, polarization, or light phase. The use of photonic devices offers a number of advantages such as tolerance to electromagnetic fields, reliability, ability to operate in hazardous environmental conditions that may include explosive or flammable materials, fast response, sensitivity and a large dynamic response range.

The development of novel nanocomposite materials and customizable polymers has allowed the enhancement of photonic sensing by combining such unique materials with suitable hosting photonic structures. For the development of high performance photonic devices with improved functionality the design of customized photonic structures suitable for specific applications is needed. The sensing performance relies both on the photonic structure inherent optical properties and sensitivity but also on the functionalization by sensitive materials that improve also the selectivity of sensing. This combination of customizable structures with novel materials is crucial for the development of high performance sensors for specific applications. The scope of this thesis is to study specific examples of such sensors demonstrating the design, fabrication and functionalization of photonic sensors towards real and demanding applications. In brief the thesis covers a wide range of devices development based on plasmonic structures, optical fibers functionalized with polymer materials, and fluorescent based sensors integrated in electrospun fiber grids. Within this work there have been identified suitable photonic structures of high inherent sensitivity as well as materials that could enable selective. For practical reasons it was chosen to

characterize the sensing performance of materials in rather simple architectures with low interrogation complexity (such as multimode fibers or free space fluorescent materials). However the ultimate scope which could be facilitated in future studies would be the combination of herein developed and identified materials with appropriate optimized photonic structures identified also in this study.

The thesis is divided in three main parts. In the first part the development of optical fiber sensors based on plasmonic structures is studied both theoretically and experimentally. Plasmonic devices can be used to develop highly sensitive sensors as the propagating plasmonic modes are highly sensitive to any changes in the dielectric/metal interface as a result of molecule adsorption. The advantages of such structures are the high enhancement and concentration of the electromagnetic field below the light diffraction limit. Many plasmonic devices have been studied, most of which have as main drawbacks the difficulty of both their fabrication and the excitation of the plasmon waves. In order to avoid the above difficulties, the devices proposed here are based on metal/glass composite optical fibers in which either the cladding or the core is made of metal. The greatest advantage of these structures is that plasmonic propagating modes can be easily excited by connecting the end of the optical fiber to a light source using appropriate optical elements. These devices have mechanical strength and provide flexibility and integration capability in sensor circuits.

The second part of this thesis focuses on the characterization and application of novel polymeric materials for protein detection. Polymeric materials that are appropriately designed to be able to adsorb the substance to be detected can be developed to implement photonic sensors. For the study of the sensitivity, linearity and selectivity of the materials, they can either be adapted to commercially available optical fibers and flat waveguides, whereby the uptake of the molecules to be detected can alter the waveguiding and propagation properties.

The third part is devoted to a new class of fluorescent sensors based on electrospun micro/nano fiber grids. Such composite polymeric materials can be doped with a number of fluorescent moieties and provide a highly enhanced surface to volume ratio, significantly improving the sensitivity. Such electrospun materials can be also integrated in plasmonic structures, optical fibers and integrated circuits for the development of sensors with low detection limits.

1.2 Plasmonic structures

The field of plasmonics has attracted great interest in the last decades as it offers high field confinement beyond the diffraction limit. Light is limited by diffraction and it cannot be confined tighter than to a length of $\lambda/2$ in each direction [1]. Surface Plasmon Polaritons (SPPs) are surface electromagnetic waves coupled to the collective

oscillations of free electrons in a conductor. SPPs have been studied for many different nano-structured metal systems such as plane metal/dielectric interfaces [2], [3], thin dielectric/metal/dielectric interfaces [4], [5] and thin cylindrical shells [6], [7] which support a number of symmetric and anti-symmetric modes. SPPs excitation is polarization dependent and has been used successfully for developing high performance polarizers [8], as well as, refractometric- [9] and bio- [10]–[13] sensors. Furthermore the high field enhancement and localization that can be achieved have found many applications, such as Surface-Enhanced Raman Spectroscopy (SERS) [14], data-storage [15] and microscopy [16].

Subwavelength-sized metallic apertures can excite Localized Surface Plasmon Resonances (LSPRs) providing high light confinement and spatial resolution [17]. The optical properties of the Plasmon Resonances (PRs) are determined by the geometry of the nanostructure and by the permittivities of both the metal and the surrounding dielectric. These Plasmonic Nano-Resonators (PNRs) can have a variety of shapes, such as square, rectangular, circular and bow-tie. When such structures are embedded in thin metal films they form Plasmonic Slot Nano-Resonators (PSNRs) which can provide a strong 3D light concentration [18], [19]. Another crucial factor for determining the performance of plasmonic systems is the propagation losses which occur due to the metal absorption. So a balance between field confinement and losses must be found in order to design an optimum plasmonic structure. The integration of PSNRs in tapered optical fibers coated with thin metallic films offer ease of excitation of the PRs as well as high field intensity close to the fiber's cut-off radius.

Metal tips are another type of very promising nanofocusing structure that has been studied extensively [20]–[23] since they enable the confinement of light at the tip apex providing strong field localization. Metal tips having dielectric cladding fabricated by tapering hybrid metal core/glass cladding microfibers have several advantages over pure metal tips. The glass cladding not only mechanically supports the metal core but also offers ease of coupling light into the device. Furthermore due to the total internal reflections at the glass/air interface the plasmon modes travelling along the metal/dielectric interface are continuously re-excited [24]. The re-excitation of the plasmon modes is crucial for limiting the losses induced by the metal.

1.2.1 Tapered optical fibers

Optical fiber tapers are fabricated by stretching optical fibers while heating them, reducing their diameters to the micron or submicron scale. In such ultrathin fibers the optical field can extend far from the fiber surface enabling its interaction with the environment.

The fabrication of adiabatic optical fiber tapers with well-defined geometrical characteristic is crucial in order to obtain low-loss tapers. Several techniques have

been developed for the fabrication of tapered optical fibers such as the hydrofluoric (HF) etching method [25], the flame-heated fiber drawing method using a sapphire fiber taper [26], and heating and stretching method using a CO_2 laser beam [27] or a flame [28], [29] as heat source.

In this thesis the heating and stretching method using a flame was adopted for the fabrication of the optical fiber tapers. The two fiber ends are placed at two elongation stages, inside optimum sized grooves. A third stage holding the flame is moving across the fiber axis over several millimetres to heat the fiber. The flame is produced by a butane-oxygen mixture while two flow controllers are used to control the flow rates of the gases. A schematic representation of the setup is given in Figure 1-1. Schematic representation of the tapering setup.

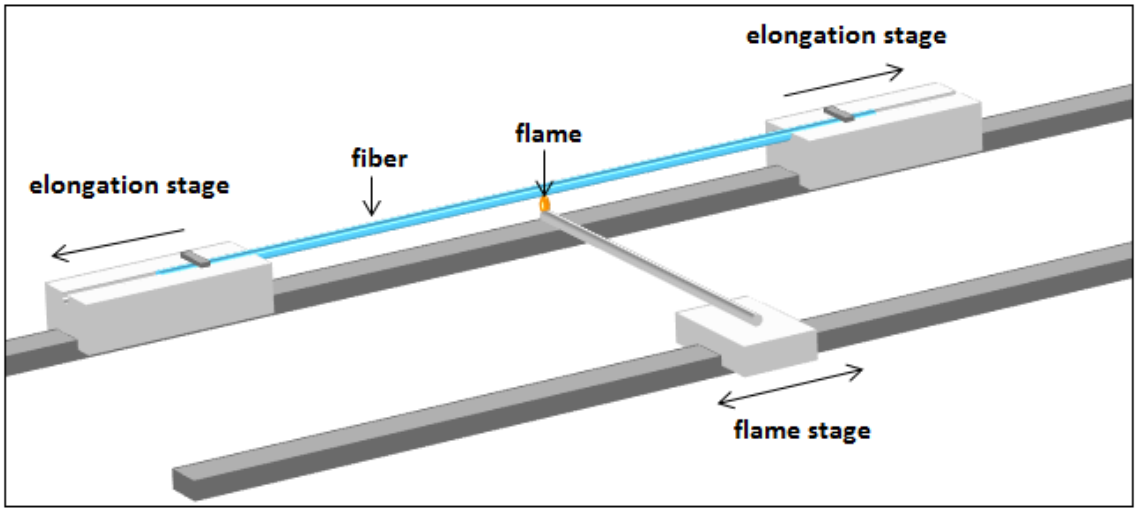

Figure 1-1. Schematic representation of the tapering setup.

This flame brushing technique has several advantages over other tapering methods. Firstly long tapers with high uniformity can be obtained with minimum losses as it offers accurate control of the pull rate and the flame's movement. Furthermore the pigtails at both fiber ends can be kept enabling the connection of the taper with other optical components compared to the drawing method using a sapphire fiber taper. Also for optical fibers combining different types of materials like glasses and metals, other methods such as stretching using a CO_2 laser beam are not suitable due to the reflectivity of the metals.

Although the flame brushing technique is appropriate for multi-material systems in the high temperatures needed for the tapering it is commonly observed the breakup of the core and the consequent formation of spheres and thus the temperature profile must be carefully controlled. This breakup is attributed to the *Plateau-Rayleigh Instability* (PRI) which grows in the low viscosities regime limiting the reduction of fibers'

diameters below a few microns. The study of the instabilities induced by the temperature profile, such as perturbation wavelength and width in the case of static heating can be used as a guide for the fabrication of fibers with the desirable characteristics. Furthermore the time that a part of the fiber remains under the influence of the perturbation is an important parameter for the stability of the metal core.

1.3 Polymeric materials as optical fiber overlayers

Polymers are a promising and widely used material platform for functional devices development. Despite the different approaches, quite often the increased cost and operational complexity limits the applicability of sensors in real applications. The deployment of polymers with electronic or photonic platforms has allowed the development of a number of cost-effective devices and sensors [30], [31]. In sensing technology functional polymers are usually employed as uniform layers or overlayers forming sensitive responsive surfaces to certain measurands. In photonics which is an emerging and highly promising field for devices development, this can be achieved either in fiber or integrated optical technology [32], [33] or even in free space optical architectures in the form of diffraction gratings [33]–[35]. The polymeric overlayer interacts by its surface with the measurand or even by volume by allowing adsorption of measurands within the polymer. This approach has led to the design and synthesis of functional materials that offer selectivity as well as efficient adsorption of the molecules under study, enhancing the sensitivity [36], [37]. The combination of the sensing material and a large core optical fiber provide additionally flexibility, mechanical robustness, high degree of miniaturization, as well as long interaction length where their operational characteristics can allow the efficient integration of sensors in measuring units. The deposition of such materials to an unclad portion of multimode polymer [38], [39] or silica [40], [41] optical fiber, which can act as both the sensing and collection element, can result to the development of low cost and low complexity sensors. The selection also of proper interrogation schemes like optical power interrogation in contrast to spectral based detection [41] offers the additional capability of sensing heads integration in autonomous wireless networks for increased monitoring flexibility [42].

The sensing mechanism of the polymer coated optical fibers is based on the variations of the measured power at the distal end of the fiber due to the interaction between the fiber's evanescent field and the changes induced to the polymeric film by the adsorption of the under study molecules (Figure 1-2). The measured power differs when the fiber is immersed to solutions of different concentrations of the measurand enabling a quantitative evaluation of the concentration.

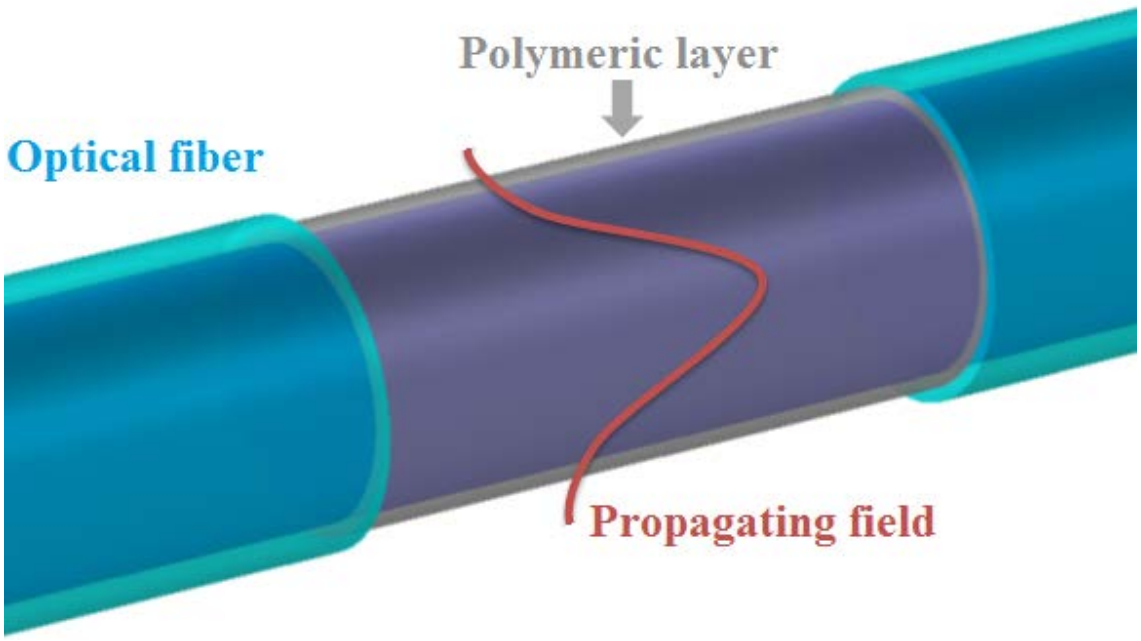

Figure 1-2. The propagating field in a polymer coated portion of an optical fiber.

Evanescent wave optical fiber sensors rely on the mechanism of total internal reflection. When the refractive index (n_2) of the medium surrounding the fiber's core is lower than the core's refractive index (n_1), rays with angles of incidence $\theta > \theta_c$, where $\theta_c = \sin^{-1}(n_2/n_1)$, are reflected and transmitted inside the core. Although light is totally reflected a small portion of the field expands into the surrounding medium and its amplitude decays exponentially with the distance from the boundary (Figure 1-3 (a)). Other geometries of the fiber like U-bend fibers (Figure 1-3 (b)) are also proposed in order to increase the penetration depth of the field and consequently the sensor's sensitivity [43].

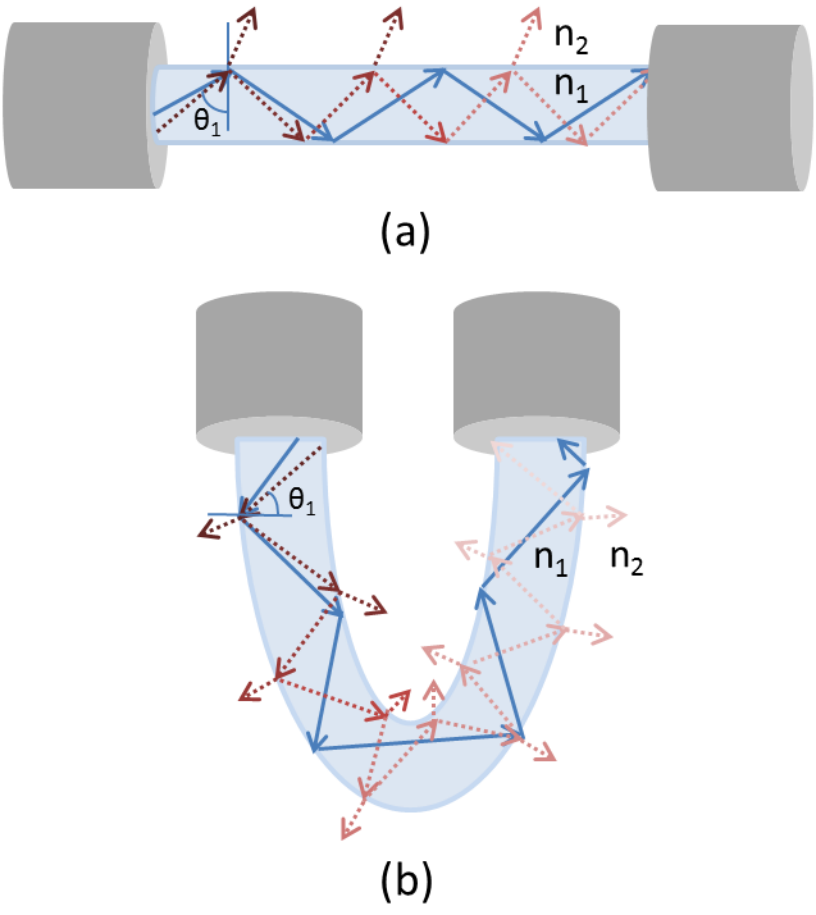

Figure 1-3. Evanescent field of a straight (a) and bend (b) de-clad fiber.

Many polymeric materials though have higher refractive index than silica. In this case where $n_{pol}>n_{core}$ and $n_{pol}>n_{sur}$, with n_{pol}, n_{core} and n_{sur} being the refractive indices of the polymer, core and surrounding medium, respectively, the sensor works in the leaky mode. When the following condition is satisfied

$$\theta_{cII} = sin^{-1}\left(\frac{n_{sur}}{n_{pol}}\right) < \varphi = sin^{-1}\left(\frac{n_{core}}{n_{pol}}\sin(\theta)\right) < \theta_{cI} = sin^{-1}\left(\frac{n_{core}}{n_{pol}}\right)$$

where θ_{cI} and θ_{cII} are the critical angles at the core/polymer and polymer/surrounding medium interfaces, respectively, the refracted beam on the polymeric layer will reflect on the polymer/surrounding medium interface and refract from the core/polymer interface and thus the incident beam with angle θ will propagate again in the core with an angle ψ [44]. Figure 1-4 shows the paths of the reflected and refracted beams.

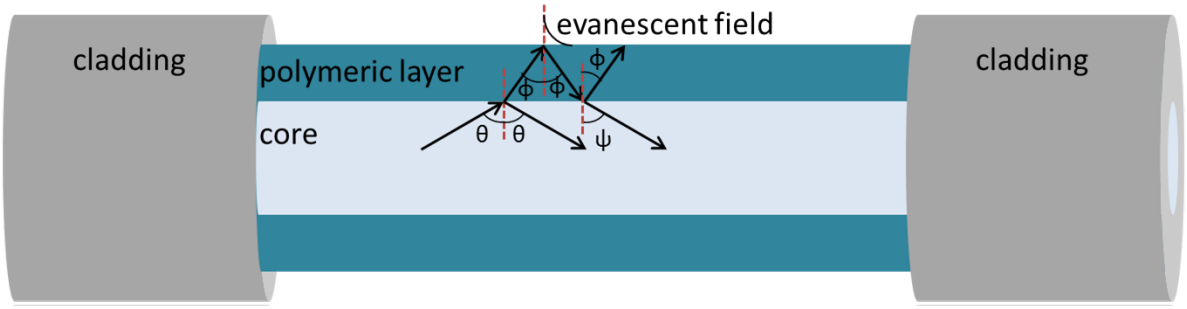

Figure 1-4. Evanescent wave optical fiber sensor with $n_{pol}>n_{core}$.

1.4 Electrospun polymers

Polymers can also be used as sensors in the form of nanofibrous system developed via electrospinning technique [45]–[48]. Electrospinning is a widely used and simple technique employed for the production of polymeric nano- and microfibers with potential applications in many scientific fields. Due to the high surface-to-volume ratio high concentrations of the measurand can be detected since the fast quenching of the system is limited. Nanofibrous materials developed using this technique can form truly 3D grids of large area that can overcome the above-mentioned interaction area limitations [49]. However this can happen at the expense of control of uniformity which is critically important at certain architectures in fiber and integrated photonics where waveguiding conditions must be controllable. However the 3D grid could be a promising candidate ideally suited for free space architectures in contrast to diffraction based remote sensors which form a special class of sensors for certain demanding applications. The further functionalization of those 3D grids with fluorescent moieties towards fluorescent-based detection can dramatically enhance their sensitivity and resolution providing extremely low detection limits. Interactions between fluorescent moieties and analytes change the transmission of the fluorescence signal and can be easily detected by a simple and low cost optical system.

A schematic representation of the electrospinning setup is given in Figure 1-5. The polymeric solution is inserted in a syringe which is placed in a syringe pump that controls the flow rate. A high voltage (10-50 kV) is applied to the syringe needle in order to initiate the ejection of the polymeric solution. The electrical forces stretch the viscoelastic polymeric solution and start to counteract its surface tension. At a critical point, known as Taylor cone, the liquid erupts forming a liquid jet. A grounded target is used to collect the produced fibers. In order to obtain continuous and smooth fibers with the desirable diameters the following parameters should be controlled:

- The polymeric parameters (molecular weight, concentration, viscosity, etc.)

- Applied voltage
- The flow rate
- The needle gauge
- The needle-to-collector distance

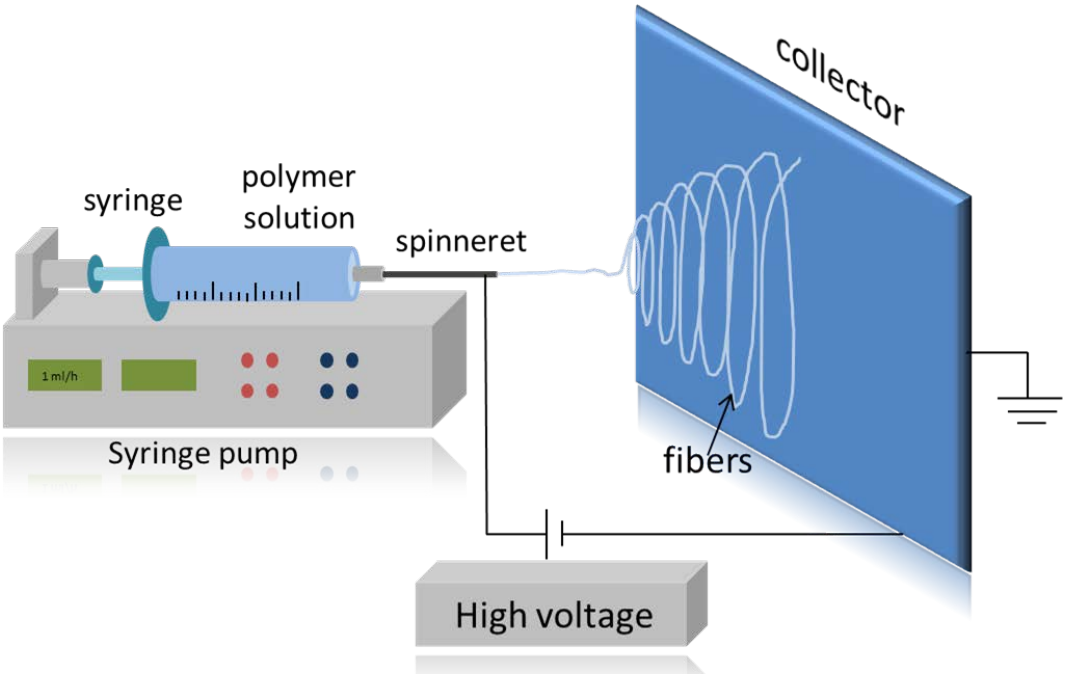

Figure 1-5. Schematic of an electrospinning setup.

Electrospun fibers can be used for coating an optical fiber segment for the development of an evanescent optical fiber sensor that combines the low complexity and cost of optical fiber sensors with the high surface-to-volume ratio of electrospun fibers. For the fabrication of this platform the optical fiber should be placed between the needle and the collector and with direction perpendicular to the syringe [50]. By rotating the optical fiber with the appropriate velocity uniform coating can be achieved along the sensing region of the fiber (Figure 1-6).

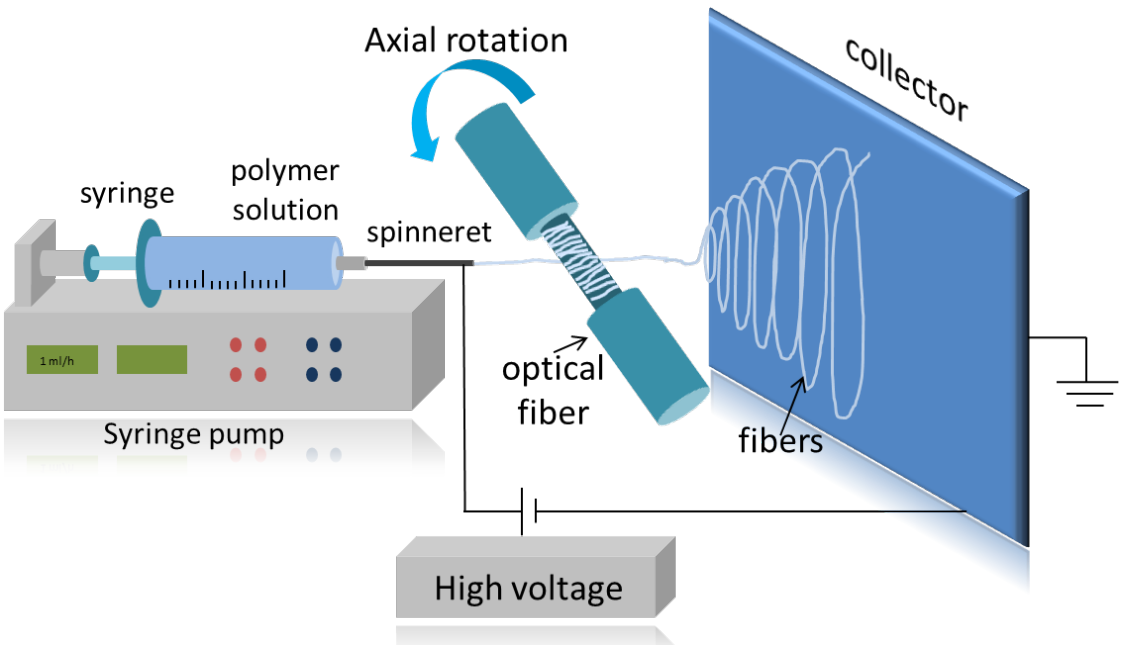

Figure 1-6. Schematic of an electrospinning setup with a rotating optical fiber for uniform coating of an optical fiber segment with electrospun fibers.

1.5 Outline

Chapter 2 presents an investigation of gold-coated fiber tips with embedded *Plasmonic Slot Nano-Resonators* (PSNRs). In section 2.2 the variation of the effective refractive index (n_{eff}) of the core modes as a function of the metal thickness and the radius of the dielectric core and their evolution from core to plasmon modes is studied. In section 2.3 we present the calculated intensity enhancement factors (E_f) of gold-coated optical fiber tips and we confirm the predicted cut-off radius of the structure. Finally, in section 2.4 we simulate gold-coated optical fiber tips of different geometrical characteristics with embedded PSNRs at different radii and we calculate the intensity enhancement factors (E_f) in order to find the optimum position for the PSNR.

In chapter 3 plasmonic tips fabricated by tapering metal core/glass cladding microfibers are studied both theoretically and experimentally. The heating and stretching method [29], [51] was used for the tapering process in order to obtain smooth tips with small semi-angles. The fabricated tips are optically characterized and their modal characteristics are compared to the simulations results. 3D simulations were also performed for the calculation of the E_f at the apex of the tip. The tapering process was further investigated through microfluidics simulations for the determination of the appropriate tapering conditions to avoid the breakup of the metal core.

In chapter 4 the synthesis of novel amphiphilic block copolymers having both hydrophobic poly(methyl methacrylate) (PMMA) and hydrophilic poly[2-(dimethylamino)ethyl methacrylate] (PDMAEMA) blocks is reported. The sensing mechanism of proteins based on the intrinsic polymers' properties is also presented, followed by the sensors development process and the deposition characteristics of overlayers regarding their surface and adhesion properties. The sensing ability and hence, the overall performance of the fiber sensors is examined.

The fabrication of electrospun microfibers functionalized with fluorescent molecules is reported in chapter 5. In section 5.1 a well-defined poly(9-anthrylmethyl methacrylate) homopolymer (PAnMMA) possessing anthracene side-chain moieties has been used in the fabrication of anthracene-containing electrospun fluorescent fibrous mats. In section 5.2 ferrous core-shell nanoparticles consisting of a magnetic γ-Fe_2O_3 multi-nanoparticle core and an outer SiO_2 shell have been synthesized and further functionalized with Rhodamine B (RhB) fluorescent molecules. The latter were covalently bound in the matrix of the silica shell. The resulting RhB-functionalized ferrous nanoparticles were further incorporated within cellulose acetate (CA) electrospun fibers to yield fluorescent electrospun fibrous nanocomposites. The sensing performance of both fabricated electrospun fibers was evaluated.

Chapter 2

Design Optimization of Gold-Coated Fiber Tips with Embedded Plasmonic Slot Nano-Resonators

2.1 Introduction

Optical fibers comprise a platform that could be adapted for the development of plasmonic devices [52], [53], combining also the ease of light coupling and thus allowing better operational characteristics. Such an optical fiber platform implemented in a tapered optical fiber with a thin metallic cladding is studied in this chapter. Along the metal-dielectric interface surface bound modes can propagate, while by embedding morphological singularities these modes can be spatially confined to localized surface plasmons leading to field enhancement. Previous works have demonstrated the operation of such plasmonic devices [18], [54]–[56] however there are still a number of optimization issues, regarding the geometrical characteristics of the metal coated fiber tips that need to be studied in order to gain better understanding and provide better performance of the platform.

In this work the metal-coated fiber tips are modelled by FEM analysis and the corresponding values of cut-off radius are calculated. By inserting a PSNR at the cut-off radius high field intensity can be obtained since the highest confinement and intensity enhancement of light is expected at the position where the group velocity (u_g) tends to zero. Since the fiber surface corresponding to cut-off radius is rather limited, the size, shape and arrangement options of the PSNR are also restricted. This limitation can be overcome by embedding the PSNR at the tip's sidewall instead of the tip apex. Our work focus on thin gold-coated fiber tips and relies on the combined effects of the field enhancement associated with the plasmonic cut-off and the field enhancement associated with the PSNR resonances in order to get the maximum E_f. In previous works [54]–[56], due to larger diameters, there is no cut-off of the propagating modes and the enhancement is entirely due to the resonator resonances at the end of the tip where the tip serves merely to deliver the power and excite the resonator. Besides, due to the propagating cut-off mode inside the structure the tip only experiences its evanescent tail. Thus, by integrating a resonator at the tip sidewall and at the cut-off

radius, maximum enhancement can be achieved improving the overall performance of the structure.

2.2 Metal coated microfibers

The simulation studies were performed on suitably short length tapered sections of a typical single mode SMF28 optical fiber platform. The sidewall of the fiber tip is covered by a thin gold layer in order to excite plasmon modes. For computer memory efficiency reasons only the segment of the tip of a few micrometers length is simulated. The intensity enhancement is examined for PSNRs placed at different radii of the tip (Figure 2-1). The structure considered for study has a taper semi-angle of 5.33˚ and radius at the input equal to 735 nm, while the rectangular PSNR is 400 nm long and 200 nm wide. The geometrical characteristics of the tip and slot are chosen in order to be directly comparable to previously published work [18].

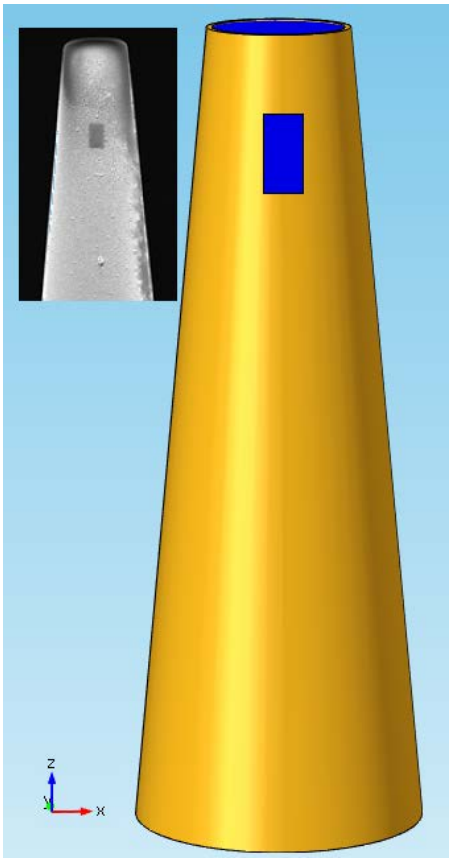

Figure 2-1. A schematic illustration of a gold-coated optical fiber tip with a rectangular plasmonic slot nano-resonator (PSNR) (inset picture: SEM image of a gold-coated fiber tip with a rectangular PSNR).

2.2.1 Mode dependence on the metal layer thickness

In order to study the effect of the metal layer thickness, simulations through *Finite Element Method* (FEM) using COMSOL Multiphysics Modelling Software were performed for the calculation of the variation of both the real and imaginary parts of the mode index of the fundamental TE polarized guided core mode (*Mode1*) as a function of the gold film thickness (Figure 2-2) using Mode Analysis. The simulated structure is a cross-section of a silica fiber surrounded by a thin gold film inside an air box. Scattering Boundary Condition (SBC) was used for the exterior boundaries to avoid reflections. The dispersion of the refractive indices of both gold and silica were taken into account. The silica core radius is r = 735 nm and the excitation wavelengths are 800, 1000 and 1550 nm. For film thicknesses less than 30 nm the n_{eff} of *Mode1* is greater than n_{SiO2}, the losses increase rapidly and it is no longer a core mode. Hence a 30 nm metal layer thickness will be used in all the following calculations.

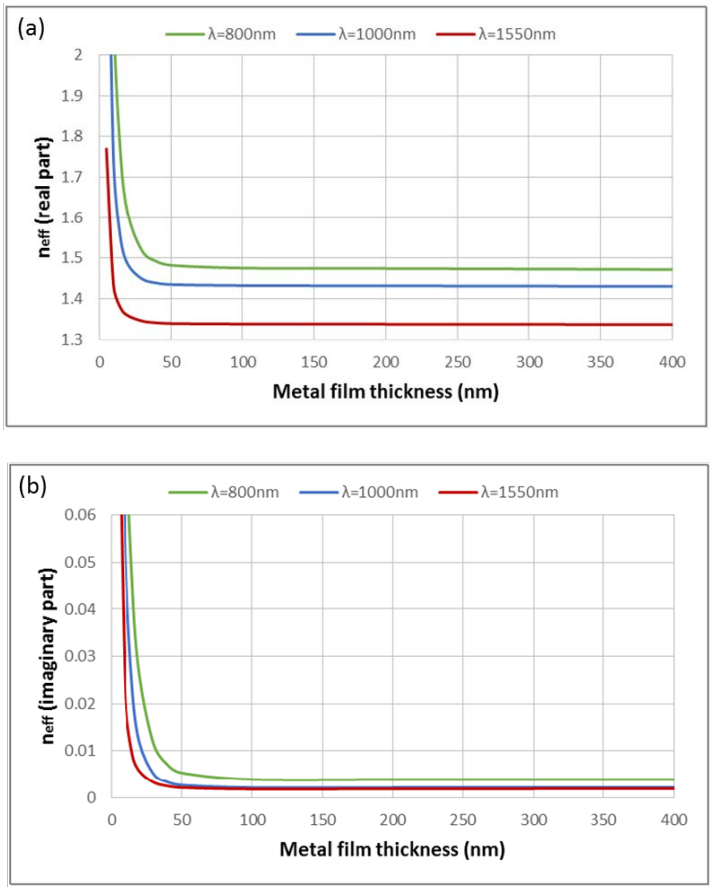

Figure 2-2. The real (a) and imaginary (b) part of the effective refractive index as a function of the metal layer thickness for a 735 nm dielectric core radius and for excitation wavelength of 800 (green), 1000 (blue) and 1550 nm (red).

2.2.2 Mode evolution in a metal-coated nano-fiber

The evolution of the two lower order hybrid core modes (*Mode1*, *Mode2*) of a gold coated silica nano-fiber was studied by calculating the real (Figure 2-3 (a)) and the imaginary (Figure 2-3 (b)) part of the effective refractive indices of the two modes as a function of the wavelength for silica core radius of 735 nm coated with a 30 nm gold layer. The azimuthal number m of these modes is equal to 1 and different colours correspond to different radial numbers.

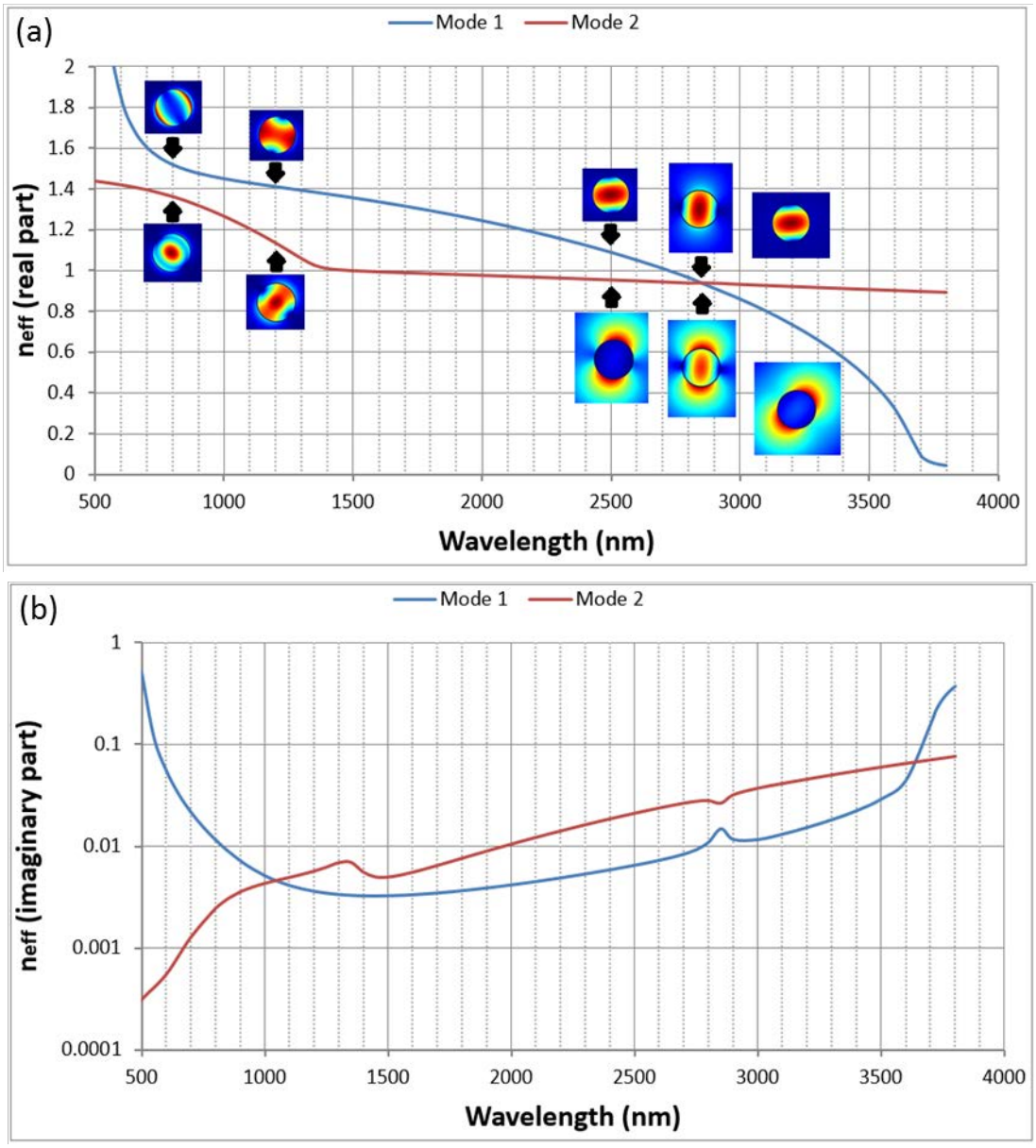

Figure 2-3. The real (a) and imaginary (b) part of the effective refractive index as a function of the wavelength for different modes. The thickness of the gold layer is 30 nm and the radius of the silica core is 735 nm. Inset pictures present the z-component of the Poynting vector of Mode1 (top) and Mode2 (bottom).

Inset pictures of Figure 2-3 show the z-component of the Poynting vector of *Mode1* (top) and *Mode2* (bottom). As n_{eff} becomes higher than n_{SiO2}, for $\lambda < 1200$ nm, *Mode1* is transformed from a core mode to an internal-like SPP mode [57] and the losses increase rapidly since the field is no longer inside the dielectric core but confined at the metal surface. On the contrary, *Mode2* is transformed, from a core mode to an external SPP mode as its n_{eff} gets close to 1, for $\lambda > 1300$ nm, and thus it no longer contributes to the core field. At $\lambda = 2850$ nm *Mode1* and *Mode2* cross while *Mode2* becomes partially a core mode again. For wavelengths longer than 2850 nm *Mode1* and *Mode2* are core and external SPP mode, respectively.

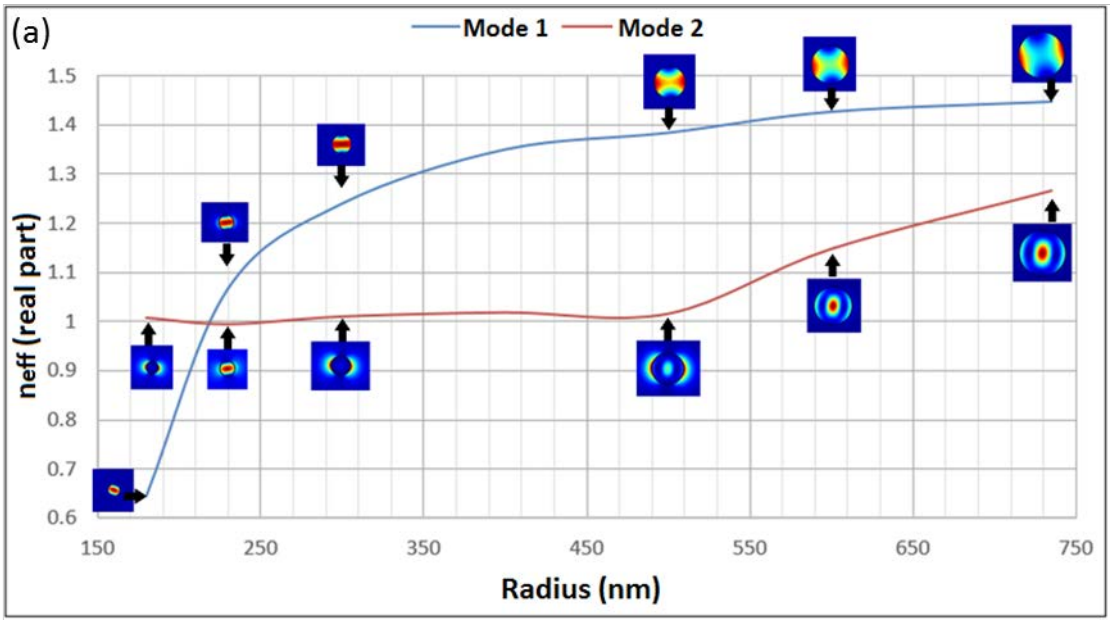

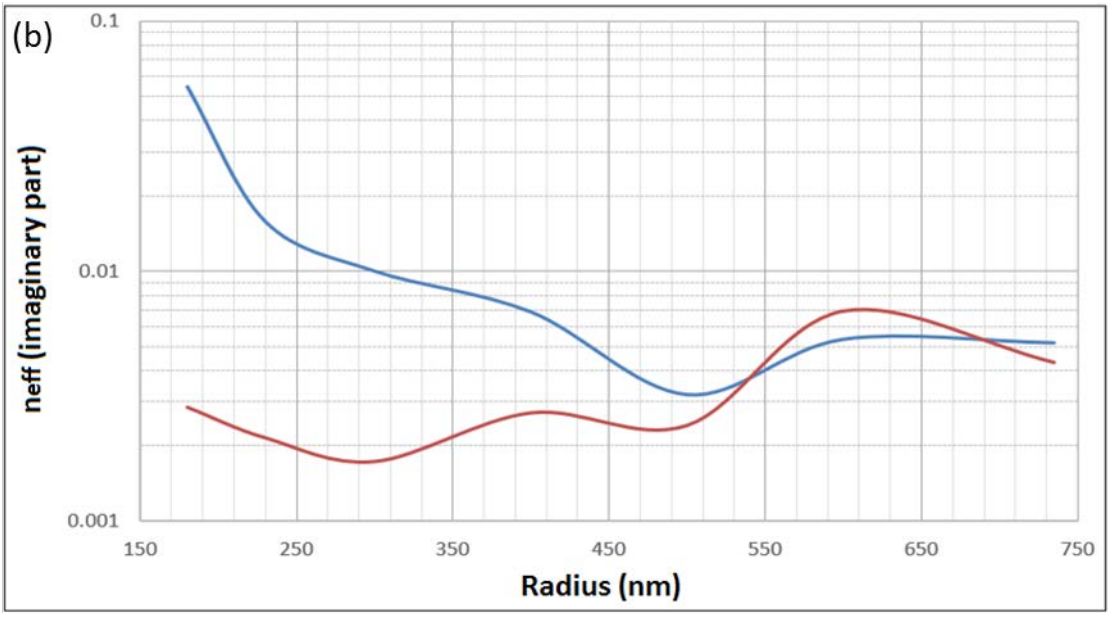

Figure 2-4. The real (a) and imaginary (b) part of the effective refractive indices of Mode1 and Mode2 as a function of the radius of the silica core. The excitation wavelength is 1000 nm.

Figure 2-4 shows the effective refractive indices of *Mode1* and *Mode2* as a function of the radius of the silica core for 1000 nm excitation wavelength. The evolution of the two lower order hybrid core modes, as represented by the z-component of the Poynting vector, is also demonstrated in the figure. For r>690 nm the n_{eff} of *Mode1* is higher than n_{SiO2}, and *Mode1* is an internal SPP mode, while *Mode2* is partially a core mode having lower losses than *Mode1*. For r<500 nm, *Mode1* is transformed to a core mode and *Mode2* becomes an external SPP mode and stops contributing to the core field.

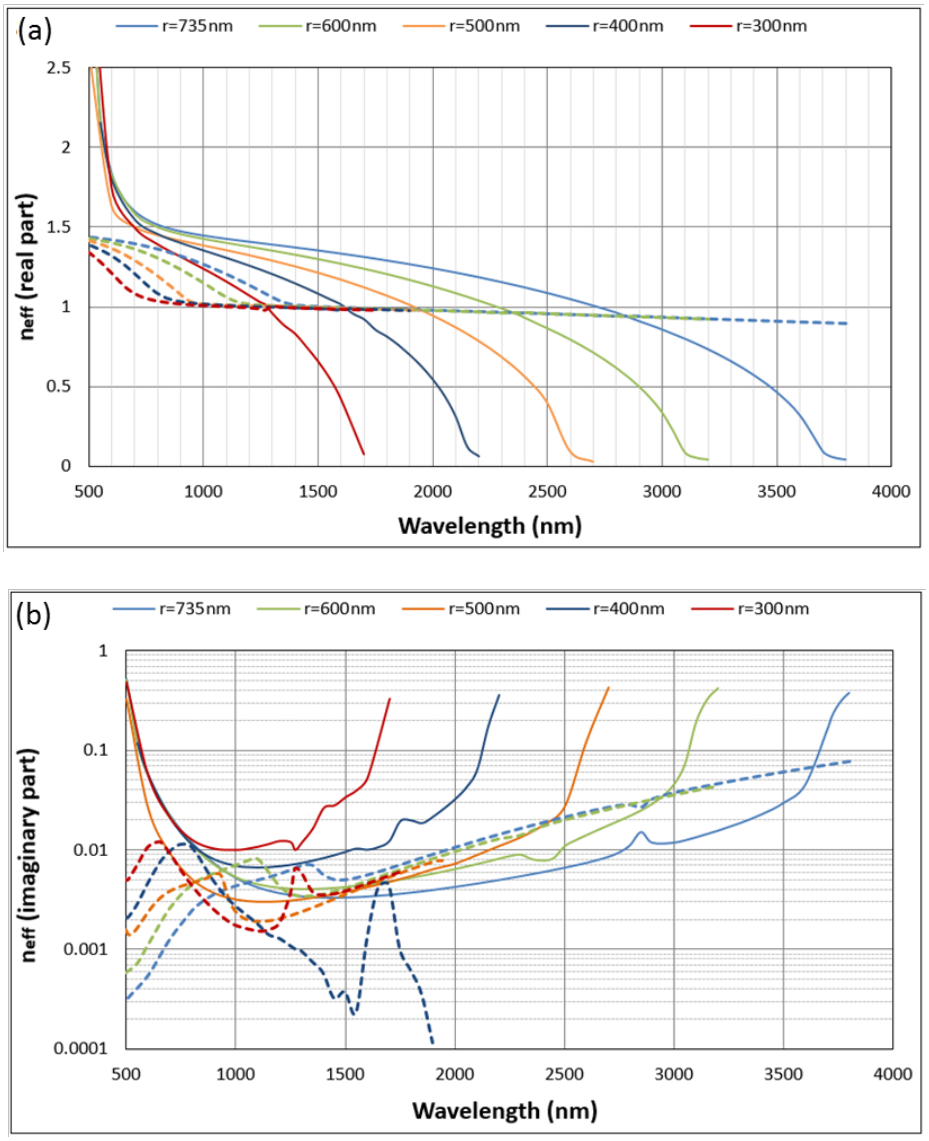

Figure 2-5. The real (a) and imaginary (b) part of the effective refractive index as a function of the wavelength for Mode1 (solid line) and Mode2 (dashed line) for different core radii. The thickness of the gold layer is 30 nm. Different colours correspond to different radii of the silica core.

Although, for r > 540 nm, *Mode2* is a core mode it exhibits more losses than *Mode1* which is an internal plasmon-like mode. On the contrary, as seen in Figure 2-5 (b), for r < 500 nm *Mode2* has lower losses than *Mode1*, hence the electric field at the silica/gold interface is one order of magnitude lower than that of *Mode1* which is crucial when PSNR's are embedded since high field intensity is needed to excite the PSNR in order to get the highest possible field enhancement when resonance is met.

The dispersion of *Mode1* and *Mode2* is also studied for different core radii and for gold film thickness of 30 nm (Figure 2-5). The effective refractive index of *Mode1* decreases and the dispersion curves shift to shorter wavelengths as the core radius decreases.

The cut-off wavelength for *Mode1*, namely the wavelength at which n_{eff} approaches to zero, is a linear function of the core radius fitted by the relation:

$$\lambda(nm) = 4.7r(nm) + 144.6 \quad (2\text{-}1)$$

Mode2 does not exhibit a cut-off since for long wavelengths it is an external SPP mode.

The wavelength corresponding to n_{eff} = 1 for *Mode1* is also a linear function of the wavelength (Figure 2-6) fitted by:

$$\lambda(nm) = 3.3r(nm) + 296.7 \quad (2\text{-}2)$$

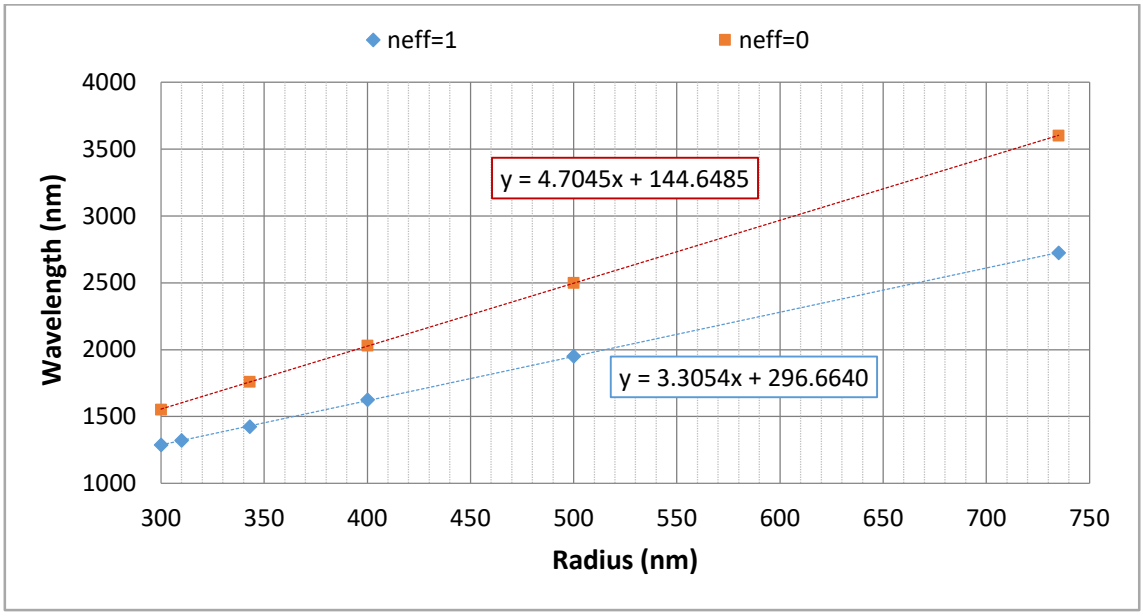

Figure 2-6. Excitation wavelength versus tip's core radius corresponding to n_{eff} = 1 (blue) and n_{eff} ≈ 0 (red).

When n_{eff} becomes less than unity, the phase velocity becomes larger than the speed of light c and the transmissivity decreases rapidly and light gets totally blocked when $n_{eff} = 0$. Hence the highest field intensity for a specific core radius is expected at the wavelength for which $n_{eff} \approx 1$. Therefore the exhibited linear dependence between excitation wavelength and radius of equation (2-2) offers the design flexibility to select the proper radius for a specific wavelength for maximum enhancement. Equations (2-1) and (2-2) cross for core radius equal to 109 nm. Consequently n_{eff} decreases rapidly as a function of the wavelength for r ≈ 110 nm since the wavelengths corresponding to $n_{eff} = 1$ and $n_{eff} = 0$ are very close. This leads to group velocity, defined as $d\omega/d\beta$, close to zero for $n_{eff} = 1$. Therefore the cut-off radius for the studied structure is approximately 110 nm since light cannot propagate for smaller radii. Hence for a gold-coated fiber tip the highest confinement is expected at r ~110 nm and for λ ~660 nm which is the wavelength corresponding to n_{eff} ~1 according to equation (2-2).

The group velocity (u_g) of *Mode1*, for the cylindrical structure with a 30 nm gold layer as a function of the core radius for different excitation wavelengths was also calculated (Figure 2-7). As expected, when the core radius decreases, u_g decreases too and light slows down. As the excitation wavelength decreases, the cut-off radius moves to lower values.

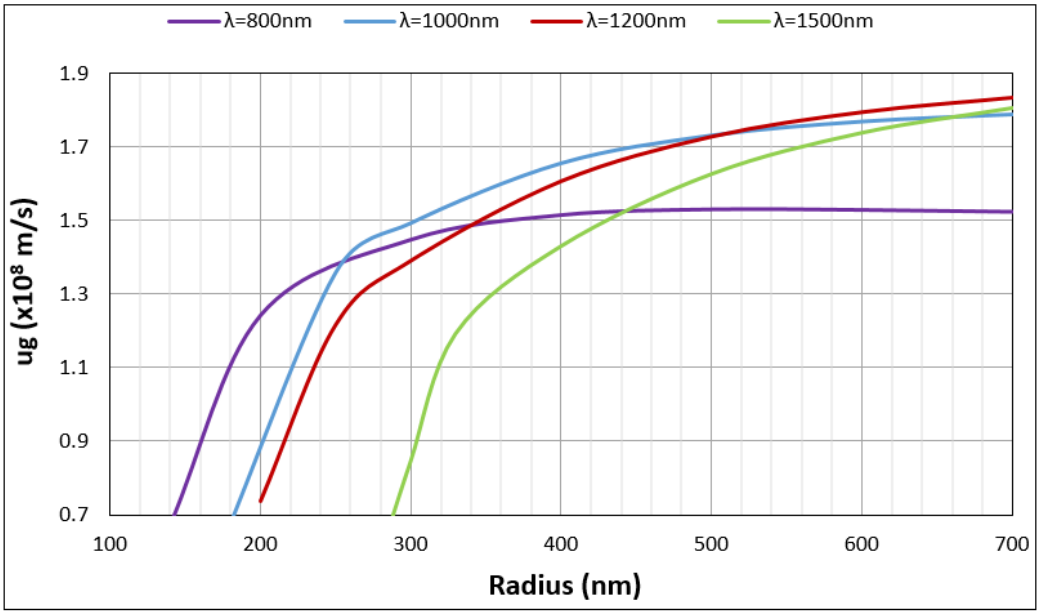

Figure 2-7. Group velocity (u_g) of Mode1 as a function of the core radius for different wavelengths.

2.3 Calculation of field enhancement at silica/gold interface of fiber tips

Gold-coated fiber tips with a 30 nm gold layer, semi-angle a = 5.33° and input radius of the silica core r = 735 nm, were simulated. As discussed above for 735 nm core radius, *Mode2* stops contributing to the core field for λ > 1400 nm as it becomes an external SPP mode. Furthermore for λ < 1000 nm although *Mode2* is a core mode and has lower losses than *Mode1*, the electric field at the silica/gold interface is lower than that of *Mode1* resulting in a decreased enhancement of the field when a PSNR is embedded. Hence, the only launched mode is the fundamental TE polarized core mode (*Mode1*) with polarization along the x direction, using Boundary Mode Analysis. Since the light is x-polarized and the structure is symmetric with respect to the y–z plane, we calculate half of it for memory efficiency reasons. In order to excite the x-polarized fundamental core mode the separatrix is set to be a Perfect Electric Conductor (PEC), i.e., the tangential component of the electric field **E** is zero on the y-z plane (**n** x **E** = **0**, where **n** is the unit vector normal to the y-z plane). Port boundary was used for the input of the

fiber. The structure is surrounded by an air box and SBC was used for the exterior boundaries to avoid reflections.

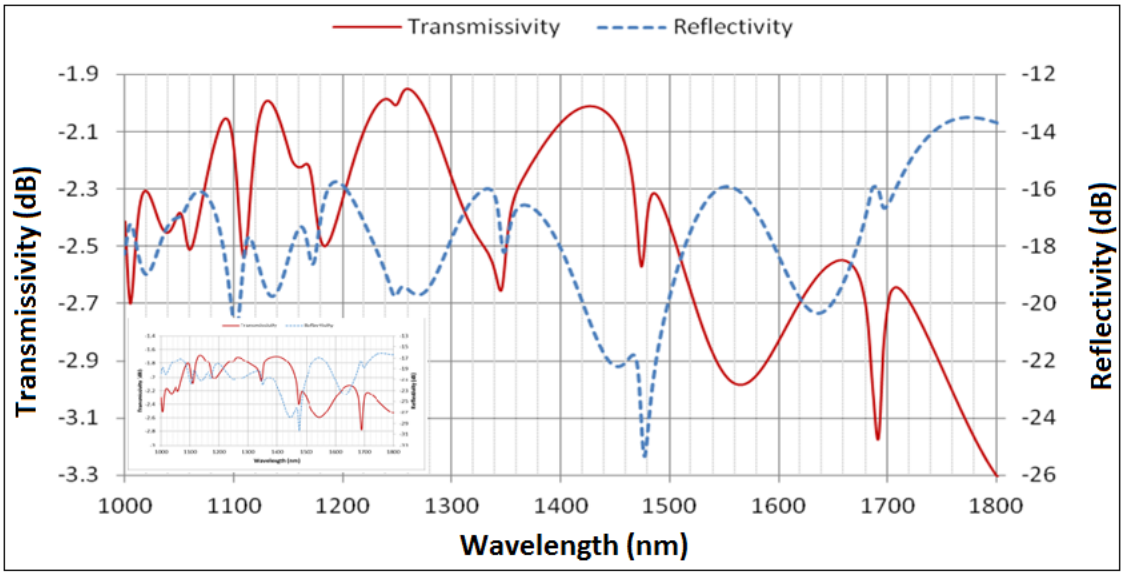

Figure 2-8. Transmissivity (red solid) and reflectivity (blue dashed) of a 4.2 μm long plasmonic tip with 343 nm output radius and semi-angle, a = 5.33°, as a function of the wavelength. The inset picture shows the spectrum when PML was used at the apex of the tip.

Figure 2-8 shows the transmissivity and reflectivity of a 4.2 μm long plasmonic tip with 343 nm output radius and semi-angle, a = 5.33°. Simulations of the same fiber tip were also performed using Perfectly Matched Layer (PML) at the output, a layer that absorbs radiation without producing reflections in order to check the effect of the reflection at the tip's end in the reflectivity spectrum. The reflectivity spectrum has exactly the same form but lower reflectivity values (Figure 2-8 (inset picture)). Therefore, the form of the reflectivity spectrum is related to internal reflections of the mode and not to reflection at the tip's end. For r = 343 nm, n_{eff} becomes 1 at λ = 1430 nm. For λ > 1430 nm the corresponding values of n_{eff} are smaller than unity and the transmissivity decreases as shown in Figure 2-8.

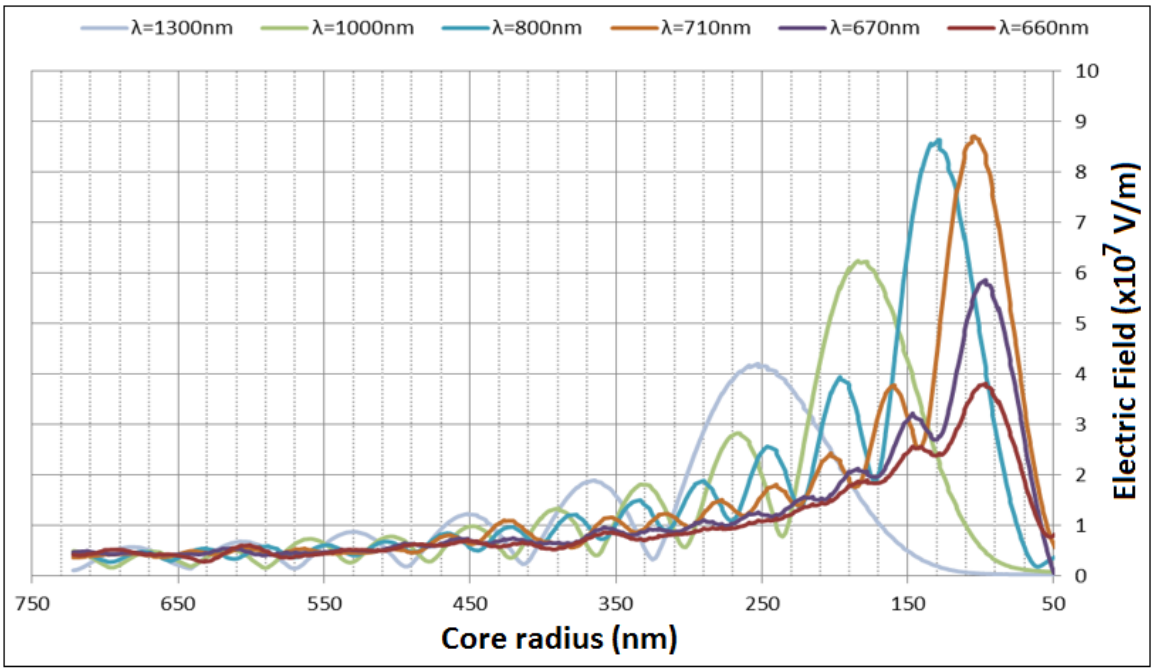

Figure 2-9. Normalized electric field along the silica – gold interface for a 4.5μm long tip with semi-angle of 9°. The input radius is 735 nm. Different colors are associated with different wavelengths.

Figure 2-9 presents the normalized electric field along the silica–gold interface for a 4.5μm long plasmon tip with semi-angle of 9°, for different wavelengths. The input and output radius of the tip is 735 nm and 22 nm, respectively. The enhancement factor (E_f) is defined as the maximum intensity *I* divided by the intensity I_o at the silica surface at the input of the fiber tip. As the excitation wavelength decreases the peak shifts to lower core radius due to the shift of *Mode1* dispersion curves to shorter wavelengths as the core radius decreases. As the wavelength increases $n_{eff,Mode1}$ crosses unity at higher tip radius and thus it cannot penetrate at smaller radii of the fiber tip. On the contrary, as the wavelength decreases, *Mode1* has not reached the cut-off for lower core radii resulting to the observed peak shift. This results from the fact that in waveguides of fixed numerical aperture the electromagnetic behaviour (e.g. modality, field confinement, dispersion) scale roughly with the ratio r/λ for optical fibers or d/λ for planar waveguides and thus by decreasing the wavelength the cut-off occurs at smaller diameters of the composite waveguide. The highest E_f calculated is ~850 and is observed for λ = 710 nm corresponding to a tip radius ~110 nm, confirming that this is indeed the cut-off radius as discussed above.

2.4 Plasmonic fiber tips with embedded PSNRs

This section presents simulations of plasmonic tips with an embedded rectangular PSNR of 400 nm length and 200 nm width. The PSNR was embedded at the x-z plane so

the structure is symmetric with respect to the y–z plane and half of it was simulated. The launched mode was polarized along the x-direction in order to excite the Plasmon Resonance (PR) at the PSNR. When the PR is excited the current density is parallel to the perimeter of the slot. For y-polarized light the current density is perpendicular to the perimeter exciting the weaker Fabry-Perot like resonance (Figure 2-10) [52], [58].

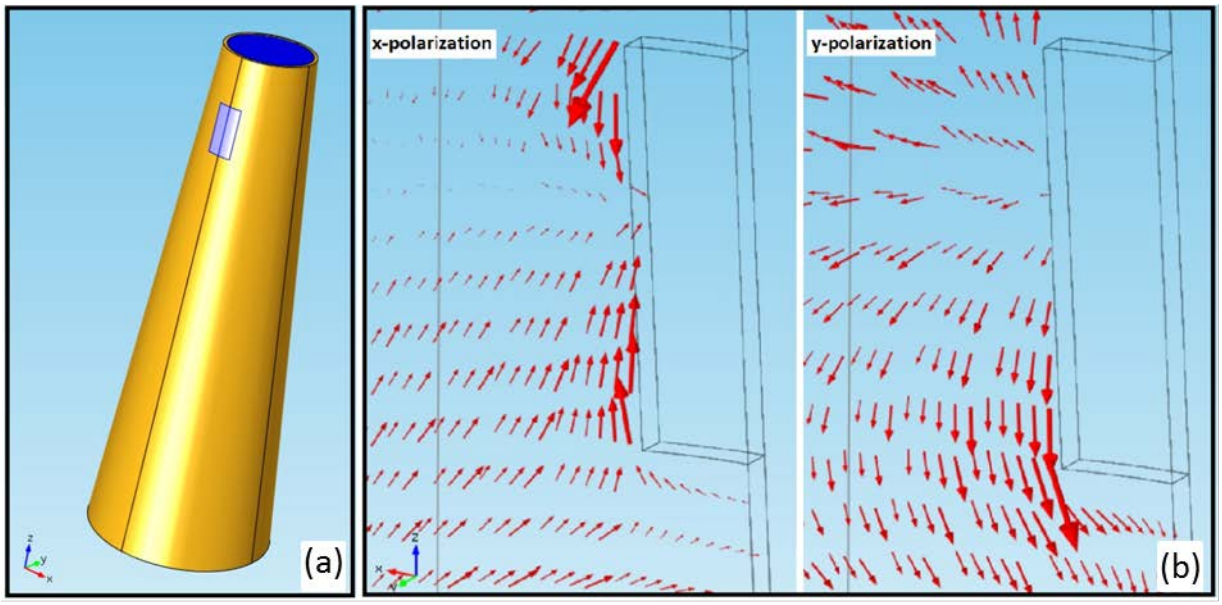

Figure 2-10. a) The simulated fiber tip. b) Current density for x-polarized (left) and y-polarized (right) launched mode.

2.4.1 Calculation of field enhancement at PSNR's embedded in plasmonic fiber tips

As discussed above, for a plasmonic fiber tip, the maximum field confinement is expected for n_{eff}~1. Therefore for different wavelengths the light is highly confined at different radius of the plasmonic tip. After embedding a rectangular PSNR, with 400 nm length and 200 nm width, at radius r = 400 nm, in a 4.2μm long plasmonic tip with a = 5.33˚, we calculated an enhancement factor (E_f) of 1.29×10^5 at λ = 1550 nm. The E_f is calculated as the maximum intensity *I* in the PSNR, divided by the intensity I_o at the silica surface at the input of the fiber tip in order to also study the effect of the PSNR's placement instead of just the effect of the PSNR's resonance. Using the above definition the E_f for slot embedded at r = 610 nm as published in [18] is 1.77×10^4 for λ = 1450 nm, which implies that at r = 400 nm the field is indeed highly confined. For slot embedded at r = 400 nm, the maximum E_f is found to be at λ = 1550 nm, as presented in Figure 2-11 (a) and not at λ = 2150 nm for which the n_{eff} is close to zero, though there is a local maximum at this wavelength. For r = 400 nm the wavelength at which n_{eff} becomes less than unity is ~1625 nm, but the highest E_f is at λ = 1550 nm. This is

probably due to resonances related to the slot and its dimensions. The slot is 400 nm long at the direction of propagation, thus the lower part of the slot is at radius r = 418 nm and its upper part is at r = 380 nm. For r = 380 nm, n_{eff} = 1 at λ = 1553 nm. The core mode is internally reflected, as discussed above, and forms cavity modes [59]. Consequently, periodic peaks appear in the field enhancement spectrum for λ < 1550 nm corresponding to the minima of the reflection spectrum in Figure 2-8.

Figure 2-11 (b) shows the normalized electric field for λ = 1550 nm and λ = 2150 nm which correspond to the wavelengths where n_{eff} is close to 1 and close to 0 respectively for r ~400 nm. For n_{eff} = 1 the field reaches its highest confinement. The transmissivity starts decreasing as n_{eff} decreases further for longer wavelengths and when n_{eff} is zero the field is blocked as it can no longer propagate inside the plasmonic tip ($u_g \rightarrow 0$ and $u_{ph} \rightarrow \infty$).

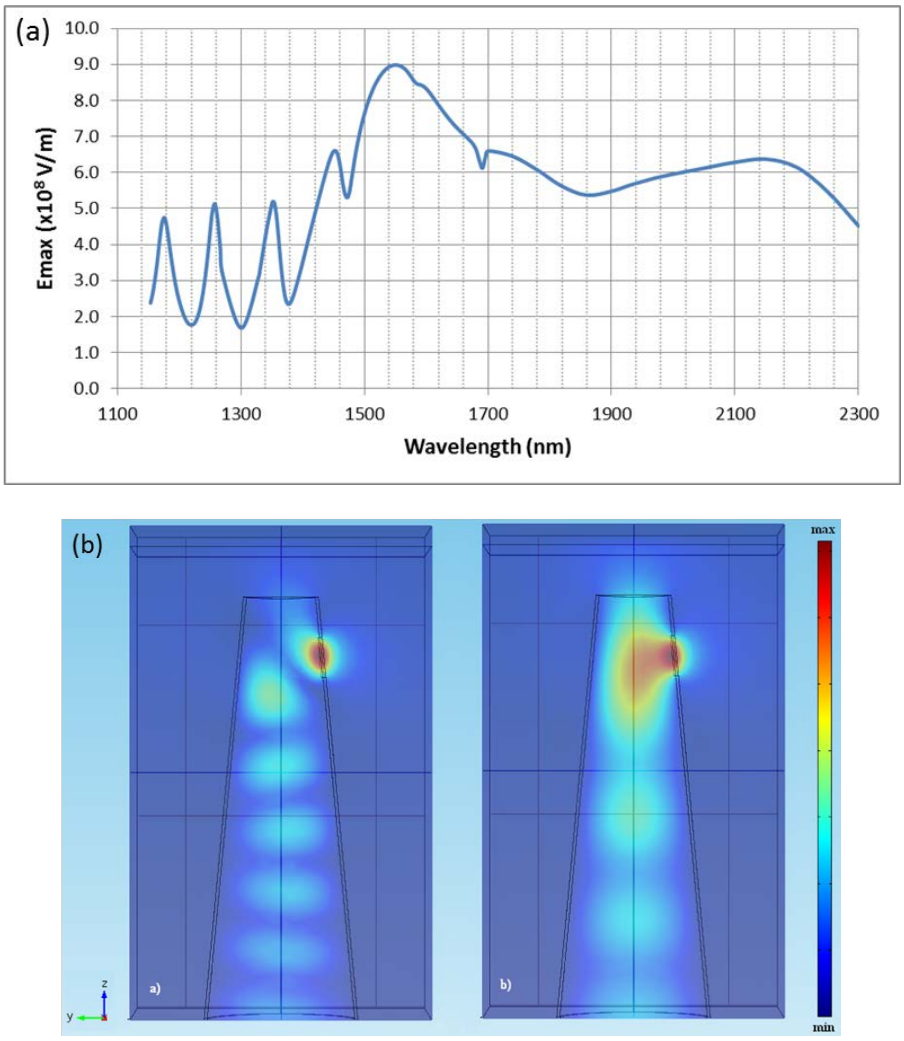

Figure 2-11. (a) Maximum normalized electric field in the slot embedded at r = 400 nm of a plasmonic fiber tip (a = 5.33˚), as a function of the wavelength. (b) The normalized electric field for a) λ = 1550 nm and b) λ = 2150 nm. The PSNR is embedded at r = 400 nm.

2.4.2 Effect of radius and taper angle

In order to investigate the effect of the fiber radius where the PSNR is embedded, we also embedded a slot of the same size as above at different radii. As the radius decreases, the E_f increases (Table 2-1). The highest E_f was calculated for slot embedded close to the cut-off radius, at r = 150 nm. The value of the E_f is 5.0×10^5 for λ = 670 nm, which is ~30 times higher than previously published in [18]. For slots of the same size embedded at r < 150 nm, the E_f decreases. The reason for calculating the highest E_f for slot embedded at r = 150 nm and not at r = 110 nm is, as discussed above, due to the dimensions of the slot. Therefore, the optimum position for embedding the PSNR, namely the position where the E_f gets its maximum value, is at r ~150 nm.

Semi-angle (α)	**Radius (r) at the position of the PSNR**	**Wavelength**	**Enhancement factor (E_f)**
5.33°	400 nm	1550 nm	1.29×10^5
5.63°	380 nm	1525 nm	1.35×10^5
6.21 °	335 nm	1391 nm	1.41×10^5
8.764°	180 nm	927 nm	2.66×10^5
9.23°	150 nm	670 nm	5.00×10^5

Table 2-1. Geometrical parameters of plasmon tips and the corresponding calculated enhancement factors for PSNRs embedded at the same axial distance from the input (z = 3.6μm).

For λ < 1200 nm the n_{eff} for the input radius approaches the refractive index of silica, as discussed above, and the maximum electric field is no longer at the core but at the silica-gold interface, resulting in a rapid increase of the losses. Therefore, for slots embedded at radii smaller than 270 nm, for which the n_{eff} becomes equal to 1 at λ ~1200 nm, the losses play a crucial role and thus a high semi-angle of the plasmon tip is preferable, as far as the adiabaticity is retained. A taper is adiabatic when $z_t > z_b$ [60], where z_t is the characteristic taper length defined as:

$$z_t = \frac{r}{\tan(a)} \tag{2-3}$$

and z_b is the beat length between *Mode1* and *Mode2* defined as:

$$z_b = \frac{\lambda}{(n_{eff,Mode1} - n_{eff,Mode2})} \tag{2-4}$$

In order to study the effect of losses in the value of the E_f, we also simulated plasmon tips with bigger semi-angles and we observe an increase of the E_f for slot placed at r = 335 nm when the axial distance from the input decreases (Table 2-2).

Semi-angle (α)	Axial distance from input	Wavelength	Enhancement factor (E_f)
6.21˚	3.6 μm	1391 nm	$1.41x10^5$
6.73˚	3.4 μm	1337 nm	$1.43x10^5$
11.34˚	2 μm	1397 nm	$1.70x10^5$

Table 2-2. Geometrical parameters of plasmon tips and the corresponding calculated enhancement factors for PSNRs embedded at the same radius (r = 335 nm).

For λ = 1400 nm, which is the wavelength corresponding to the maximum enhancement for PSNR embedded at r = 335 nm, the gold tapered tip is adiabatic for semi-angles up to ~11˚. Although the tip is adiabatic for α = 11˚ at λ = 1400 nm, this is not valid for other wavelengths and hence the structure should be carefully designed when working with a specific wavelength. The gold-coated tip is adiabatic for any wavelength up to 1800 nm for semi-angles up to ~7˚. For λ = 700 nm, which is the wavelength corresponding to the maximum E_f calculated at the cut-off radius, the structure is adiabatic for semi-angles up to ~12˚, a high tapering angle in order to minimize the losses.

2.4.3 Modelling of metal-coated tips with different PSNRs shapes

By nano-patterning the PSNR creating shapes with sharp edges the field intensity can be further enhanced. Figure 2-12 shows a PSNR three gold tapes in it. The width of the gold tapes decreases as the radius of the tip decreases. The position of the last gold tape (the one embedded at the smallest radius) is approximately at r = 400 nm.

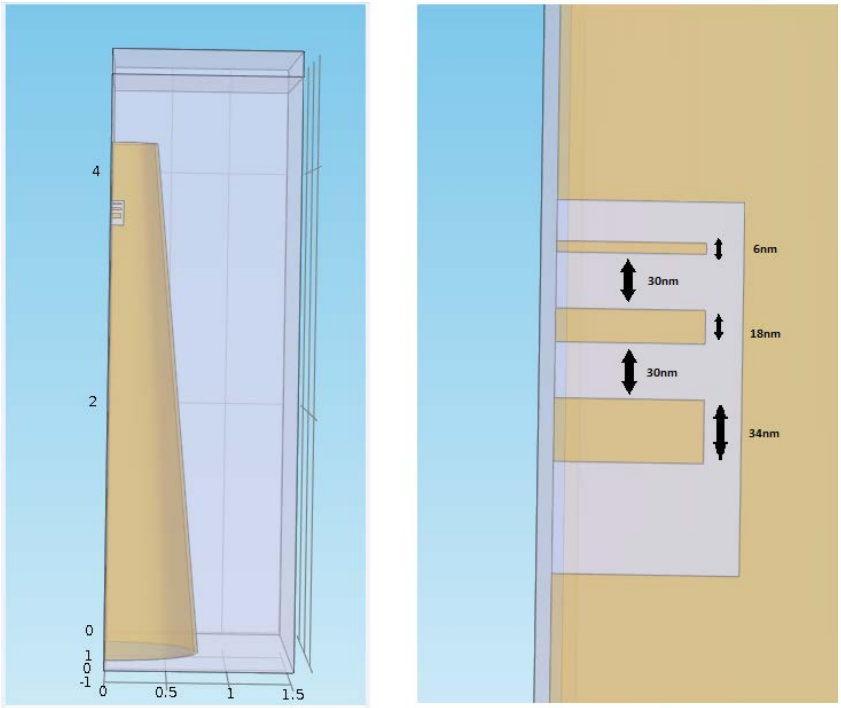

Figure 2-12. a) Plasmonic fiber tip with an embedded slot with three gold tapes, b) The slot with the three gold tapes. The tapes have widths 34, 18 and 6 nm and the distance between them is 30 nm.

Figure 2-13 shows the transmissivity and reflectivity of the rectangular PSNR with the three gold tapes embedded in the plasmonic fiber tip at r = 400 nm (a) and the maximum normalized electric field as a function of the wavelength (b). The enhancement factor at λ = 1645 nm is 3.27 $x10^5$ which is two orders of magnitude higher than the rectangular PSNR embedded in the plasmonic fiber tip at r = 610 nm for λ = 1458 nm. The minimum enhancement factor for the whole spectral range is 1.17 $x10^4$. For higher maximum electric field the space confinement increases.

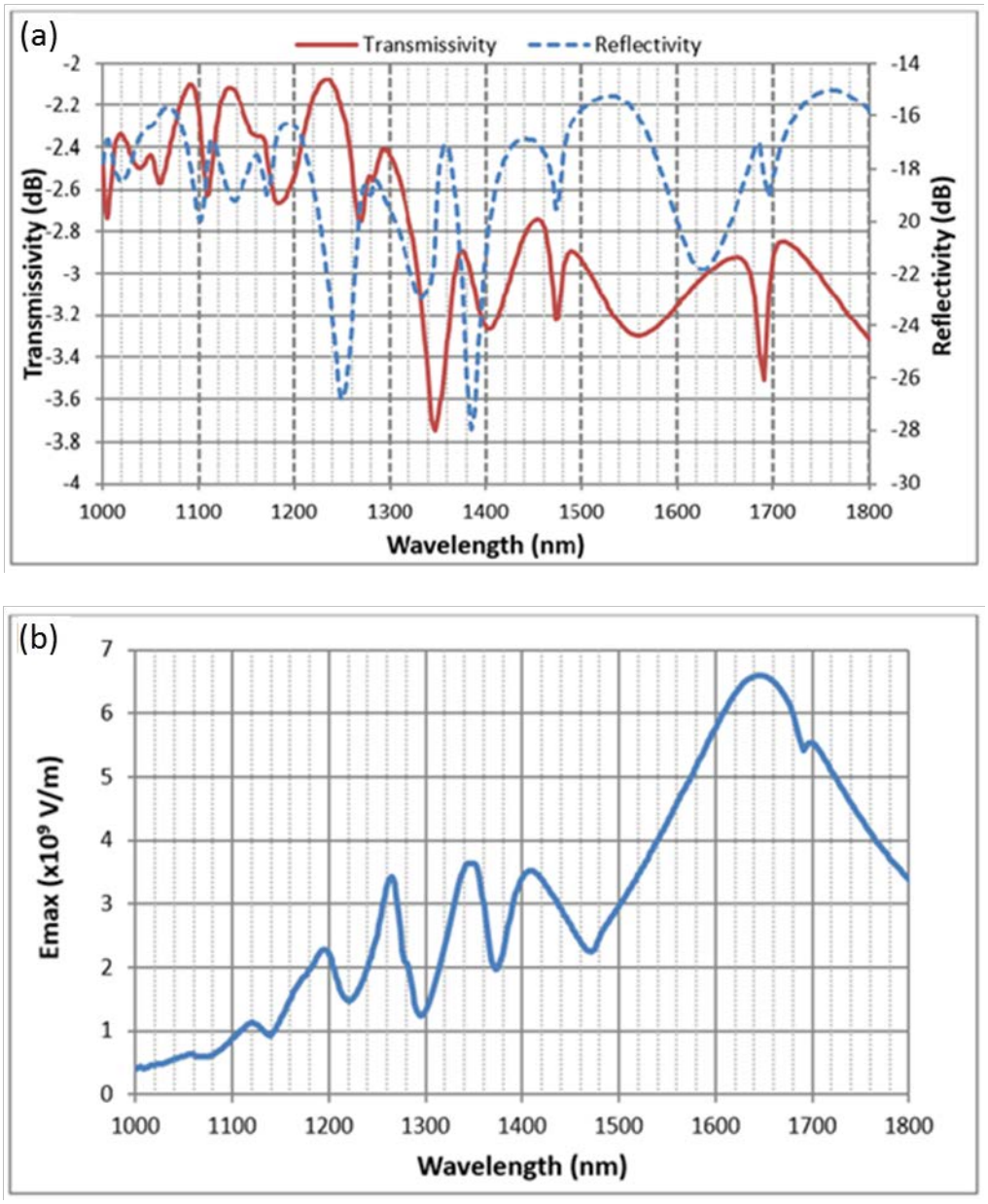

Figure 2-13. (a) Transmissivity (red solid) and reflectivity (blue solid) of the rectangular PSNR with three gold tapes embedded in the plasmonic fiber tip at r = 400 nm, for x-polarized light. (b) Maximum normalized electric field as a function of the wavelength.

After the 2D analysis of the structure presented above, we calculated that for r = 400 nm silica core and a 30 nm gold layer, n_{eff} becomes less than unity for $\lambda > 1622$ nm. Figure 2-14 shows the normalized electric field for wavelengths of 1645 nm and 1460 nm. The high E_f for $\lambda = 1645$ nm corresponds to high spatial field confinement at the sharpest edge of the structure.

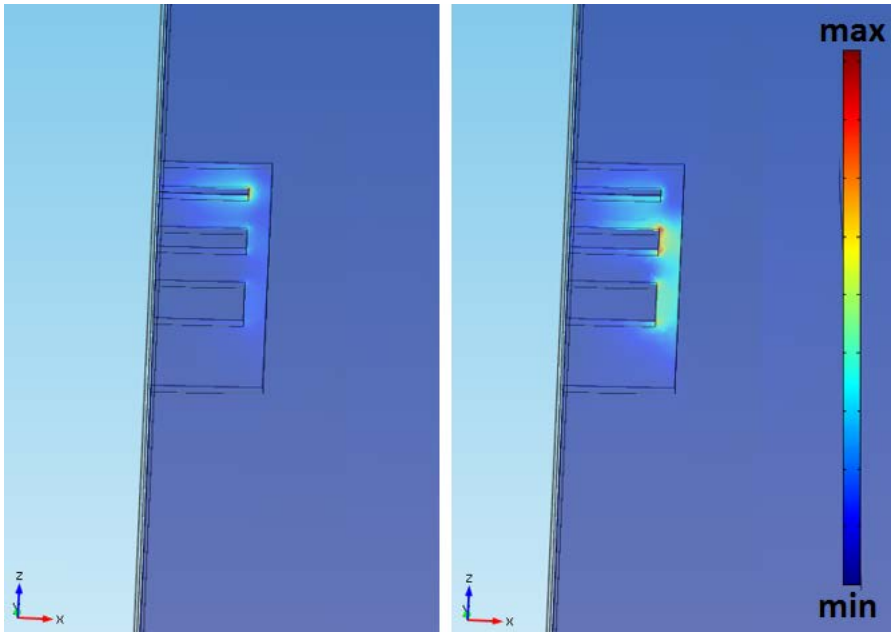

Figure 2-14. Normalized electric field for a) 1645 nm and b) 1460 nm.

2.5 Conclusions

Metal coated optical fibers and fiber tapers with embedded PSNRs suggest a robust platform for plasmonic applications. The highly confined field, due to the tapering of the microfiber, combined with the resonant effects of PSNRs, can provide high field enhancement that can find many applications in SERS, bio-sensing or data storage. It was shown that the optimum position for embedding a PSNR is at the corresponding cut-off radius where the highest confinement of the field is reached. The cut-off radius for a silica - fiber with a 30 nm gold layer was found to be around 110 nm where the wavelengths corresponding to $n_{eff} = 1$ and $n_{eff} = 0$ are very close and the group velocity tends to zero. Also the wavelength at which the highest E_f for a specific radius is expected, is the one that corresponds to n_{eff}~1, since when n_{eff} becomes less than unity, the phase velocity becomes larger than c and the transmissivity decreases. After embedding a PSNR centred at r = 150 nm we calculated the highest E_f of $5x10^5$ which is 30 times higher than previously reported. This improvement can be critical for specific applications like SERS as can dramatically enhance the total signal enhancement which is proportional to the fourth power of the electric field (E^4). Furthermore, due to the crucial limiting factor of losses in the performance of those plasmonic structures, a further optimization of taper angle is also important for reducing the propagation length and associated losses while retaining the adiabaticity. Further optimization of the shape and dimensions of the PSNR by rigorous multivariable optimization strategies [61] could lead to further intensity enhancement, even by orders of magnitude, due to resonances corresponding to the cut-off wavelength (~700 nm).

Chapter 3

Fully controllable fabrication of plasmonic tips by tapering composite metal core/dielectric cladding microfibers

3.1 Introduction

Metal tips are another type of very promising nanofocusing plasmonic structure that has been studied extensively [20]–[23] since they enable the confinement of light at the tip apex providing strong field localization. In this work metal tips having dielectric cladding are studied. The tips are fabricated by tapering hybrid metal core/glass cladding microfibers. The glass cladding not only mechanically supports the metal core but also offers ease of coupling light into the device. Furthermore due to the total internal reflections at the glass/air interface the plasmon modes travelling along the metal/dielectric interface are continuously re-excited [24]. The re-excitation of the plasmon modes is crucial for limiting the losses induced by the metal.

The fabrication of metal tips by tapering hybrid microfibers offers accurate control of their geometrical characteristics. The heating and stretching method [29], [51] used in this work is a simple, cost-effective technique compared to more complicated methods such as Focused Ion Beam (FIB). This results in the formation of smooth tips with small semi-angles. Furthermore the fabricated tips have a dielectric cladding along all of their length, compared to previously published works where the metal tip is formed outside of the glass cladding [21], ensuring the re-excitation of plasmon modes up to the tip apex.

Although the tapering process used for the fabrication of metal tips is a low complexity method, there were some limitations that had to be overcome. In order to properly taper the microfibers the glass softening point and the metal melting point had to be close. For this reason borosilicate glass was chosen as cladding due to its low softening and working points. Moreover the core continuity is crucial for the tapering process as random discontinuities of the metal core would result in the collapse of the surrounding glass.

Although the drawing of fibers containing base metals has already been investigated [62], the study of fibers containing noble metals is of intense interest for plasmonic devices. The manufacturing and post processing [53], [63] of such fibers though is quite challenging due to the combination of materials with different mechanical and physicochemical properties. At high temperature processing conditions, a number of instabilities induce various microfluidic phenomena leading in turn to formation of various embedded microstructures. The understanding of those phenomena is crucial, as it would help either to avoid such structures or help in their tailored fabrication. The choice of materials with compatible properties, such as melting and working points, is crucial in order to successfully draw uniform and low loss fibers. For the fabrication of fibers with uniform diameters and continuous metallic cores, key parameters, such as feed rate of the metal, temperature, and pull rate, should be optimized during the drawing process [64], [65]. In the high temperature conditions needed for the fabrication of such multi-material systems, the breakup of the core is commonly observed, and the consequent formation of spheres, and thus the temperature profile, must be carefully controlled. This breakup is attributed to the Plateau-Rayleigh Instability (PRI), which grows in the low viscosity regime. Furthermore, as the diameter of the metal decreases, the instability increases, limiting the reduction of the fibers' diameters in the nanoscale, where fragmentation of the metal can occur, even at temperatures lower than the bulk melting temperature [66], [67].

Although the breakup of the core needs to be avoided during the fabrication and post-processing of hybrid optical fibers, the study of the formation of an array of spheres could be of great value for many applications, such as the development of integrated optical microresonators [64]. Recent studies of capillary instabilities [68]–[70] have paved the way towards this direction. Chains of dielectric [71]–[73] and Cu [74] nanoparticles have already been demonstrated, showing high control over both size and spacing of the nanoparticles. The formation of noble metal micro-nano spheres in an all-fiber plasmonic device, such as the one proposed here, would offer mechanical robustness, ease of light coupling, as well as the possibility of its integration into standard optical fibers, enabling the remote use of the device.

In this chapter the fabrication of hybrid plasmonic tips is studied. FEM microfluidic simulations as well as instability analysis are performed in order to find the optimum conditions for the tapering process. Electromagnetic simulations of metal tips with glass claddings are also performed for the estimation of the intensity enhancement at the tip apex. Additionally the near-field distributions at the end-faces of tapered and untapered fibers were calculated theoretically and were compared with the experimental results.

3.2 Fabrication of Hybrid Metal Core/Glass Cladding Microfibers

The hybrid metal core/borosilicate cladding microfibers were fabricated in a variety of sizes -as the fiber drawing process is not yet standardized- while in this study were considered microfibers with typical core and cladding diameters of 4μm and 30μm, respectively [65]. For the glass cladding Schott Duran borosilicate tubing of different outer and inner diameters (81 wt% SiO_2, 13 wt% B_2O_2, 4 wt% Na_2O+K_2O, 2 wt% Al_2O_3) was chosen due to the compatibility of its softening and working points which are 825 ˚C and 1260 ˚C, respectively, with the melting point of the metals used. The metals that were used are silver, copper, gold and aluminum having melting points ranging from 660 °C for aluminum to 1085 °C for copper (Figure 3-1). In this work only gold core microfibers were studied due to various current fabrication restrictions affecting microwires' core uniformity.

Figure 3-1. Left: Bundles of silver, gold and copper-core borosilicate microfibers. Right: SEM images of metal-core borosilicate microfibers.

The main parameters that were controlled during the drawing process of the fibers in order to obtain microfibers with smooth and continuous metal cores are the temperature, feed rate, pull rate and volume of the used metal. Even after the optimization of the aforementioned parameters and the fabrication of high quality microfibers, certain random discontinuities appear in the metal core of the fibers currently limiting the length available for processing. These discontinuities do not alter the mode profile at the output of the fiber due to the repeated re-excitation of the fundamental mode but they affect the tapering process as for discontinuous cores the glass collapses during the tapering. Due to the current restriction on available

continuous core fibers, only microfiber segments of limited length and with continuous cores were processed and tapered in the present study.

3.3 Study of Microwires' Modal Characteristics

Theoretical studies were performed for the calculation of the fundamental TM_{01} mode profile of hybrid microfibers as well as for the field enhancement at the tip apex using FEM by the commercial software package COMSOL Multiphysics Modelling software. A typical microfiber with a 4μm gold core diameter and a 30μm borosilicate cladding was simulated. The excitation wavelength is 532 nm and it was chosen for direct comparison with the experimental measurements. The calculated electric field of the TM_{01} mode is concentrated at the metal surface and decays exponentially far from it, forming two intense peaks corresponding to the metal/glass interface (Figure 3-2).

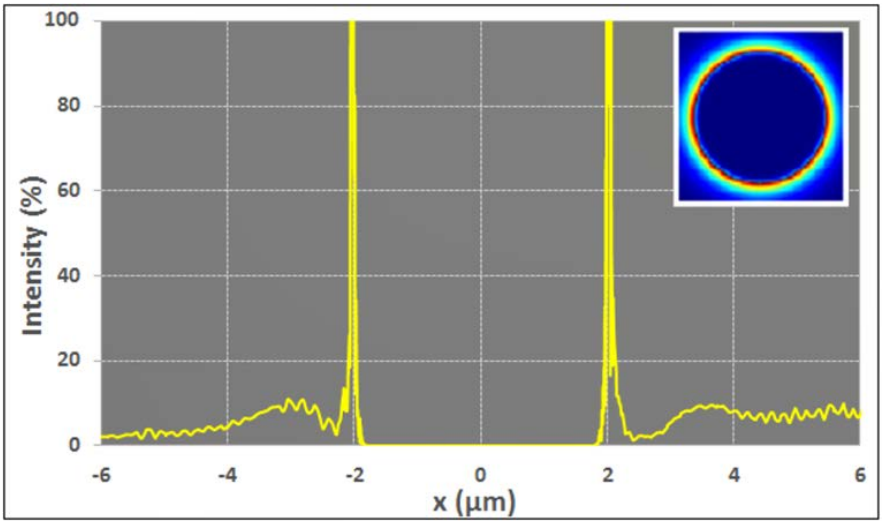

Figure 3-2. TM_{01} mode profile of a microfiber with 4μm gold core diameter and a 30μm borosilicate cladding. Inset picture: 2D representation of the TM_{01} mode profile.

The effective refractive index of the TM_{01} mode for gold core/borosilicate cladding microfibers was calculated for different core radii (Figure 3-3) using the dispersion equation [75]:

$$\varepsilon_1\alpha_2 I_1(\alpha_1 R_1)[\alpha_2\varepsilon_3 K_1(\alpha_3 R_2)M_{00} + \alpha_3\varepsilon_2 K_0(\alpha_3 R_2)M_{10}] = -\varepsilon_2\alpha_1 I_0(\alpha_1 R_1)[\alpha_2\varepsilon_3 K_1(\alpha_3 R_2)M_{01} + \alpha_3\varepsilon_2 K_0(\alpha_3 R_2)M_{11}], \quad (3\text{-}1)$$

with $M_{ab} = I_a(a_2R_2)K_b(a_2R_1) - (-1)^{a+b} I_b(a_2R_1)K_a(a_2R_2)$

Here ε_1, ε_2 and ε_3 are the relative permittivities of gold core, borosilicate cladding and air, respectively, $\alpha_j = (\beta^2 - \varepsilon_j k^2)^{1/2}$ for j = 1,2,3, β is the propagation constant, I and K are the modified Bessel functions of the first and second kind and R_1 and R_2 are the radii of the core and cladding, respectively.

The borosilicate cladding is large enough ($r_{cladding}$> 10μm) and its exact radius does not influence the n_{eff} since the field for TM_{01} mode is concentrated at the metal/glass interface as presented in Figure 3-2. As the core radius decreases both real and imaginary part of n_{eff} increase leading to significant losses for small core radius.

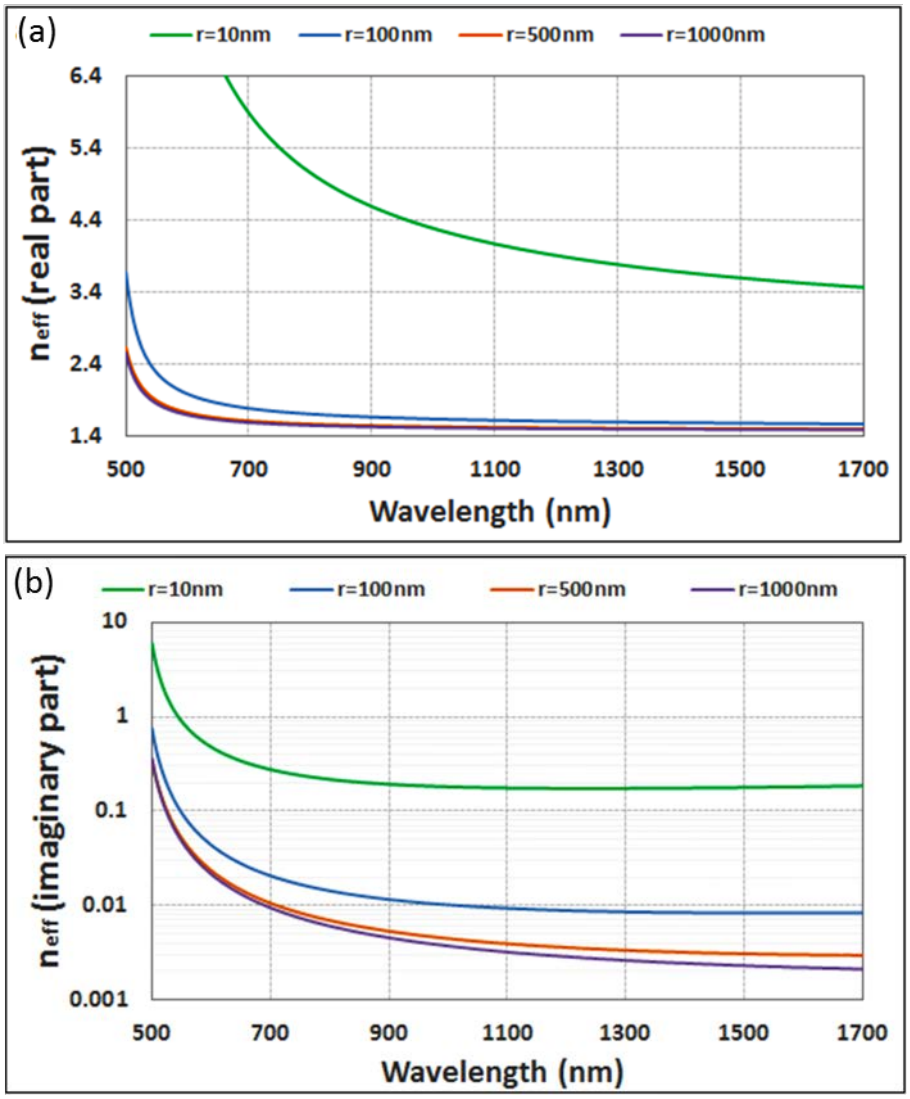

Figure 3-3. Real (a) and imaginary (b) part of the effective refractive index (n_{eff}) of TM_{01} mode as a function of the wavelength for different radii of the gold core.

3.4 3D Simulations of Metal Tips

A gold core/borosilicate cladding tapered microfiber was simulated in order to calculate the intensity enhancement at the tip apex for 532 nm excitation wavelength. Since the fabricated tapered microfibers have semi-angles between 3˚- 4˚ for both core and cladding, as it will be discussed later, the simulated tip has semi-angle α = 3.5˚. For these semi-angles the adiabaticity condition [76]:

$$\left|\frac{d(\beta_r)^{-1}}{dz}\right| \ll 1 \qquad (3\text{-}2)$$

where β_r is the real part of the propagation constant, is satisfied and thus the reflections of the SPP's that can lead to significant reduction of the intensity enhancement at the tip apex are limited. For computer memory efficiency purposes only the last 2.4μm of the tip was simulated. Furthermore in order to reduce calculation time only half of the structure was simulated with the separatrix being set to be a perfect magnetic conductor in order to launch the fundamental TM_{01} mode. In the simulated limited segment the input core radius is set to 150 nm and at the tip apex is 3 nm in order to avoid computational singularities. The core is surrounded by a large enough borosilicate glass layer and the whole structure is surrounded by a sufficient large air box with Scattering Boundary Conditions applied at its exterior boundaries to avoid reflections. Boundary mode analysis was used for launching the TM_{01} mode and the input power was 1W.

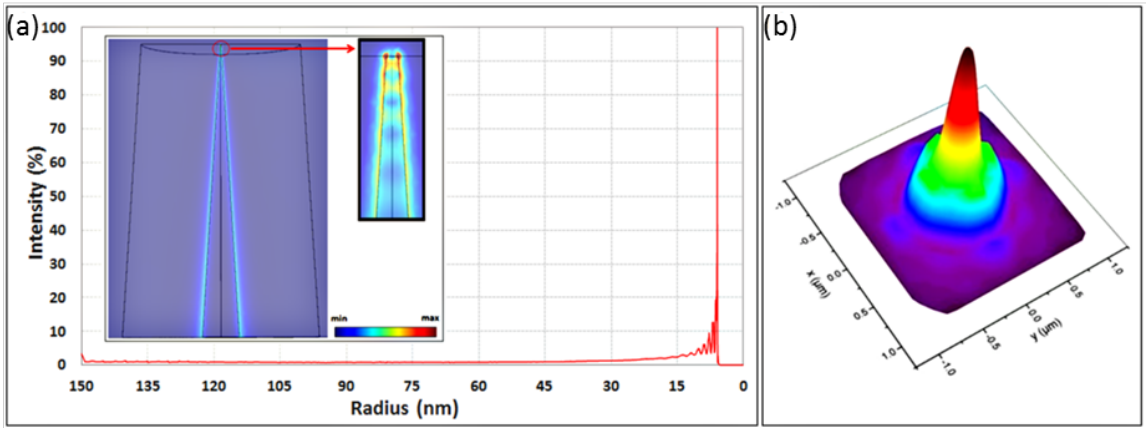

Figure 3-4. (a) Field intensity along the metal/glass interface. Inset picture: Zoom-in of the normalized intensity at the tip apex. (b) Near field at the tip apex.

Figure 3-4 (a) and (b) show the field intensity along the metal/glass interface and the near field at the tip apex respectively. The inset picture of Figure 3-4 (a) shows the field intensity at the tapered core surface. High field enhancement and localization is

achieved at the tip apex due to the excited SPP's since plasmon modes do not suffer from cut-offs contrary to photonic modes propagating in optical fibers. The intensity enhancement, calculated as:

$$E_f = \frac{I_{apex}}{I_0} = \frac{|E_{apex}|^2}{|E_0|^2} \qquad (3\text{-}3)$$

Here I_{apex}, I_0, E_{apex}, E_0 are the intensity and electric field at the tip apex and input, respectively, is ~10^3. As discussed above, due to the high losses of the TM_{01} mode for small core radii, i.e., r < 200 nm, the propagation length, defined as the distance the SPP travels before its intensity is reduced by a factor of e, is less than 4μm for λ = 532 nm. Hence the re-excitation of the TM_{01} mode from the light reflected at the glass/air interface is crucial in order to obtain a high E_f. Higher E_f up to ~10^5 can also be achieved for longer excitation wavelengths that exhibit lower losses as seen in Figure 3-5 where the maximum electric field at the tip apex (E_{max}) as a function of the wavelength is presented, which is comparable or even higher than previously published reports [77], [78]. The periodic peaks appeared in the spectrum originate from the cavity modes formed due to the reflection of the propagating SPPs at the tip apex [59]. Another factor that determines the E_f is the core radius at the tip apex. As the core radius decreases both group and phase velocities of the propagating SPPs decrease leading to the observed high field concentration. Hence the highest possible E_f corresponds to a core radius close to zero.

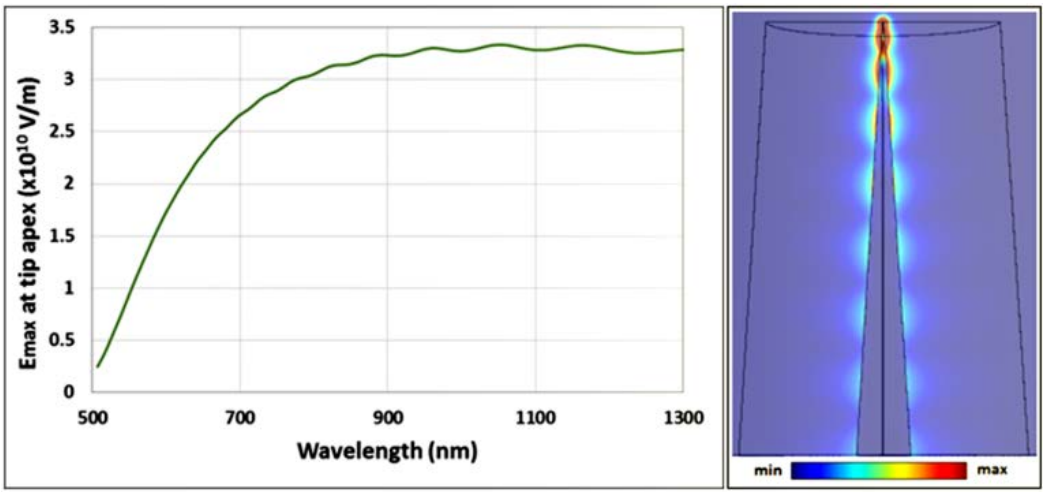

Figure 3-5. Left: Maximum normalized electric field at the tip apex as a function of the wavelength. Right: Normalized electric field for 1200 nm excitation wavelength along a tapered microfiber.

3.5 Fabrication of Metal Core/ Glass Cladding Tips

For the tapering process the heating and stretching processing method was chosen as the more suitable and flexible for tapering the gold core microfibers. The microfiber is placed on two linear stages that stretch it while a third stage moves the flame along the fiber axis (Figure 3-6). The tapering system is computer controlled via LabView software to accurately move the stages in order to obtain the desired geometrical characteristics of the tapered microfiber. The appropriate temperature is achieved by adjusting the distance between the flame and the microfiber as well as its thermal profile by controlling the ratio of the butane – oxygen mixture using two electronic mass flow controllers.

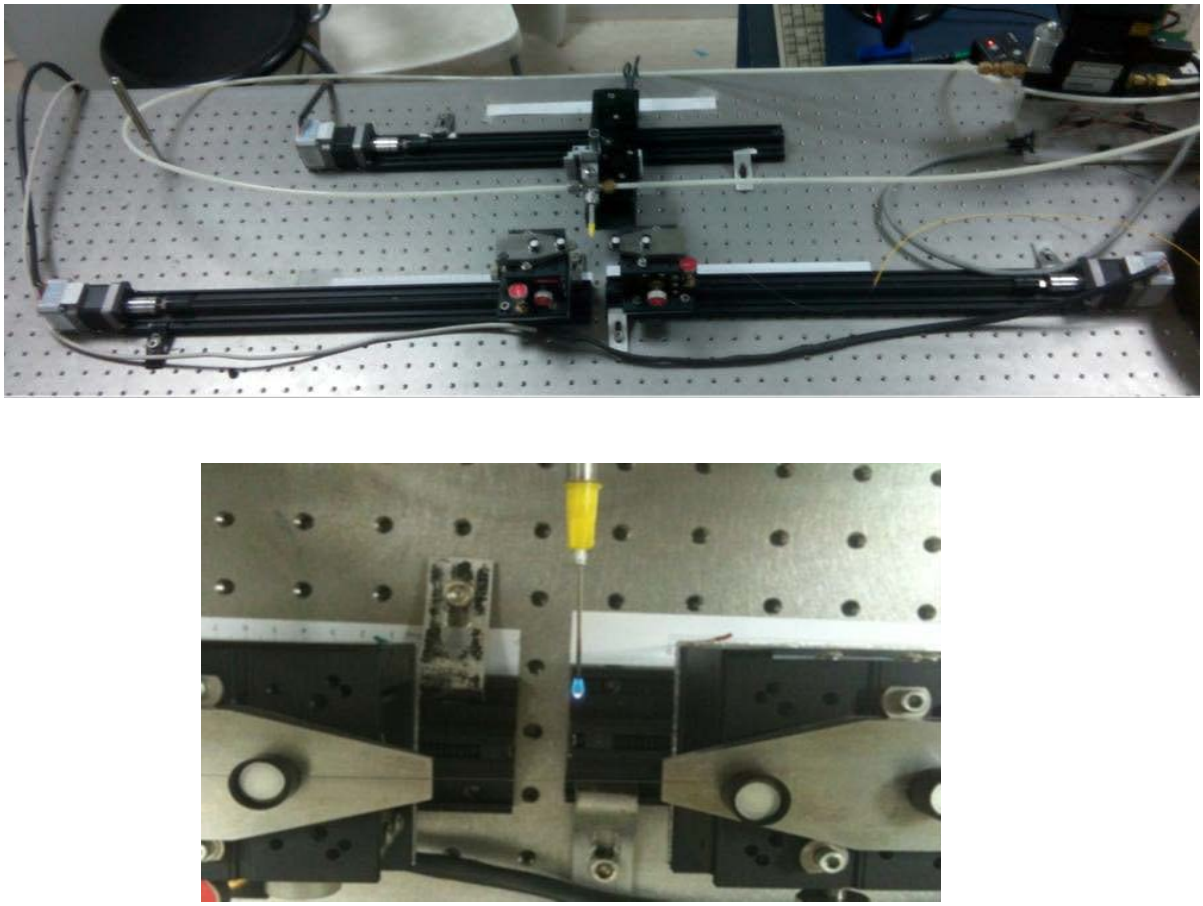

Figure 3-6. Tapering setup.

However, it should be stressed that various conditions in the tapering process of such delicate fibers have imposed difficulties in smooth tapers fabrication. During the experimental tapering process it was noticed that breakup of the inner metal core or also the formation of isolated microspheres (Figure 3-7) could easily occur in un-optimized conditions. This could be attributed to instabilities induced by the temperature profile of the flame or by spatial irregularities of the core's surface. Such

instabilities in fluidic systems have been investigated in various material systems [64], [79], [80] and in fiber platforms [62], [81].

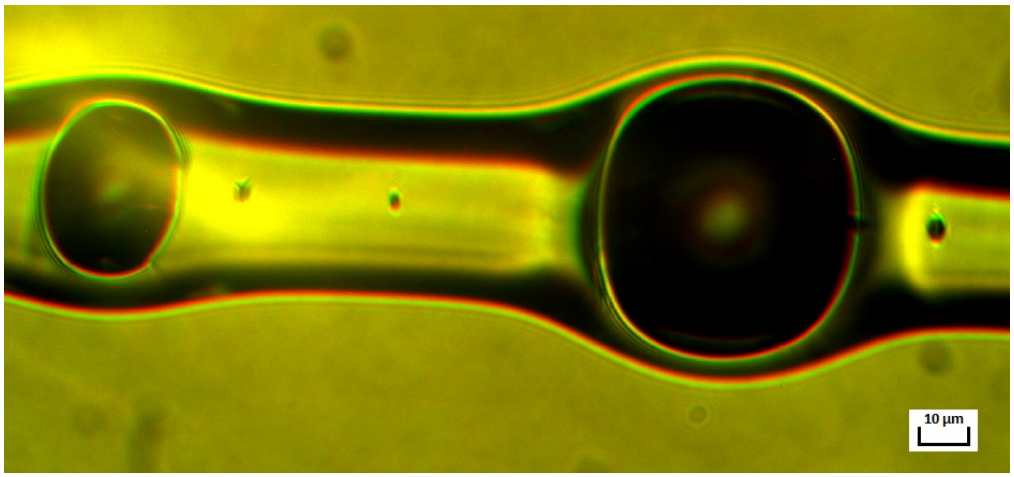

Figure 3-7. Microscope images of formed spheres from fibers with initial core radius of 2µm (left) and 3µm (right).

3.5.1 Instability Analysis

The key parameter describing the instability phenomena is the break up time τ_B, of the continuous medium which can be quantitatively estimated using the Tomotika model instability rate (*in*). In this analysis we use Tomotika's stability theory and we consider a gold core surrounded by a large borosilicate glass cladding. The borosilicate glass was chosen due to its temperature compatibility with the gold. The working range of borosilicate glass is between 825 ^{o}C and 1260 ^{o}C, which overlaps with the melting point of gold (1065 ^{o}C). Both the core and cladding viscosities as a function of temperature, $\mu_{gold}(T)$ and $\mu_{glass}(T)$ respectively, are taken into account. The interfacial surface tension, s(T), is considered to be dominated by the surface tension of gold. The analysis is performed for temperatures ≥1065 ^{o}C, for which the gold core is in its liquid form. Tomotika's theory is strictly applicable only when the relative velocity of the jet and surrounding fluid are very low. Hence, for the static case studied here we can use the linear stability analysis of Tomotika, and we can calculate the breakup time τ_B [79] defined as:

$$\tau_B(T) = \frac{1}{in} \qquad (3\text{-}4)$$

where

$$in = \frac{s}{2r\mu_{glass}}(1 - x^2)\Phi(x) \qquad (3\text{-}5)$$

with r being the core radius, x = 2πr/λ. Φ is the function (39) in [82]:

$$\Phi(x) = \frac{N(x)}{D(x)}$$

$$N(x) \equiv I_1(x)\Delta_1 - \{xI_0(x) - I_1(x)\}\Delta_2$$

$$D(x) \equiv \left(\frac{\mu_{metal}}{\mu_{glass}}\right)\{xI_0(x) - I_1(x)\}\Delta_1 - \left(\frac{\mu_{metal}}{\mu_{glass}}\right)\{(x^2+1)I_1(x) - xI_0(x)\}\Delta_2 - \{xK_0(x) + K_1(x)\}\Delta_3 - \{(x^2+1)K_1(x) + xK_0(x)\}\Delta_4$$

where Δ_1, Δ_2, Δ_3 and Δ_4 are functions of x expressed in determinantal forms as follows:

$$\Delta_1 = \begin{vmatrix} xI_0(x) - I_1(x) & K_1(x) & -xK_0(x) - K_1(x) \\ I_0(x) + xI_1(x) & -K_0(x) & -K_0(x) + xK_1(x) \\ \left(\frac{\mu_{metal}}{\mu_{glass}}\right)xI_0(x) & K_1(x) & -xK_0(x) \end{vmatrix}$$

$$\Delta_2 = \begin{vmatrix} I_1(x) & K_1(x) & -xK_0(x) - K_1(x) \\ I_0(x) & -K_0(x) & -K_0(x) + xK_1(x) \\ \left(\frac{\mu_{metal}}{\mu_{glass}}\right)I_1(x) & K_1(x) & -xK_0(x) \end{vmatrix}$$

$$\Delta_3 = \begin{vmatrix} I_1(x) & xI_0(x) - I_1(x) & -xK_0(x) - K_1(x) \\ I_0(x) & I_0(x) + xI_1(x) & -K_0(x) + xK_1(x) \\ \left(\frac{\mu_{metal}}{\mu_{glass}}\right)I_1(x) & \left(\frac{\mu_{metal}}{\mu_{glass}}\right)xI_0(x) & -xK_0(x) \end{vmatrix}$$

$$\Delta_4 = \begin{vmatrix} I_1(x) & xI_0(x) - I_1(x) & K_1(x) \\ I_0(x) & I_0(x) + xI_1(x) & -K_0(x) \\ \left(\frac{\mu_{metal}}{\mu_{glass}}\right)I_1(x) & \left(\frac{\mu_{metal}}{\mu_{glass}}\right)xI_0(x) & K_1(x) \end{vmatrix}$$

Using the equations of the general case of Tomotika model we can calculate τ_B as a function of the temperature (Figure 3-8(a)). In the case studied here the ratio of the core to cladding viscosity tends to zero ($\mu_{gold}/\mu_{glass} \rightarrow 0$) which according to the Tomotika model leads to a maximum instability for $x \rightarrow 0$, or accordingly for perturbation wavelength λ much larger than the radius of the core (which typically is ≈3μm). As the temperature decreases the viscosity of the surrounding glass (μ_{glass}) increases exponentially, leading to a stable jet due to the rapid increase of τ_B according to (*3-4*).

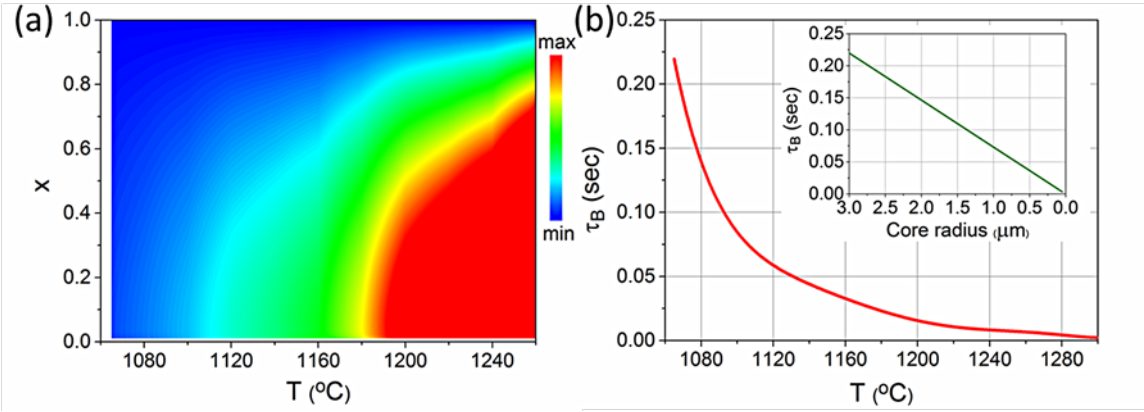

Figure 3-8. a) Instability rate ($1/\tau_B$) as a function of T and x for core radius 3μm. b) Breakup time τ_B as a function of temperature. Inset picture: Breakup time τ_B as a function of core radius at 1065 °C.

When such fibers are tapered down to small core radii the time for which they remain in the heating zone is crucial in order to prevent the breakup of the core. In Figure 3-8 (b) τ_B corresponding to the maximum instability, i.e. to the x that maximizes equation (*3-5*), is presented as a function of the temperature. For 1065 °C, which is the melting point of gold, τ_B is ≈0.22 sec for a 3μm core radius. This value linearly decreases for smaller core radii as shown in the inset diagram of Figure 3-8 (b). Hence, a static heating zone wouldn't be appropriate for the tapering of the fibers as it would lead to the rapid collapse of the core. On the contrary, a moving heating source, such as a moving flame, can be used to successfully taper hybrid fibers.

The flame's temperature profile and distance from the fiber must be adjusted to match the desirable temperature of 1065 °C, as for higher temperatures the instability of the core will increase. The most crucial parameter though is the flame's velocity. Since τ_B is ≈0.22 sec, a high flame velocity is needed. Also as the fiber is tapered down, the core radius decreases and becomes more unstable. Hence the flame's velocity must be adjusted in order to be fast enough to prevent the breakup of the core and slow enough to permit the melting of the metal. Furthermore, due to the system's high instability, a fast tapering process would be preferable. Thus the stages that pull the fiber should have a high velocity to reduce the tapering time.

3.5.2 Microfluidic simulations

For the Finite Element Method (FEM) simulations, COMSOL software was employed to solve the Navier-Stokes equations that describe the velocity field and pressure of the liquid. The level set method was chosen, in which the fluid–fluid interface is represented as the 0.5 contour of the level set function. The level set method was chosen over the moving mesh method, since the topology of the core after its breakup

is of interest. Recent developments on the improvement of the level set method can be found in previous studies [83]–[85]. No-slip walls were set as boundary conditions. Periodic boundary conditions were also used to describe an infinitely long fiber. All the simulations are run with extra fine mesh and for times up to 0.3 s, since for higher times the model does not converge. Furthermore, since the length scales considered here are well below the capillary length, λ_c = 2.55 mm, the gravitational effects are neglected. This assumption was supported also by the fact that in the experimental results no signs of gravitational effects were obvious, since the fibers were symmetric with respect to the fiber axis after the formation of the spheres.

3.5.2.1 Effect of temperature

In order to test the instability of a gold cylindrical rod with 3 μm radius surrounded by a borosilicate glass cladding, we assume a surface tension perturbation of the following form:

$$s = s_0\left(1 - \left(w * p(t) * \cos\left(\frac{2*\pi*z}{\lambda}\right)\right)\right) \quad (3\text{-}6)$$

where s_0 is the surface tension corresponding to the desirable temperature, w is the width and λ is the wavelength of the perturbation, respectively, and p(t) is a piecewise function that controls the time that the fiber remains under the influence of the perturbation.

Figure 3-9 shows the modelled region of the fiber at different time steps at 1200 ^{o}C and at 1300 ^{o}C. The parameters used are w = 0.008, λ = 200μm and

$$p(t) = \begin{cases} 10^{-2t} & t < 0.2s \\ 0 & t > 0.2s \end{cases} \quad (3\text{-}7)$$

The core at T = 1300 °C breaks ~10 times faster than T = 1200 °C, as expected due to the lower viscosity of gold. Furthermore, the size of the primary sphere does not seem to depend on the temperature, but only on the initial core radius. Simulations were also performed for different temperatures: 1065 °C, 1100 °C, 1150 °C, 1180 °C, 1200 °C, 1250 °C, and 1300 °C. For temperatures up to 1180 °C and for the simulation time of 0.3s, the final sphere is not formed but still has an ovular shape, and hence the diameter cannot be measured. For temperatures of 1200 °C, 1250 °C, and 1300 °C, the size of the primary sphere diameter is consistently around 14.3 μm, as indicatively shown below in Figure 3-9.

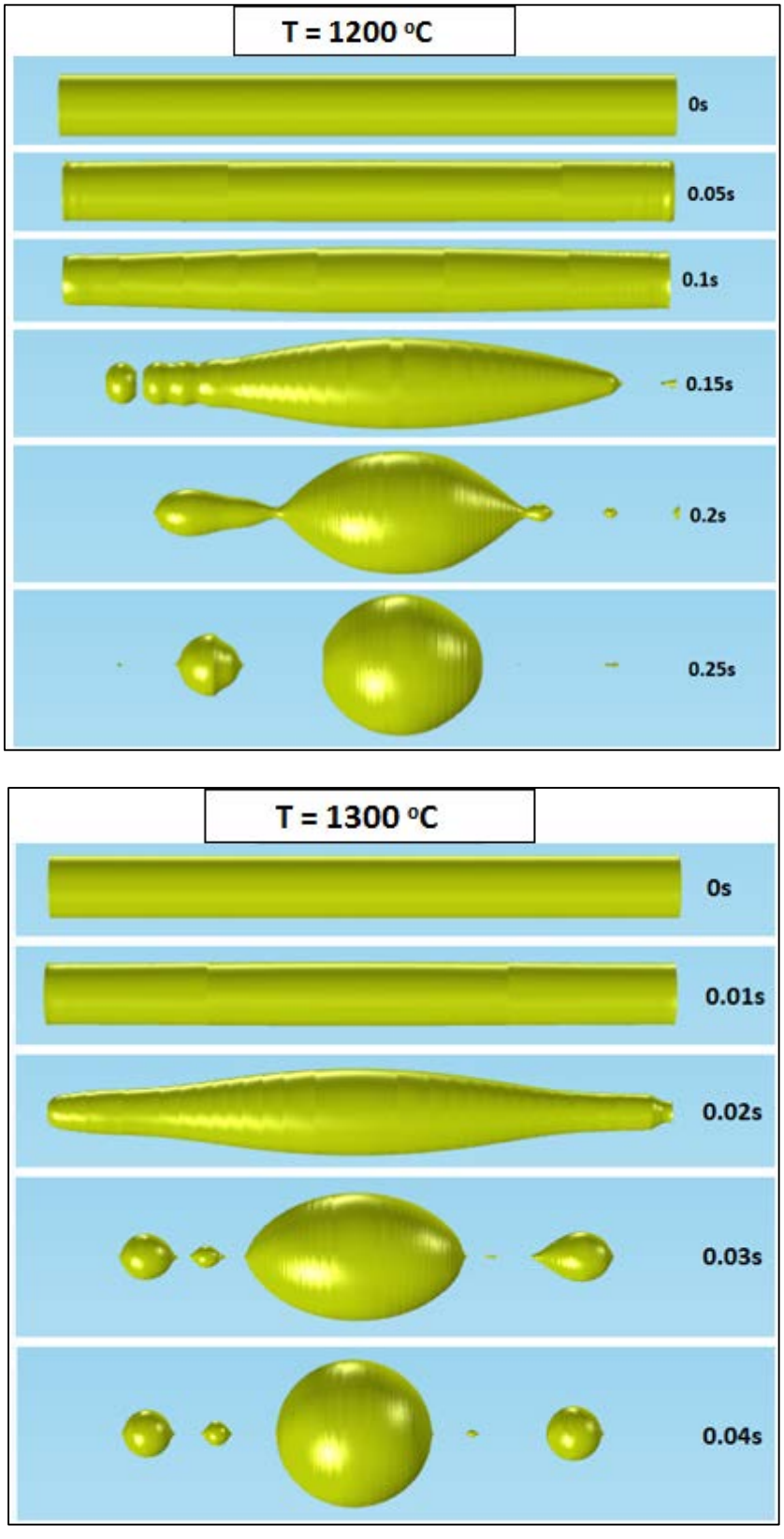

Figure 3-9. Different stages of the PR instability during static heating for different temperatures of a gold cylindrical rod by inserting a surface tension perturbation.

Figure 3-10 shows τ_B as a function of the temperature. For temperatures lower than ~1150 ^oC the core remains intact for times up to 0.3s. The calculated τ_B is 10 times higher than the one calculated from Tomotika model. This could be attributed to the fact that Tomotika model assumes an unbound surrounding fluid.

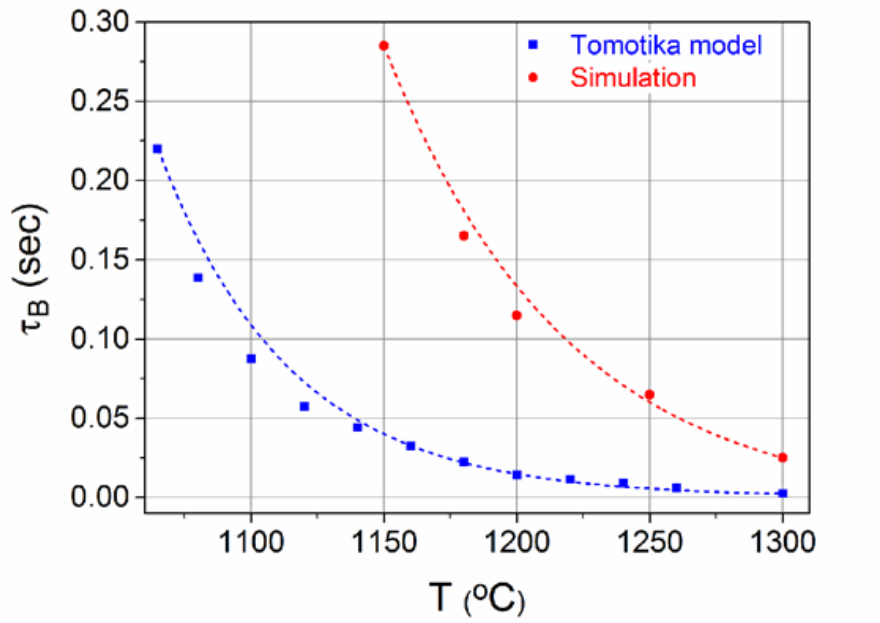

Figure 3-10. Breakup time as a function of temperature calculated using simulations (red) and Tomotika model (blue).

3.5.2.2 *Effect of initial core radius*

Simulations were also performed for the calculation of τ_B for different initial core radii. The temperature for the simulations was 1200 ^oC and as seen from Figure 3-11 (a) τ_B is a linear function of the core radius which is in agreement with what is expected from the Tomotika model.

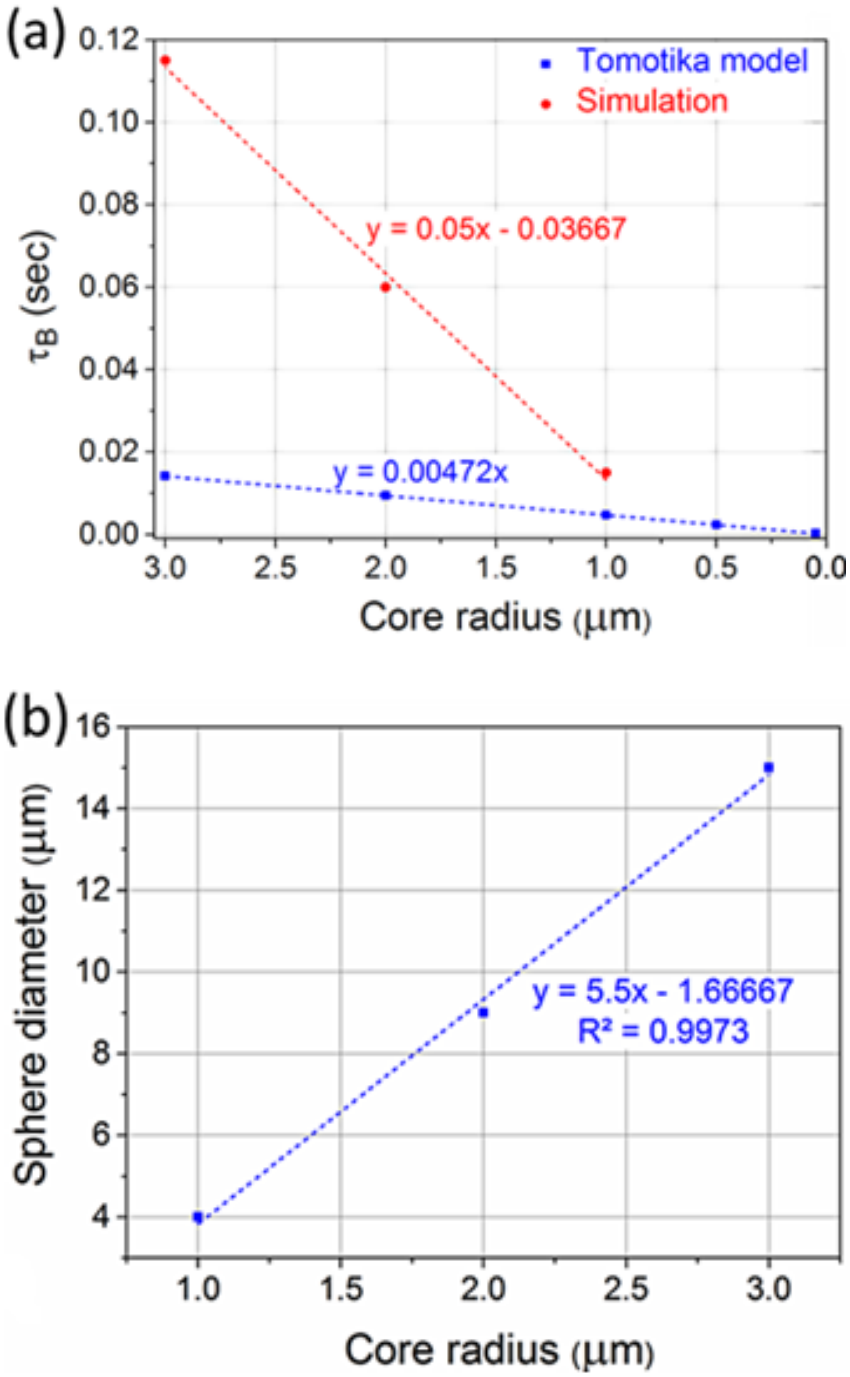

Figure 3-11. a) Breakup time as a function of the initial core radius at T = 1200 °C calculated using simulations (red) and Tomotika model (blue). b) Sphere diameter as a function of the core radius.

Furthermore the diameter of the formed spheres is also a linear function of the core radius as shown in Figure 3-11 (b). The temperature for the simulations was 1200 °C, although the final sphere diameter does not seem to depend on the temperature, as has been indicated by the discussion above, in Figure 3-9, where for temperatures of

1200 °C, 1250 °C, and 1300 °C, the size of the primary sphere diameter is consistently around 14.3 µm. Although this conclusion cannot be fully validated at this stage it can be intuitively explained as follows. The sphere diameters do not depend on the intermediate transient effects, which differ as functions of temperature, but on at the final equilibrium condition set by the structure's geometrical characteristics.

Figure 3-12 shows microscope images of spheres formed from fibers with different initial core radii. Specifically, the spheres were obtained when the temperature and the velocity of the flame were 1200 °C and 2 mm/s, respectively. The diameters of the spheres are approximately 12 µm and 17 µm for 2 µm and 3 µm initial core radii, respectively, a result close to the simulations, where the corresponding diameters were ~9 µm and ~14.3 µm (Figure 3-11 (b)). The distance between the spheres is ~37 µm, while for the simulated ones it is 22.5 µm.

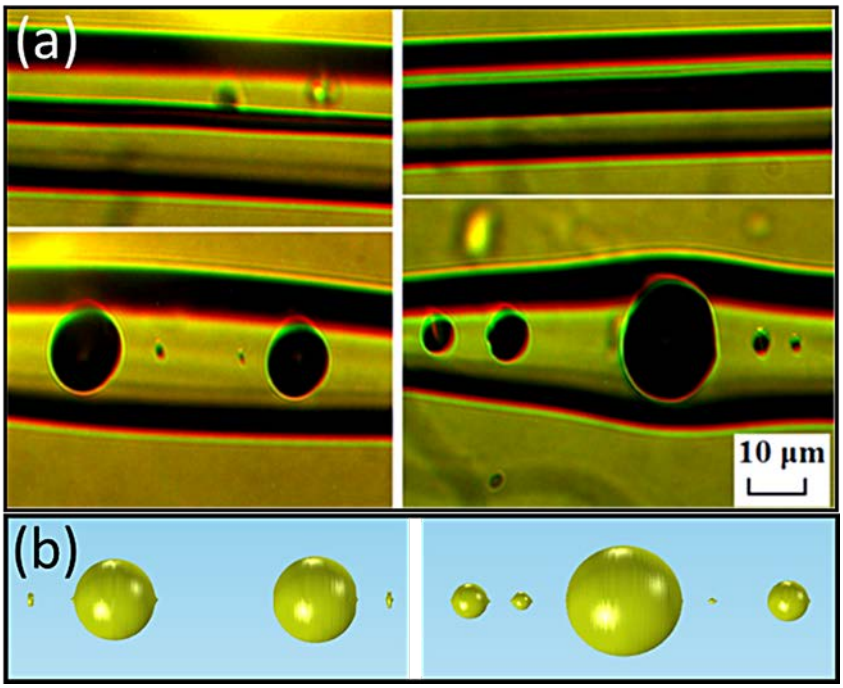

Figure 3-12. (a) Microscope images of formed spheres from fibers with initial core radii of 2 µm (left) and 3 µm (right). (b) The resulting topology of 2 µm (left) and a 3 µm (right) gold core radii.

3.5.2.3 Effect of the width and wavelength of the perturbation

Simulations for surface tension perturbations with different widths and wavelengths were also performed to investigate the differences between the formed microspheres. The temperature is considered 1200 ^{o}C. The surface tension perturbation has the following form:

$$s = s_0\left(1 - \left(w * cos\left(\frac{2*\pi*z}{\lambda}\right)\right)\right) \quad (3\text{-}8)$$

where s_0 is the surface tension corresponding to the desirable temperature, w is the width and λ is the wavelength of the perturbation. Figure 3-13 (a) show the resulting topology for different widths and wavelengths of the surface tension, respectively. Although the distance and size of the primary spheres remains the same, the number and sizes of the formed satellite spheres differs significantly. For the simulations of Figure 3-13 (a) the wavelength was 5μm and the widths 0.008, 0.02 and 0.04. For the simulations of Figure 3-13 (b) the width was 0.008 and the wavelengths 3, 15, 21 and 22 μm.

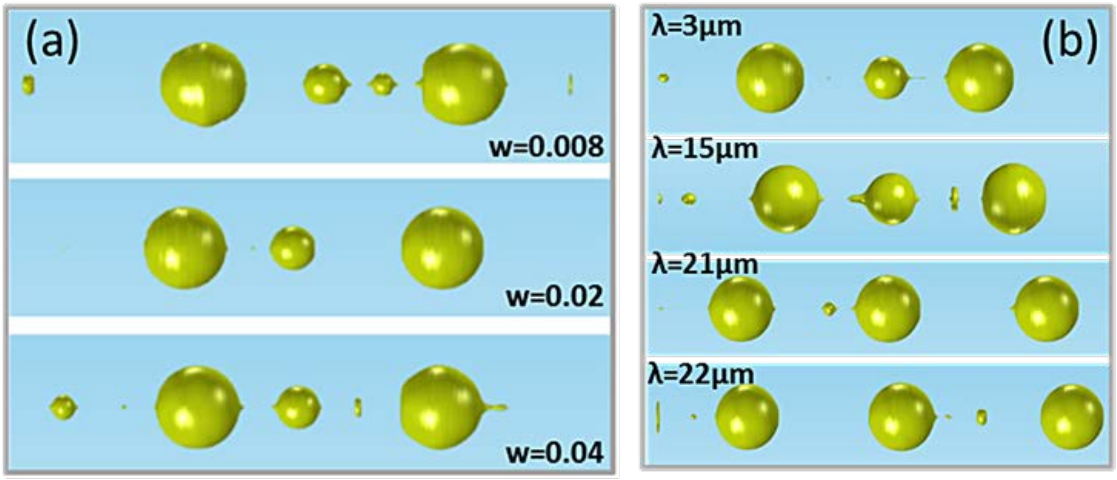

Figure 3-13. a) The resulting topology of a 2μm radius gold core for different widths of the surface tension. b) The resulting topology of a 2 μm radius gold core for different wavelengths of the surface tension.

The diameters of the primary and secondary formed spheres as a function of the wavelength are shown in Figure 3-14 (a) and (b), respectively. Only perturbation wavelengths up to 25 μm are presented due to the computationally limited simulating fiber length. The distance between the primary spheres is related to the diameters of both the primary and secondary spheres. As primary spheres, only the two outer spheres of Figure 3-13 (b) are considered for all the calculations, even when the secondary (middle) sphere reaches the size of the primary. For larger secondary spheres the size of the primary spheres decreases due to mass conservation. Furthermore, a large secondary sphere between two primary spheres means that the breakup points have larger distances between them, leading to larger distances between the two primary spheres. This explains the anti-correlation between the diameter of the primary spheres and their distance (with Pearson and Spearman correlation coefficients -0.84705 and -0.71876, respectively) and the correlation

between the diameter of the secondary spheres and the distance between the primary spheres (with Pearson and Spearman correlation coefficients -0.81517 and -0.85451, respectively), as shown in the inset plots of Figure 3-14. The values of the slopes for the inset plots of Figure 3-14 (a) and (b) are -0.07552 and -0.32299, respectively. With corresponding standard errors (0.00967 and 0.04685, respectively) being less than 20% of the slope values, we can consider the correlation in both plots linear.

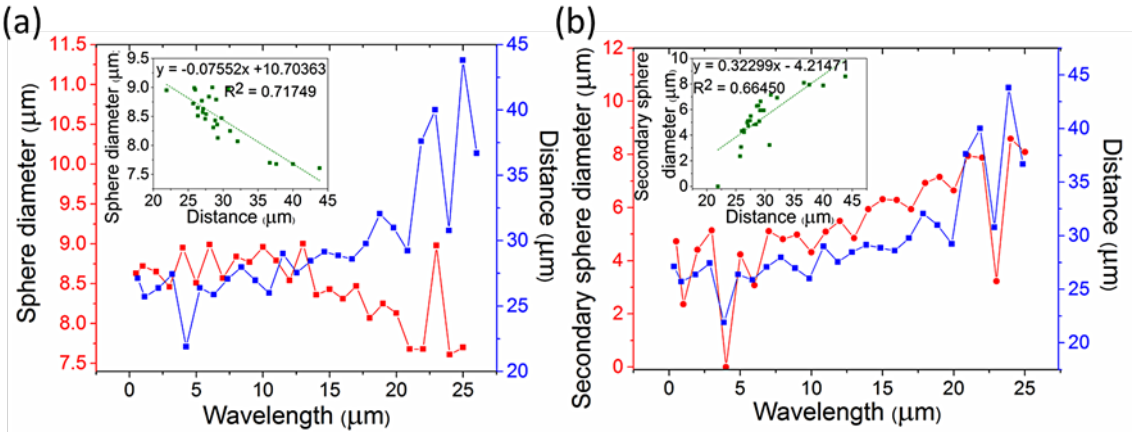

Figure 3-14. (a) Diameter of the primary spheres and distance between them as a function of the perturbation wavelength. (b) Diameter of the secondary sphere and distance between the primary spheres as a function of the perturbation wavelength.

Although the primary sphere diameter and the distance between the primary spheres seem to have a linear anti-correlation, this can only be valid for a rather short range of diameters and distances. The minimum diameter of a sphere is $\sqrt[3]{\frac{3\pi}{2}}D$ (corresponding to a minimum distance of πD), where D is the initial core diameter. For a 4 µm core, the corresponding minimum sphere diameter and minimum distance are D_{min} = 6.3 µm and d_{min} = 12.6 µm, respectively, in the case where only primary spheres exist. When secondary spheres are present, the distance between two primary spheres increase with the wavelength until the size of the secondary sphere reaches the size of the primary, and hence it is also considered as primary (Figure 3-14 (b)). This result is obvious in Figure 3-14 (b), where the diameters of the secondary spheres for long wavelengths are ~8 µm, comparable to the diameters of the primary spheres shown in Figure 3-14 (a). The perturbation wavelength at which three equally sized spheres (D ≈ 8 µm) are formed for an initial 4 µm core is λ~21 µm and the distance between the spheres is d~19 µm, slightly larger than the theoretical D_{min} and d_{min}, probably due to the existence of smaller satellite spheres. This result is also very close to the experimental distance between the spheres, as shown above, where d ≈ 37 µm (Figure 3-12). As shown in Section 3.2.2, the diameter of the primary sphere depends on the

initial core radius and is the same for different temperatures. In Figure 3-14 only small variations of the primary sphere diameters are seen, with an average diameter of 8.84 μm, which is the expected diameter for a 2 μm core radius, as shown in Figure 3-11 (b), where a wavelength of 200 μm was considered, leading to a large distance between the spheres. Hence, for large distances between the primary spheres the primary sphere diameter will remain ~9 μm for a 2 μm initial core radius but the number of the secondary spheres will increase due to mass conservation.

The formation of secondary spheres is in agreement with previously published works, where satellite droplets are observed [64], [79]. Furthermore, we have control over the primary sphere diameter, since, as discussed above, it is only related to the initial core radius. The control of the sphere's diameter over a small range has been previously shown [71], where silica-clad silicon-core fiber with a diameter of 340 nm was continuously fed into a flame, defining an axial thermal gradient; the continuous formation of spheres whose size is controlled by the feed speed was also demonstrated. Due to the limited simulated length though we cannot come to a conclusion concerning the distance between the primary spheres, since only 1–2 spheres are formed in this limited segment.

3.5.2.4 Simulation of the tapering process

The fibers' tapering process was also simulated in order to study the conditions of smooth adiabatic tapering by avoiding the formation of spheres. For the purposes of the simulation a radial velocity was added to the outer glass boundary using deformed geometry. The velocity was set to be:

$$v_r = -0.5(z + 30) \text{ (μm/s)} \qquad (3\text{-}9)$$

with z being the axis along the fiber ranging from -30 μm to 30 μm.

Two different temperatures, 1065 °C and 1200 °C, were investigated. The simulation time was 0.3 s. The results are shown in Figure 3-15 (a). At 1065 °C a smooth taper is obtained, while at 1200 °C the metal core breaks into spheres. Even though the velocity is rather high compared to the experimental procedure, it was chosen in order to test the behavior of the core when its diameter reduces drastically. Even higher velocities result in the formation of smooth tapers for T = 1065 °C (Figure 3-15 (b)). For lower velocities the simulation should run for longer time scales in order to reach the same diameters, which are limited due to convergence issues. However, lower and higher velocities were also simulated, giving the same results, i.e., smooth tapers at 1065 °C and core breakup at 1200 °C.

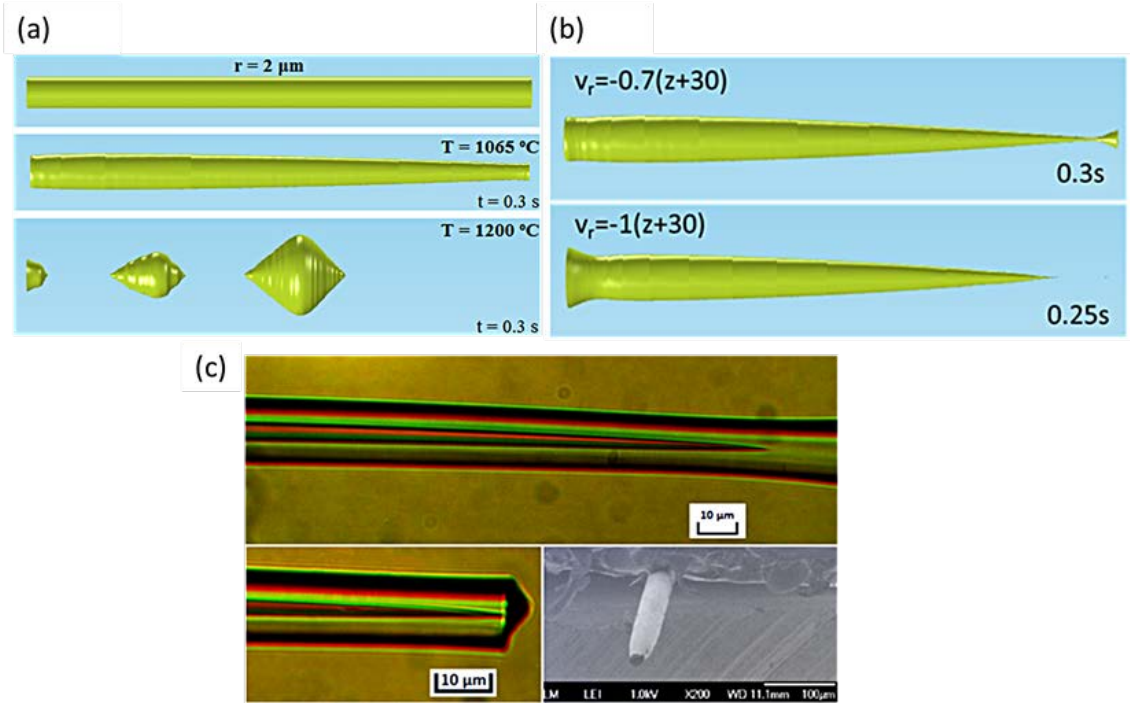

Figure 3-15. (a) Simulation of the tapering process of a 2 µm core radius microfiber at 1065 °C and 1200 °C with vr = -0.5 (z+30) (µm/s), showing the core's evolution after 0.3 s. (b) Simulation of the tapering process of a 2 µm core radius microfiber at 1065 °C for higher radial velocities. (c) Top: Optical microscope images of a fabricated fiber tip before cleaving. Bottom: Optical microscope (left) and SEM (right) characteristic images of a fabricated fiber tip after the cleaving process.

The performed simulations and the study of instabilities in the heated microwires provided very useful and intuitive guidelines for the appropriate thermal treatment in the tapering process. Indeed, when the lowest possible temperature (~1065 °C) combined with high flame velocity (6 mm/s; "fast and cold method") were employed in the experimental tapering process smooth adiabatic tips were successfully fabricated (Figure 3-15 (c)).

3.6 Characterization of Metal Core/ Glass Cladding Tips

During the experimental procedure the key tapering parameters such flame temperature and speed were carefully optimized and selected, thus allowing the fabrication of smooth adiabatic tapers, by controllably avoiding embedded microspheres formation. Figure 3-16 shows optical microscope and Scanning Electron Microscopy (SEM) images obtained from SEM instrument JEOL JSM -7401f FESEM- of a tapered microfiber with initial core and cladding diameters of 4µm and 31µm, respectively. After the taper fabrication the ends of the fiber must be cleaved to allow its further characterization. The best method for cleaving the fiber ends is by using

Focused Ion Beam (FIB) techniques, however in order to avoid this complicated and time consuming method the tapered fibers were cleaved here by using a simple ceramic tile. It should be stressed that the fact that a simple hand held ceramic tile could be used for cleaving demonstrates the ease of handling as well as the mechanical robustness of these fiber tapers.

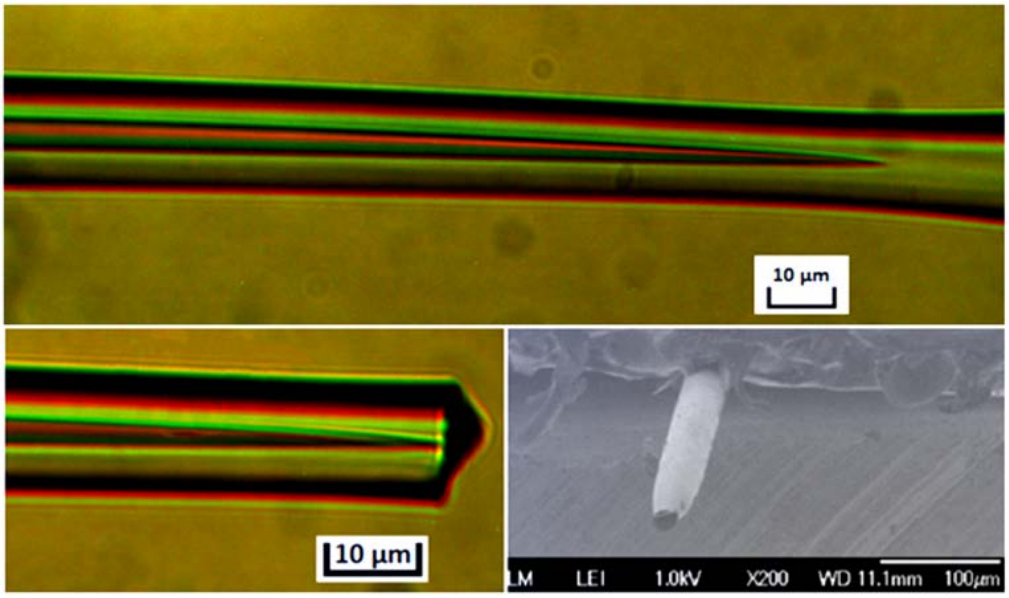

Figure 3-16. Up: Optical microscope images of a fabricated fiber tip before cleaving. Down: Optical microscope (left) and SEM (right) characteristic image of a fabricated fiber tip after the cleaving process.

The mode profiles of the pristine un-tapered and tapered fibers were extracted using a 60X objective lens and a scanning slit optical beam profiler (Thorlabs BP209-VIS/M) in order to image the near-field intensity distribution at the fiber output. For the excitation a 532 nm laser is used and light is coupled to the microfiber with a 40X objective lens. Figure 3-17 shows a schematic representation of the setup.

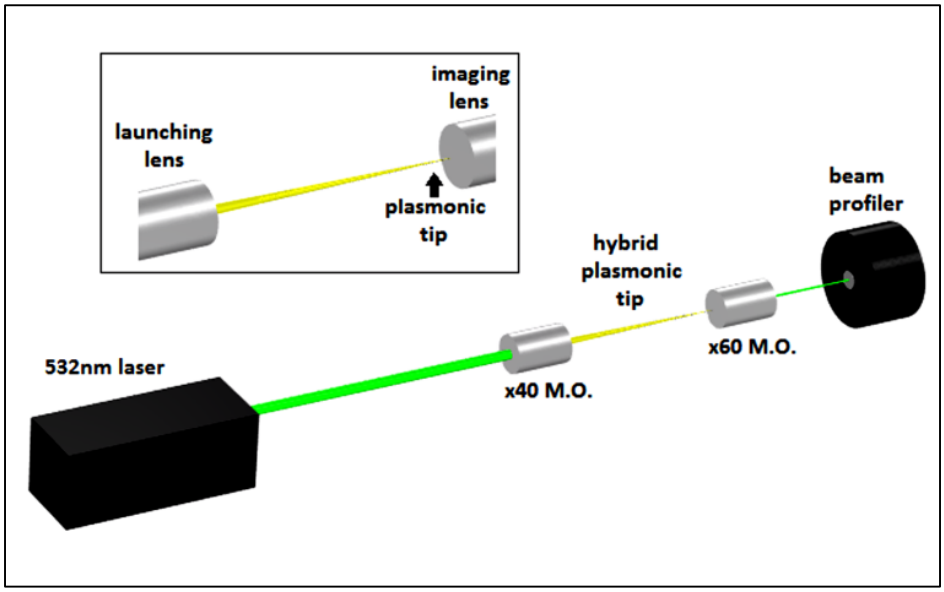

Figure 3-17. Schematic representation of the characterization setup.

As aforementioned, at the current stage of fiber production the microwires have discontinuous metal cores at long lengths while only limited segments of 3-4 cm of continuous core were identified for this study. Such discontinuous microwires of relatively long lengths were evaluated also in terms of propagation, and they exhibited uniform and low loss propagation characteristics as demonstrated by coupling with visible light at 671 nm and 532 nm. Typical gold core microfibers with core and cladding diameters of 4 µm and 30 µm were butt coupled and visually characterized providing light propagation over a relatively long length of 12 cm by guiding at microfiber's glass cladding (Figure 3-18).

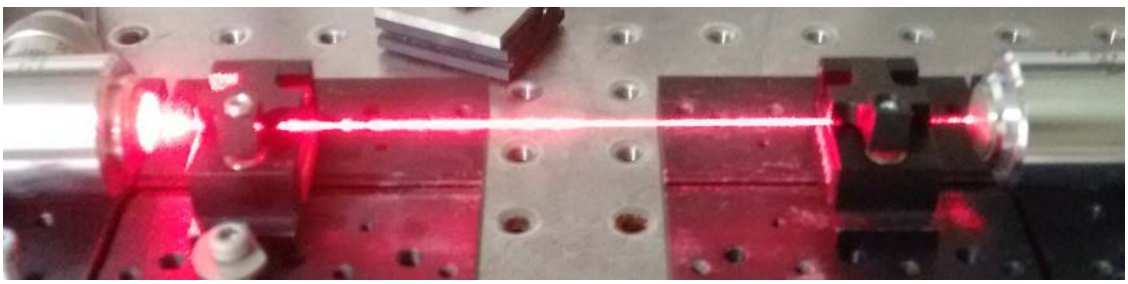

Figure 3-18. Visible light (671 nm) propagation in a 12 cm long segment of discontinuous core microwires.

In Figure 3-19 the mode profile of the microfiber before (a) and after (b) the tapering process is presented. The mode profile of the pristine / untapered microfiber (Figure 3-19 (a)) matches with the profile of the TM_{01} mode shown in Figure 3-2 having two

intensity peaks corresponding to the gold/glass interface and it was obtained after propagation along a 12cm long fiber. The conservation and imaging of the plasmon mode at the end face of the microfiber in Figure 3-18, after such a long propagation length, and despite the plasmon losses and the strong discontinuities of the metal core, is a result of the mode re-excitation mechanism. The relatively high intensity in the middle of the gold core is due to non-optimum cleave performed by a standard ceramic tile. On the contrary the tapered microfiber has one sharp intensity peak (Figure 3-19 (b) and Figure 3-20) and matches with the near field calculated from the simulations (Figure 3-4 (b)).

Since two separate intensity peaks are not observed in the mode profile of the tapered fiber, the diameter must be less than 380 nm which is the resolution of the 60X objective lens that was used for the imaging. The exact diameter of the core at the tip apex though cannot be measured directly by SEM images due to the surrounding dielectric cladding. However, an accurate estimation can be based on the uniform tapering semi-angle of ~3˚, by assuming that a 4μm diameter gold core tends to zero after a length of ~38 μm resulting in a gold tip with a very small radius surrounded by a large radius silicate glass cladding.

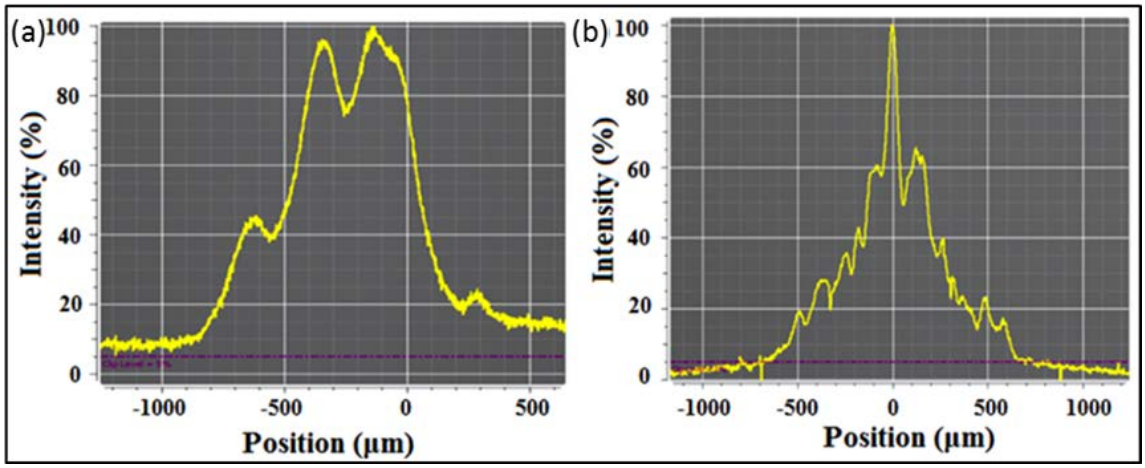

Figure 3-19. Recorded mode profile of a gold core microfiber before (a) and after (b) the tapering process.

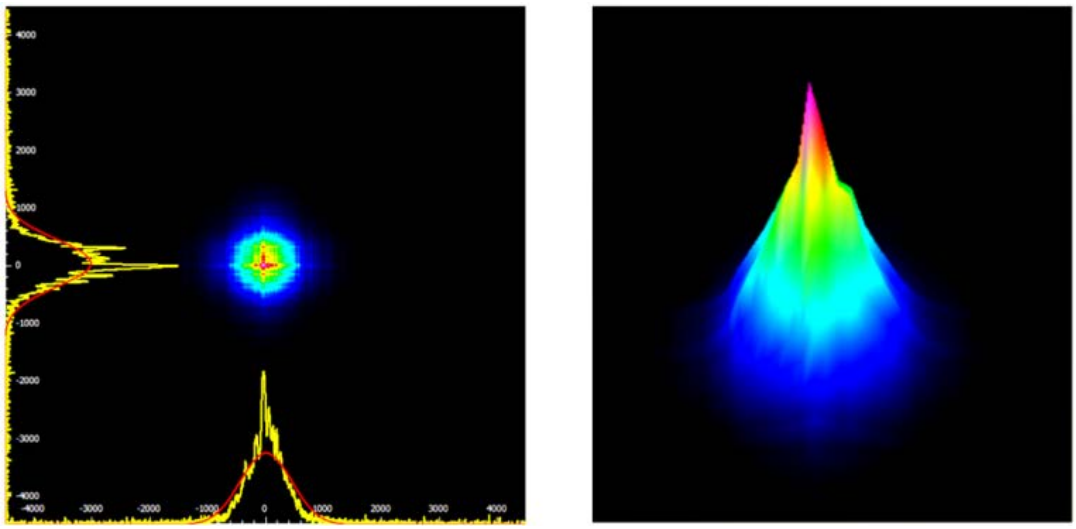

Figure 3-20. 2D (left) and 3D (right) recorded near field intensity distribution of a tapered gold core microfiber.

As discussed above due to the high losses and the short propagation length of TM_{01} mode, the high intensity at the apex of the tip observed above is due to the continuous re-excitation of the mode from the light coupled in the glass cladding. For metal tips without glass cladding the direct excitation from a fiber would lead to significant losses reducing dramatically the field enhancement and the overall performance of the structure.

3.7 Conclusion

In this work, a new hybrid platform of metal core/glass cladding microfibers was proposed and investigated both theoretically and experimentally towards the development of robust plasmonic nanotips for light nanofocussing. Borosilicate tubing was chosen for the glass cladding of the microfibers due to the compatibility of its softening point with the melting points of the used metals. The heating and stretching tapering method allowed the successful fabrication of metal tips with the appropriate geometrical characteristics. The ability to control the geometry of the taper ensures the development of adiabatic tips with minimum losses. Furthermore the use of a "fast and cold" tapering approach helps avoid the breaking and collapse of the core during the process by increasing the characteristic break-up time of the metal core and providing thus an adequate time scale for continuous tapering. Theoretical investigations and FEM based microfluidic simulations support the experimental observations and validate the proposed taper fabrication approach. The fabricated tips exhibit high field confinement beyond the diffraction limit at their apex as well as high field enhancement with calculated E_f of 10^5. Furthermore, the continuous re-excitation of the fundamental mode due to the repeated total internal reflection of light at the

glass/air interface limits the losses induced by the metal leading to high field intensities at the tip apex and thus increases the overall performance of the structure and results to even higher E_f. Additionally, compared to bare metal tips, the presence of the glass cladding offers mechanical robustness as well as ease of light coupling.

Chapter 4

Design of Amphiphilic Block Copolymers and Implementation of Optical Fiber Sensors for Efficient Protein Detection

4.1 Introduction

Proteins are a class of major biomolecules that play a crucial role in many areas such as the food industry, biotechnology and medicine. The need for reliable sensing and quantitative control of proteins has fuelled the development of several protein detection methods over the past decades that can provide both sensitivity and selectivity. Photonic biosensors are widely used since they offer various advantages such as immunity to electromagnetic interference, reliability, fast response, large dynamic range and ability to operate in harsh environmental conditions. Various photonic structures have been proposed for biological sensing including optofluidics [86], PR biosensors [53], [87]–[89], photonic crystals [90], fluorescence sensors [91] and photonic resonant optical microcavities [32], [92], [93].

Despite the different approaches, quite often the increased cost and operational complexity limits the applicability of sensors in real applications. The sensing scheme complexity can be balanced by integrating new sensitive materials that can offer increased sensitivity in detection platforms of low cost instrumentation. This approach has led to the design and synthesis of functional materials that offer selectivity as well as efficient adsorption of the molecules under study, enhancing the sensitivity [36], [37]. The combination of the sensing material and a large core optical fiber provide additionally flexibility, mechanical robustness, high degree of miniaturization, as well as long interaction length where their operational characteristics can allow the efficient integration of sensors in measuring units. The deposition of such materials to an unclad portion of multimode polymer [38], [39] or silica [40], [41] optical fiber, which can act as both the sensing and collection element, can result to the development of low cost and low complexity sensors. The selection also of proper interrogation schemes like optical power interrogation in contrast to spectral based detection [41] offers the additional capability of sensing heads integration in autonomous wireless networks for increased monitoring flexibility [42].

The sensing mechanism of the polymer coated optical fibers is based on the variations of the measured power at the distal end of the fiber due to the interaction between the fiber evanescent field and the changes induced to the polymeric film by the adsorption of proteins. The measured power differs when the fiber is immersed to protein solutions of different concentrations enabling a quantitative evaluation of the protein concentration. The formation of thin and uniform polymeric layers is crucial for the development of an accurate sensor with low detection limit due to the small penetration depth of the evanescent wave. Therefore, two different deposition methods were employed in this study, the dip coating technique and direct manual casting for side deposition, in order to find the optimum conditions for the formation of high quality polymeric layers.

For the purpose of the present study, customized amphiphilic block copolymers [94] were specifically designed having both hydrophilic and hydrophobic blocks for the facilitation of protein detection and the efficient adhesion of the polymer overlayer to the optical fiber surface. More specifically, $PMMA_{117}$-*b*-$PDMAEMA_{16}$ and the vinyl-sulfone-functionalized $PMMA_{117}$-*b*-P($DMAEMA_{17}$-*st*-$VSTEMA_2$) amphiphilic block copolymers were prepared using a 'living' polymerization technique [95], reversible-addition fragmentation chain transfer (RAFT) polymerization [96], [97], having both hydrophilic and hydrophobic blocks. Methacrylic monomers were chosen since they are easily polymerized. The hydrophilic PDMAEMA block is protonated at neutral pH and can electrostatically adsorb negatively charged molecules. The existence of vinyl-sulfone double bonds in the chemically modified $PMMA_{117}$-*b*-P($DMAEMA_{17}$-*st*-$VSTEMA_2$) copolymer leads to chemical binding by thiol-ene reaction with cysteine in proteins resulting in permanent immobilization of the proteins [98], [99]. The hydrophobic PMMA, a well-known methacrylic polymer used in biomedical applications, is the non-interacting block and due to its insolubility in water it ensures the formation of stable polymeric films on the fiber surface.

4.2 Experimental

The two synthesized polymers are presented in Figure 4-1 showing the groups that interact with the BSA protein. The PDMAEMA block of the $PMMA_{117}$-*b*-$PDMAEMA_{16}$ amphiphilic block copolymer is extensively protonated at low pH leading to electrostatic binding of negatively charged BSA molecules to the dimethylamino group. The presence of vinyl-sulfone double bonds to the $PMMA_{117}$-*b*-($PDMAEMA_{17}$-*st*-$VSTEMA_2$) additionally leads to chemical binding by thiol-ene reaction with cysteine in proteins.

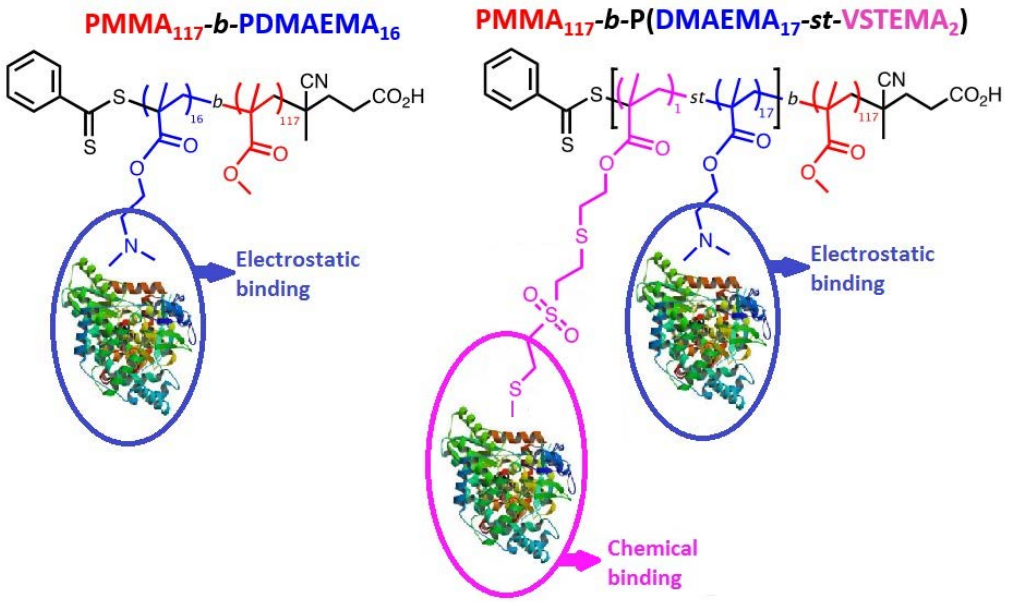

Figure 4-1. The two synthesized polymers and the corresponding groups interacting with the BSA protein.

4.2.1 Sensors' development

For the development of fiber optic sensing heads, large core and multimoded silica optical fibers of 600 µm silica core (FT600EMT, purchased from Thorlabs) with removable polymer was used. For the functionalization of the fibers, both the jacket and the cladding were mechanically removed over a length of 4 cm exposing the core. The exposed region was cleaned with acetone and dried before the deposition of the polymeric material. The block copolymer solutions were deposited on the exposed silica cores of the fibers using either direct side polymer deposition or the dip coating technique. For the deposition, block copolymer solutions of 1.0% w/v, 0.5% w/v and 0.2% w/v concentration were used. After the polymeric layer deposition, the sensing region of the fiber was immersed into a buffer solution at pH 7 to get a positively charged surface on the top of the polymeric film which could adsorb the negatively charged at neutral pH BSA protein. Figure 4-2 shows a schematic representation of the procedure described above.

A systematic study for the development of different overlayers on fibers surface was performed in order to identify optimal conditions. The SEM images in Figure 4-2 show that the polymeric films formed with 1.0% w/v $PMMA_{117}$-*b*-$PDMAEMA_{16}$ amphiphilic block copolymer solution using direct side polymer deposition are quite thick (~7 µm) leading to the formation of cracks due to non-optimum bonding with the silica surface.

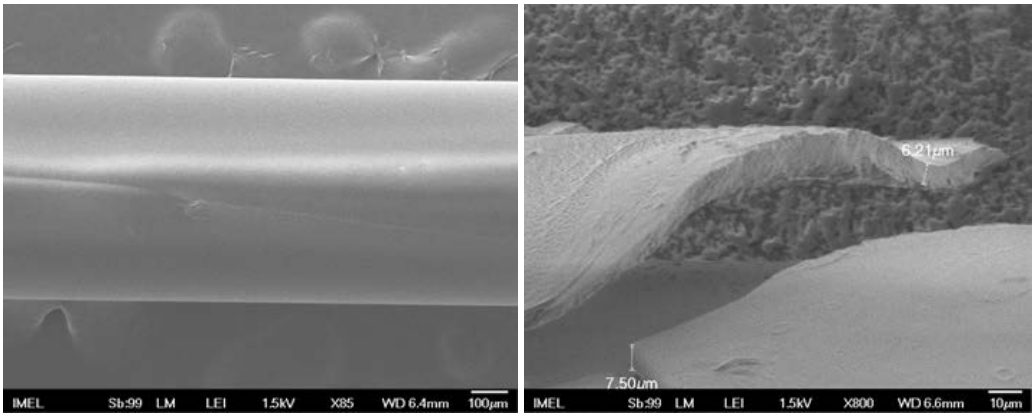

Figure 4-2. SEM images of silica optical fibers covered with $PMMA_{117}$-b-$PDMAEMA_{16}$ amphiphilic block copolymer using direct side polymer deposition.

The side deposition was employed as it would be better suited for the selective deposition of a layer in a predetermined length of the fiber without the need to dip the entire length of the fiber affecting thus the deposition uniformity. However, the control was not optimum resulting thus in thick layers. For the formation of thin and mechanically robust polymeric layers the dip coating technique was then employed. As an initial characterization procedure polymeric layers of $PMMA_{117}$-*b*-$PDMAEMA_{16}$ solutions with different concentrations were deposited on glass slides with dip coating in order to measure the film thickness with a profilometer (Alpha-step IQ). The evaluation was performed using glass slides since the thickness of the polymeric film could not be measured directly on the fiber's surface with the profilometer as a result of the curvature of the fiber surface. Figure 4-3 shows the linear dependence between the film thickness and the concentration of the $PMMA_{117}$-*b*-$PDMAEMA_{16}$ solution, as well as the number of dips. The films obtained with the dip coating technique are very thin, with thicknesses ranging from ~20 nm to ~75 nm for $PMMA_{117}$-*b*-$PDMAEMA_{16}$ solutions of 0.2% w/v and 1% w/v, respectively, for a single dip.

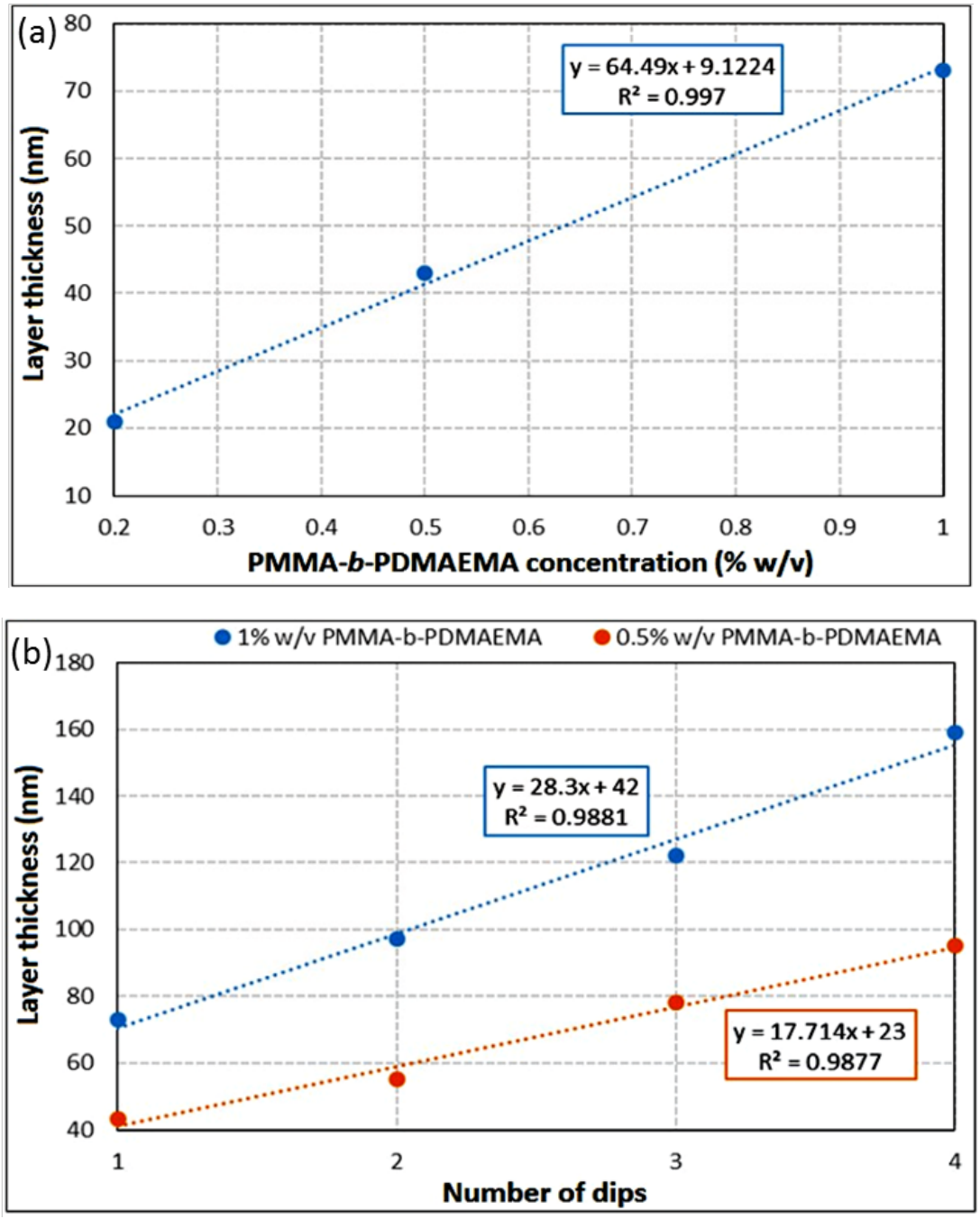

Figure 4-3. Thickness of the PMMA$_{117}$-b-PDMAEMA$_{16}$ polymeric film as a function of the PMMA$_{117}$-b-PDMAEMA$_{16}$ solution concentration (a) and of the number of dips (b).

SEM characterization of an optical fiber coated with 0.2% w/v PMMA$_{117}$-*b*-PDMAEMA$_{16}$ solution were also performed in order to measure the thickness of the polymeric layer (Figure 4-4). The thickness was ~30 nm and it was measured on a cross-section of the fiber parallel to the fiber's axis. The fiber, due to its large diameter behaves similarly to a flat surface, hence the measured film thickness is close to the value measured on the flat surface of the glass slide.

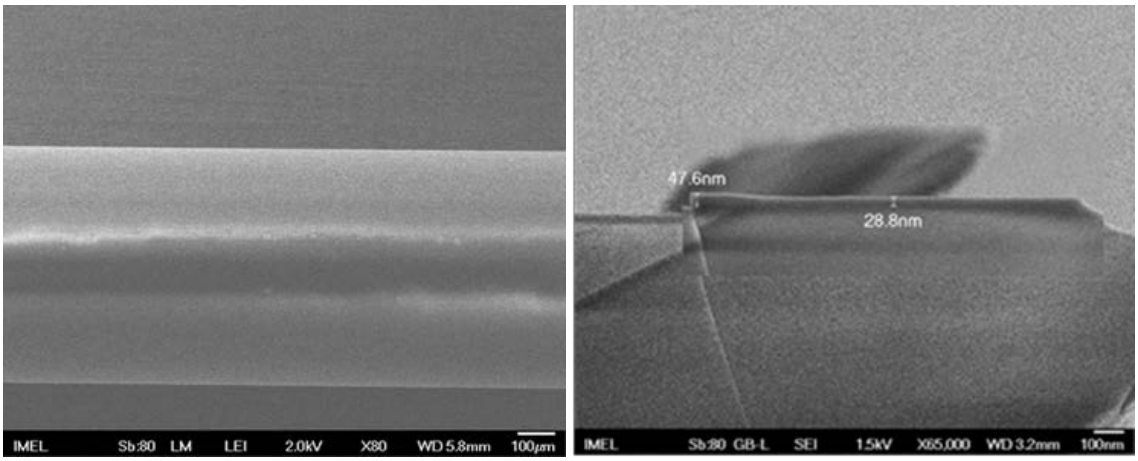

Figure 4-4. SEM images of silica optical fibers covered with 0.2% w/v $PMMA_{117}$-b-$PDMAEMA_{16}$ amphiphilic block copolymer solution using the dip coating technique for the deposition of the polymer.

4.2.2 Experimental setup

The experimental setup for sensing heads characterization consists of a functionalized silica fiber connected to a Thorlabs M625F1 LED light source operating at 650 nm with maximum output power of 10 mW. The sensing region of the fiber is immersed in solutions with different protein concentrations and the signal is recorded at the fiber's distal end by a Thorlabs PM100D power meter connected to a computer. The setup is presented schematically in Figure 4-5.

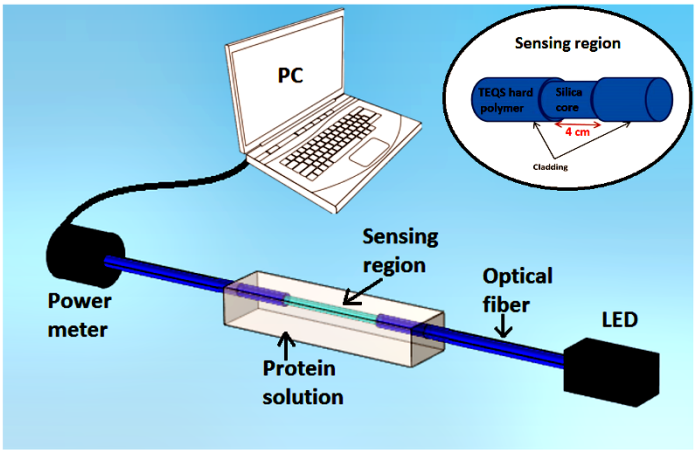

Figure 4-5. Schematic representation of the experimental setup.

Due to the opposing charges of the sensing material and the measured protein, the protein is electrostatically bound onto the polymeric layer. The protein adsorption from the copolymer at the fiber's surface changes both the refractive index as well as the thickness of the film. Due to the interaction between the evanescent field and the polymeric film these changes cause a variation in the output power measured at the fiber's distal end.

4.3 Results and Discussion

For the protein detection experiments optical fibers coated with both $PMMA_{117}$-*b*-$PDMAEMA_{16}$ and $PMMA_{117}$-*b*-P($DMAEMA_{17}$-$VSTEMA_2$) copolymers were evaluated over different BSA concentrations in buffer solutions. The buffer solution was used in order to simulate the acidity and salinity of the biological liquids. The coated fibers are firstly immersed in buffer solution to take the reference intensity value (I_{ref}). Then the sensor's response, defined as:

$$Response\ (\%) = \frac{I_{sig}-I_{ref}}{I_{ref}} \times 100 \quad (4\text{-}1)$$

where I_{sig} the intensity measured for a BSA solution, is calculated.

4.3.1 Performance of the $PMMA_{117}$-*b*-$PDMAEMA_{16}$ block copolymer

The first experiments were performed with optical fibers coated with 1% w/v $PMMA_{117}$-*b*-$PDMAEMA_{16}$ amphiphilic block copolymer solution using direct side polymer deposition. The fiber was immersed in BSA solutions with different concentrations. After each immersion the fiber was washed with buffer solution. The results are presented in Figure 4-6 (a).

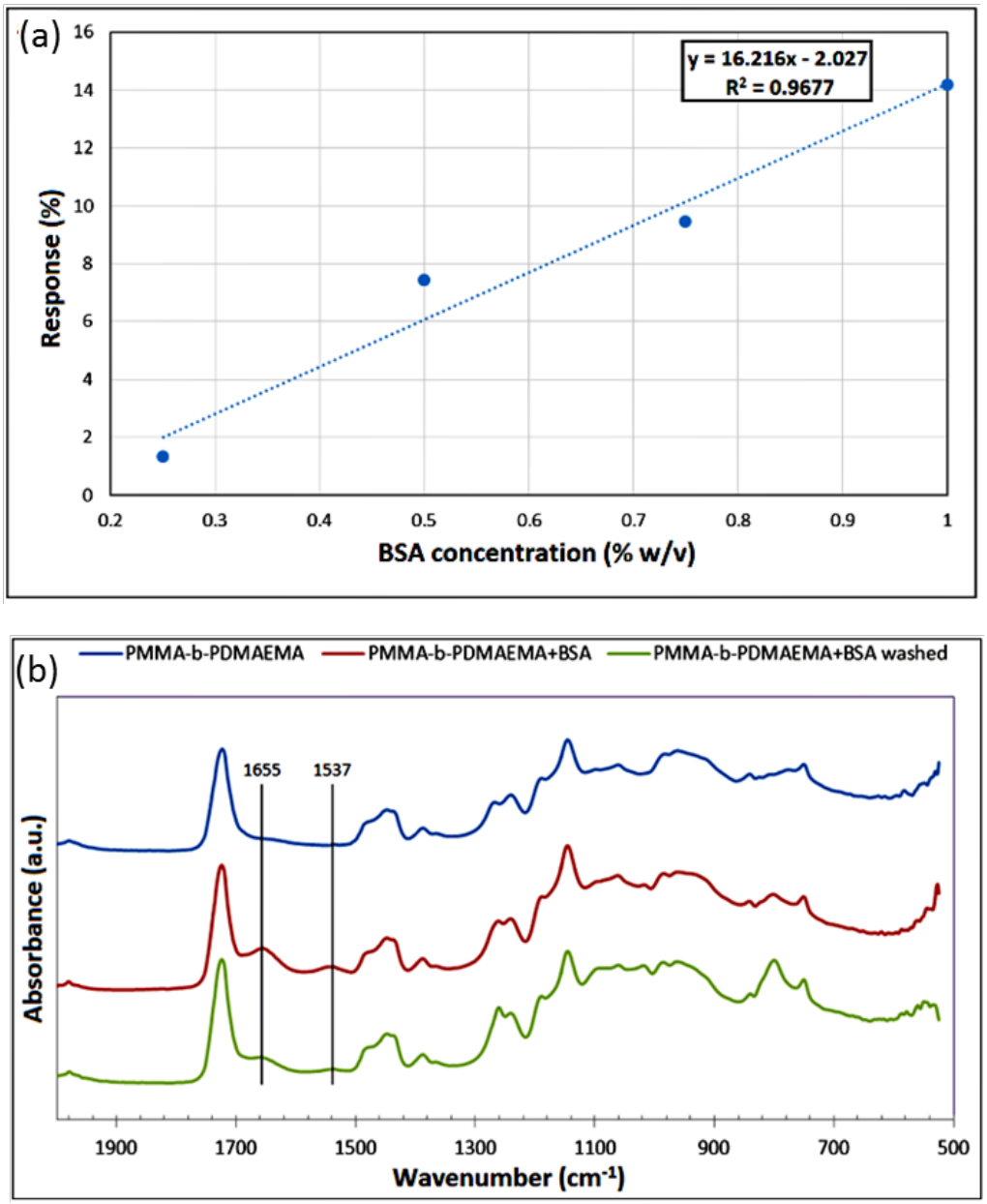

Figure 4-6. a) Absolute response for different BSA concentrations of an optical fiber coated with 1% w/v $PMMA_{117}$-b-$PDMAEMA_{16}$ amphiphilic block copolymer solution using direct side polymer deposition resulting in an overlayer thickness of ~7 µm. b) ATR-FTIR spectrums of the fiber sensor coated with $PMMA_{117}$-b-$PDMAEMA_{16}$ polymer before (blue) and after (red) BSA absorption. The green line is the spectrum after washing the sensor with the absorbed BSA with buffer solution.

Such thick overlayers (~7 µm) were efficient for monitoring only high BSA concentrations ranging from 0.25% w/v – 1% w/v, limiting the sensitivity by the weak interaction between the evanescent field and the protein due to the high film thickness.

An extensive ATR-FTIR analysis was performed to confirm the presence of the BSA's absorption bands (amide bond frequencies at 1655 and 1537 cm^{-1}) and thus prove that the protein is efficiently adsorbed by the $PMMA_{117}$-*b*-$PDMAEMA_{16}$ copolymer (Figure 4-6 (b)). Despite the reversible electrostatic binding mechanism we noticed that after washing the fiber there was still a residual presence of BSA on the polymeric film.

In order to increase the detection limit and to avoid the degradation of the layer, the experimental procedure was repeated with an optical fiber coated with 0.2% w/v $PMMA_{117}$-*b*-$PDMAEMA_{16}$ amphiphilic block copolymer solution using the dip coating technique for the deposition. The sensor's response as presented in Figure 4-7 (a) shows that the detection limit was indeed decreased by one order of magnitude (BSA concentrations ranging from 0.025% to 0.1% w/v) due to the thin polymeric layer. Furthermore, due to the improved quality of the film, the sensor exhibited good reversibility. The response presented is not linear due to the fact that the fiber was not washed after each immersion.

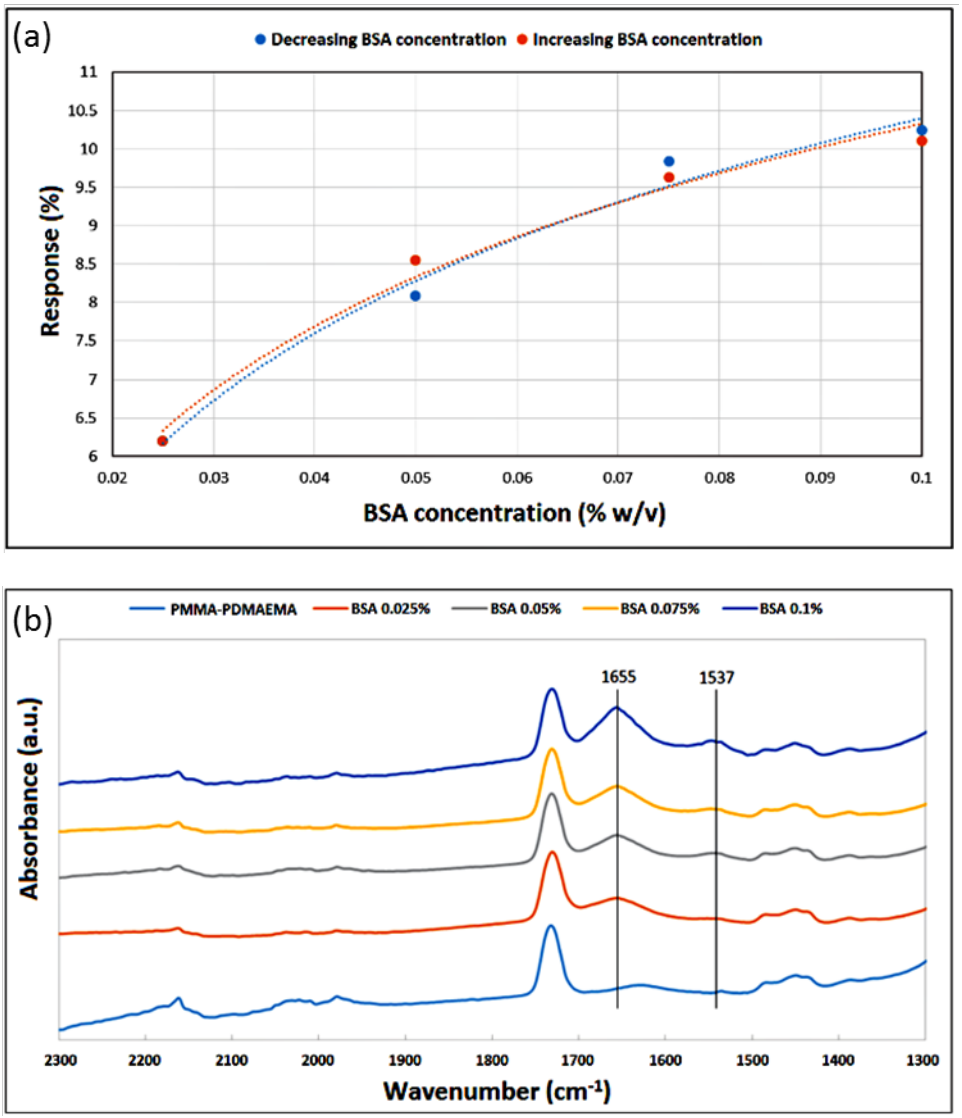

Figure 4-7. a) Absolute response for different BSA concentrations of an optical fiber coated with 0.2% w/v $PMMA_{117}$-b-$PDMAEMA_{16}$ amphiphilic block copolymer solution using the dip coating technique resulting in an overlayer thickness of ~30 nm. b) ATR-FTIR spectrums after immersion to solutions with different BSA concentration.

The response of the sensor to different BSA concentrations was also evaluated with ATR-FTIR measurements. Figure 4-7 (b) shows increased BSA adsorption after immersion to solutions with higher BSA concentration.

4.3.2 Performance of the $PMMA_{117}$-*b*-P($DMAEMA_{17}$-$VSTEMA_2$) block copolymer

The experiments were repeated using an optical fiber sensing head coated with 1% w/v $PMMA_{117}$-*b*-P($DMAEMA_{17}$-$VSTEMA_2$) amphiphilic block copolymer solution with direct side polymer deposition resulting in an overlayer thickness of ~7 µm. The $PMMA_{117}$-*b*-P($DMAEMA_{17}$-$VSTEMA_2$) copolymer, due to its vinyl-sulfone double bonds,

should give an additional non-reversible chemical binding mechanism to the negatively charged proteins, further to the cationic group reversible electrostatic mechanism. The fiber was immersed in BSA solutions with different concentrations. After each immersion, the fiber was washed with buffer solution. The results are presented in Figure 4-8 (a).

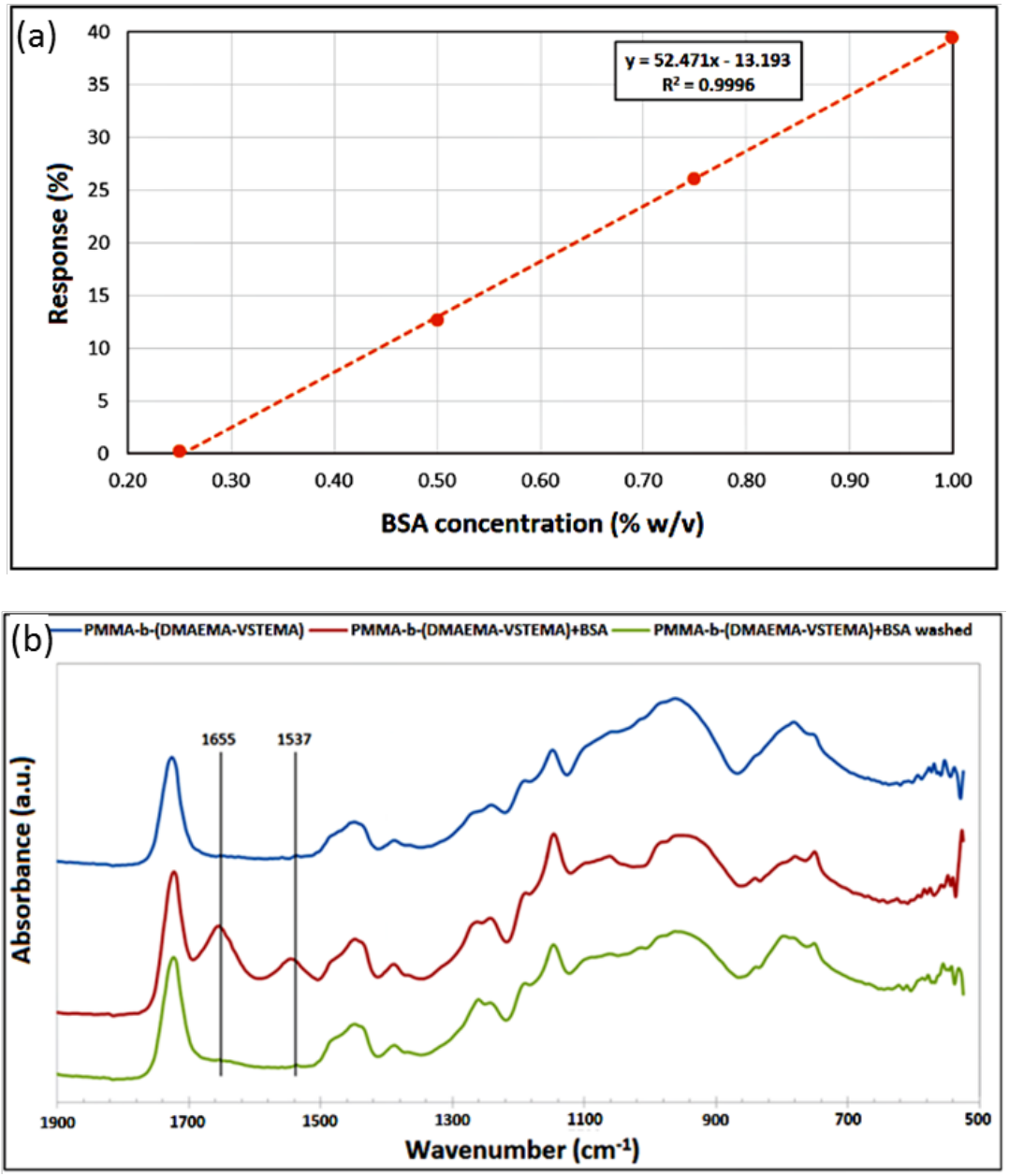

Figure 4-8. a) Absolute response for different BSA concentrations of an optical fiber coated with 1% w/v $PMMA_{117}$-b-$P(DMAEMA_{17}$-$VSTEMA_2)$ amphiphilic block copolymer. b) ATR-FTIR spectrums of the $PMMA_{117}$-b-$P(DMAEMA_{17}$-$VSTEMA_2)$ coated fiber before (blue) and after (red) BSA absorption. The green line is the spectrum after washing the sensor with the adsorbed BSA with buffer solution.

We can confirm that due to additional mechanism of permanent covalent binding, the response of $PMMA_{117}$-*b*-$P(DMAEMA_{17}$-$VSTEMA_2)$ is considerably higher than the response of $PMMA_{117}$-*b*-$PDMAEMA_{16}$ block copolymer (Figure 4-7). However, a direct comparison and the determination of chemical binding contribution would not be possible as there are also other parameters like overlayer thickness and uniformity that affect the responsivity.

In order to verify the $PMMA_{117}$-*b*-$P(DMAEMA_{17}$-$VSTEMA_2)$ sensing performance, ATR-FTIR measurements were also performed. The results, presented in Figure 4-8 (b), demonstrate the clear presence of BSA protein as efficiently adsorbed by the polymer.

However we can observe the drastic decrease of absorption peaks of BSA after washing the fiber with buffer solution despite the fact that the $PMMA_{117}$-*b*-$P(DMAEMA_{17}$-$VSTEMA_2)$ copolymer should lead to permanent immobilization of proteins. This could be attributed to the specific composition of the copolymers as there are only 2/19 units of the hydrophilic block VSTEMA compared to 17/19 of DMAEMA. This implies that only a very small amount of protein is covalently bound compared to that which is electrostatically bound.

It was observed that the excessive use of fiber heads in aqueous solutions was causing a gradual degradation for the relatively thicker films of both $PMMA_{117}$-*b*-$PDMAEMA_{16}$ and $PMMA_{117}$-*b*-$P(DMAEMA_{17}$-$VSTEMA_2)$ block copolymers, in the form of cracks, as is indicatively presented in the SEM image of Figure 4-9. Probably the highly hydrophilic nature of the overlayer can cause a degree of swelling leading to cracks and eventually to overlayers delamination.

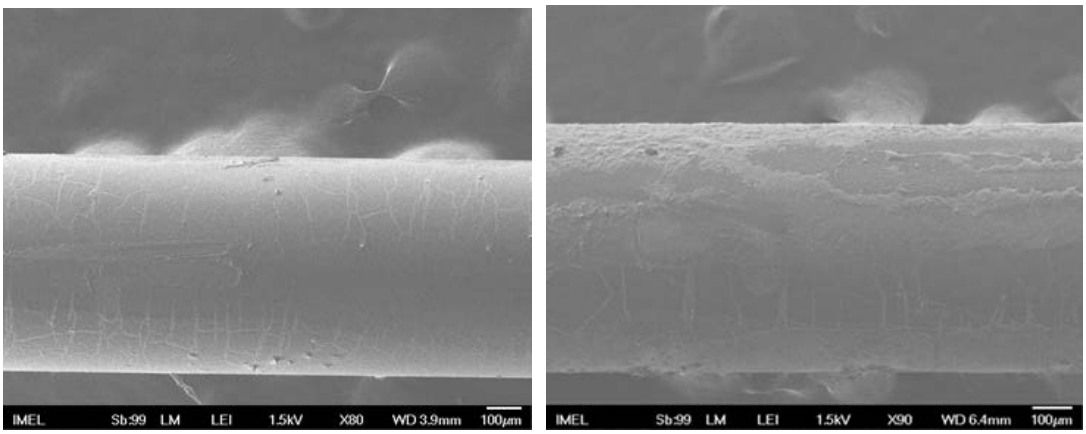

Figure 4-9. SEM images of a fibers covered with $PMMA_{117}$-b-$PDMAEMA_{16}$ (left) and $PMMA_{117}$-b-$P(DMAEMA_{17}$-$VSTEMA_2)$ (right) polymer after the experimental procedure.

Further study is in progress to improve the deposition quality of the layers and optimally tune the hydrophobicity of the anchoring PMMA block for improving the stability and adhesion quality of the overlayer as well as to optimize the hydrophilicity of the interacting blocks in order to enhance the operability on aqueous environment while at the same time improve the stability and reversibility of the sensors.

4.4 Potential applications of polymers in other photonic platforms

Both $PMMA_{117}$-*b*-$PDMAEMA_{16}$ and $PMMA_{117}$-*b*-P($DMAEMA_{17}$-$VSTEMA_2$) block copolymers could also be integrated in other photonic devices to either immobilize the under study molecules or to be used as waveguides.

The polymers could be used as overlayers on PSNRs embedded in the metal coated microfibers discussed in Chapter 2. Especially for SERS applications the immobilization of the under study molecules on the PSNR could lead even to single molecule detection. Figure 4-10 shows the maximum normalized electric field in a polymer coated slot embedded at r = 400 nm of a plasmonic fiber tip with a semi-angle of a = 5.33˚, as a function of the wavelength. The electric field is comparable to the maximum field of an uncoated slot and hence the polymer coating could be used for adsorption of molecules to the PSNR surface without limiting the effectiveness of the resonator.

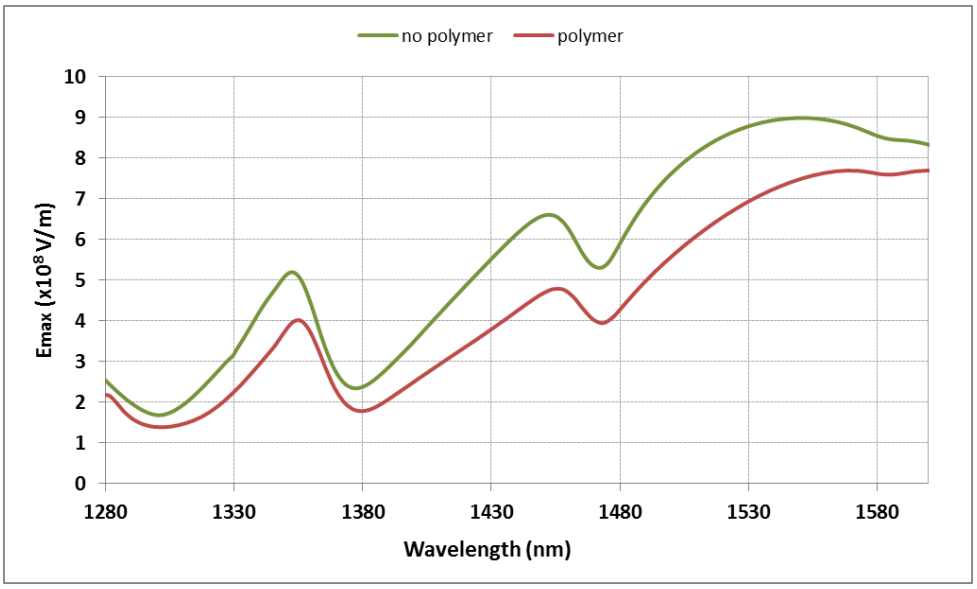

Figure 4-10. Maximum normalized electric field in the slot embedded at r = 400 nm of a plasmonic fiber tip (a = 5.33˚), as a function of the wavelength with (red) and without (green) polymer coating.

4.5 Conclusions

We have demonstrated the characterization of amphiphilic block copolymers containing both hydrophobic and hydrophilic blocks for efficient protein detection. The combination of both blocks in the $PMMA_{117}$-*b*-$PDMAEMA_{16}$ and the vinyl-sulfone functionalized $PMMA_{117}$-*b*-P($DMAEMA_{17}$-$VSTEMA_2$) amphiphilic block copolymer materials leads to the formation of robust overlayers on the fiber surface and efficient adsorption of the negatively charged BSA molecules. The synthesized copolymers have a well-defined structure as revealed from GPC. A fiber optic based protein sensor functionalized with the copolymer materials was developed in order to test the sensing performance of the copolymers. The deposition of the polymeric materials was performed using direct side polymer and dip coating techniques. When using direct side polymer deposition of the $PMMA_{117}$-*b*-$PDMAEMA_{16}$ and $PMMA_{117}$-*b*-P($DMAEMA_{17}$-$VSTEMA_2$) polymer, the layers produced were thick (~7 μm), resulting in a high detection limit (BSA concentrations ranging from 0.25% to 1% w/v) and deformation of the film after excessive use. On the contrary, $PMMA_{117}$-*b*-$PDMAEMA_{16}$ polymer films obtained with the dip coating technique were very thin (~30 nm) leading to good and reversible response of the sensor, decreasing the detection limit by one order of magnitude (BSA concentration ranging from 0.025% to 0.1% w/v). ATR-FTIR analysis was also performed, confirming the efficient protein adsorption. The performance of the $PMMA_{117}$-*b*-P($DMAEMA_{17}$-$VSTEMA_2$) block polymer showed that an increase in the polymer hydrophobicity is probably needed in order to avoid the degradation of the film after repeated immersions in protein solutions. Biosensors with better performance can be developed in the future by integrating the polymers to novel flat fiber based photonic circuits [100].

Chapter 5

Electrospun Fluorescent Fibers for Sensing Applications

5.1 Introduction

Polymers are a promising and widely used material platform for functional devices development. The deployment of polymers with electronic or photonic platforms has allowed the development of a number of devices and sensors [30], [31]. In sensing technology functional polymers are usually employed as uniform layers or overlayers forming sensitive responsive layers to certain measurands. In photonics which is an emerging and highly promising field for devices development, this can be achieved either in fiber or integrated optical technology [32], [33] or even in free space optical architectures in the form of diffraction gratings [33]–[35]. The polymeric overlayer interacts by its surface with the measurand or even by volume by allowing adsorption of measurands within the polymer. Those characteristics impose certain restrictions to the effective volume interaction characterizing thus the response, the reaction time and the maximum measurement limit [39].

Electrospinning has been one of the most versatile methods employed for generating nano- and microfibers [101]–[103]. Its simplicity, scalability and high versatility in regards to the chemical composition, morphology and orientation of the produced fibers, renders this method very attractive in many scientific fields.

Fluorescence detection methods are distinguished by high sensitivity and resolution providing extremely low detection limits. Interactions between fluorescent moieties and analytes change the transmission of the fluorescence signal and can be easily detected by a simple and low cost optical system. The fibrous spatial network generated by electrospinning can provide large surface area to volume ratios of about 1-3 orders of magnitude more than that of corresponding continuous thin films [48], [49] for efficient interaction with the analytes to be detected.

During the last years the development of electrospun (nano)fibrous grids with embedded fluorescence moieties that were further evaluated in fluorescence sensing has attracted considerable attention. In these materials the fluorophores are either

covalently attached onto the polymer chains [49], [104]–[106] or are incorporated as dopants (either organic or inorganic) into the fibrous polymer matrix [107]–[111].

5.2 Cost-Effective Polymethacrylate-Based Electrospun Fluorescent Fibers toward Ammonia Sensing

5.2.1 Introduction

Anthracene is a well-known fluorescent molecule with highly interesting photophysical properties [112], [113]. The covalent anchoring of this fluorophore onto polymer chains has led to the development of fluorescent polymers that were further used in the construction of optoelectronic devices [114], [115], photoluminescent films [116], [117] and photoresists [118], [119]. Synthesis of well-defined methacrylate-based homopolymers and block copolymers containing anthracene side-chains functionalities have been previously prepared by Reversible Addition-Fragmentation chain Transfer (RAFT) controlled radical polymerization and they were evaluated as dual fluorescent chemosensors for amines and transmission metal ions in solution [120].

Although anthracene-doped nanofibers containing 9-chloromethylanthracene as a fluorescent dopant have been fabricated by means of the electrospinning method and evaluated in regards to their sensing performance towards an organic dye acting as a model quencher [107], in the present work a well-defined poly(9-anthrylmethyl methacrylate) homopolymer (PAnMMA) possessing anthracene side-chain moieties has been used in the fabrication of anthracene-containing electrospun fluorescent fibrous mats. The presented approach is considered to be highly advantageous compared to other fabrication routes reported so far, based on (a) its simplicity in regards to the synthesis of well-defined anthracene-containing homopolymers involving conventional RAFT polymerization methodologies, thus avoiding complicated and time-consuming polymer syntheses and/or post-modification steps; (b) the avoidance of the fluorophore leakage from the fibrous mat which may lead to inferior sensing properties, owned to covalent bonding of the fluorophore onto the polymer chain in contrast to the case where small fluorescent molecules are introduced within the polymer fibers as dopants; (c) the lack of interaction of the anthracene fluorophore with polymeric materials and its capability of forming complex compounds with ammonia molecules leading to effective fluorescent quenching; (d) the blending of the anthracene-containing homopolymer with PMMA that serves towards the “dilution” of the fluorophores thus avoiding self-quenching phenomena (e) the significant reduction of the material’s production costs since PMMA that is used in excess (97 wt% in respect to the total polymer mass) is a commercially available polymer of low cost and (f) the considerable decrease in the amount of the macromolecular fluorescent dopant introduced within the PMMA electrospun fibers compared to the amount of the

previously reported 9-chloromethylanthracene (9-CMA) dopant [107] employed in cellulose acetate fibers(i.e. 3 wt% *vs* 10 wt% corresponding to the PAnMMA and the 9-CMA fluorophores respectively), demonstrating the enhanced fluorescence efficiency of the PAnMMA polymeric dopant and consequently its high potential in the fabrication of high performance optical (fluorescence) sensors.

The evaluation of the developed materials was performed in this work toward the specific case of ammonia detection, demonstrating high fluorescent-based sensing efficiency. Due to their large surface area these 3D fibrous systems do not exhibit fast quenching mechanisms while providing fast response in ammonia presence and detection to concentrations up to 10000 ppm.

5.2.2 Ammonia Sensing

In order to detect ammonia vapors, a petri dish containing liquid ammonia solution of 25% w/v was placed on a peltier device inside a sealed testing chamber of 4.3L volume. The sample was excited by a UV LED at 385 nm using an appropriate FT600UMT excitation optical fiber purchased from Thorlabs with low attenuation at UV wavelengths. The emitted fluorescence was filtered by a Thorlabs FEL0400 longpass filter with 400 nm cut-off wavelength, that blocks the excitation wavelength and it was finally collected by a second optical fiber and analyzed by a Thorlabs CCS200 spectrometer. A schematic representation of the setup is shown in Figure 5-1. During the measurements the peltier device was switched on, ensuring continuous and rapid evaporation of the ammonia solution. The measurements were taken in two-minutes sampling ratio intervals.

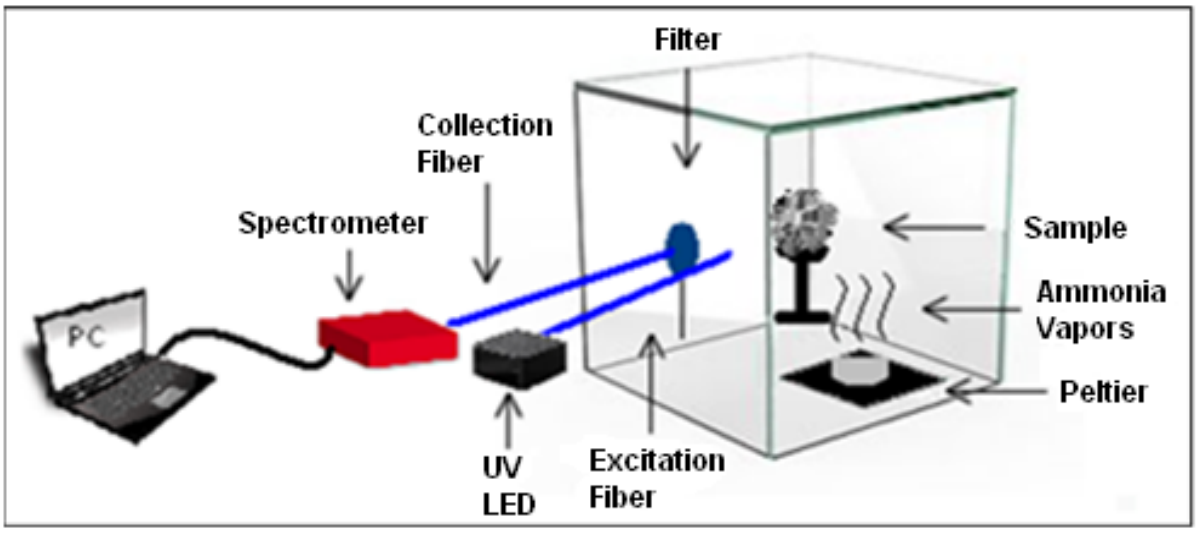

Figure 5-1. Schematic representation of the ammonia detection setup.

5.2.3 Results and Discussion

Polymeric fluorescent fibrous mats based on the commercially available PMMA and the in-house synthesized fluorescent PAnMMA were fabricated by means of the electrospinning technique. Figure 5-2 provides the chemical structures of the PMMA and PAnMMA homopolymers used in the present study. In Figure 5-3 representative photographs of the fabricated fluorescent fibers when exposed to UV irradiation are presented (Group of Dr. T. Krasia-Christoforou, Department of Mechanical and Manufacturing Engineering University of Cyprus).

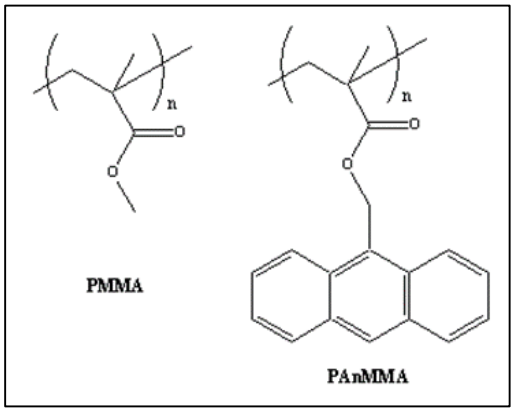

Figure 5-2. Chemical structures of the PMMA and PAnMMA homopolymers used for the fabrication of the electrospun fluorescent PAnMMA/PMMA blended fibers.

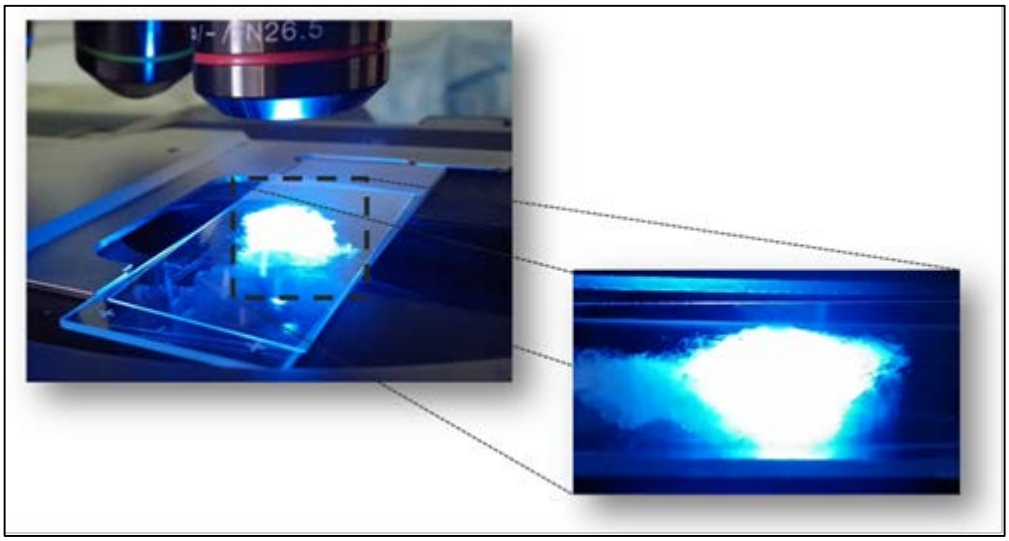

Figure 5-3. Photographs of the fibers when these are exposed to UV irradiation.

The morphological characteristics of the fluorescent fibers were determined by SEM. Figure 5-4 (a) provides characteristic SEM images of the as-prepared PMMA/PAnMMA fibrous mats (Group of Dr. T. Krasia-Christoforou, Department of Mechanical and Manufacturing Engineering University of Cyprus). As seen in the images, the fibers are continuous, without beads whereas they exhibit a non-cylindrical, tape-like

morphology. The average fiber diameters were determined from the SEM images by using the Digimizer Image Analysis software and they were found to be 6.59 ± 1.42 μm.

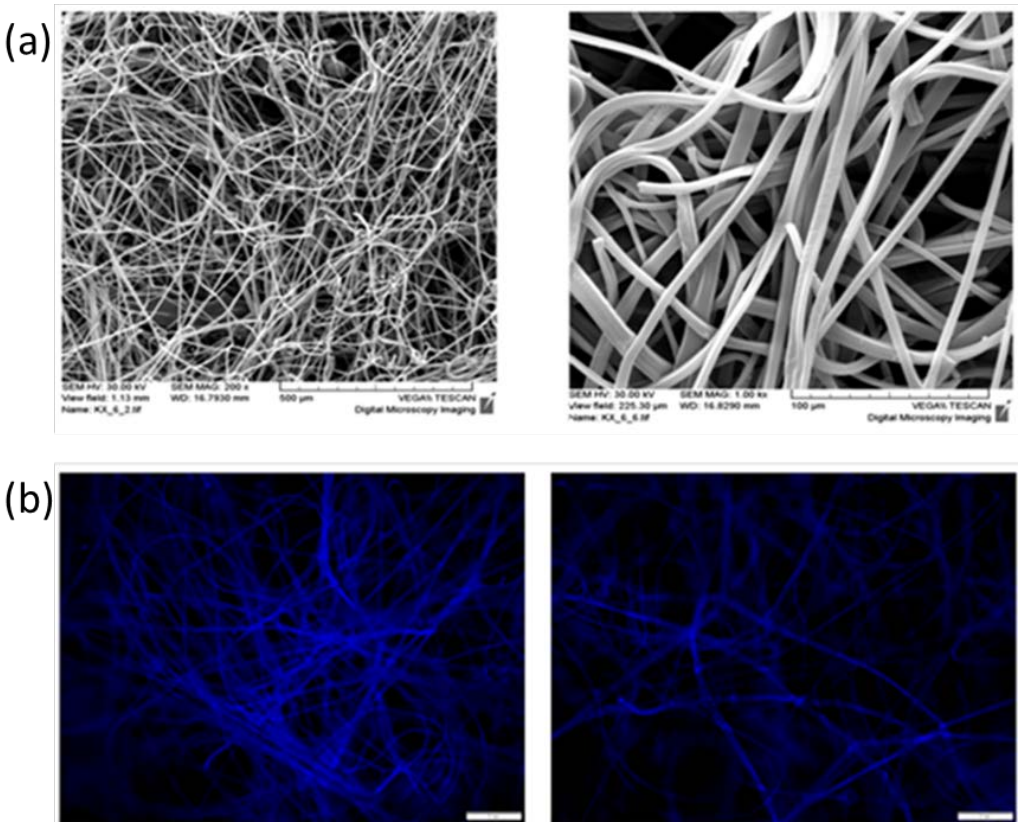

Figure 5-4. Scanning electron microscopy (a) and fluorescence microscopy images of the PMMA/PAnMMA blended fibers.

Fluorescence microscopy was also employed for visualizing the anthracene-containing fluorescent electrospun fibers and verifying their fluorescence efficacy. In Figure 5-4 (b) characteristic fluorescence microscopy images are provided. As seen from the images, the fibers behave as efficient blue light emitters thus verifying their high fluorescence efficacy even in the presence of very low fluorophore content (3 wt% of PAnMMA in respect to the total polymer mass) (Group of Dr. T. Krasia-Christoforou, Department of Mechanical and Manufacturing Engineering University of Cyprus).

Ammonia sensing can be achieved by measuring the fluorescence intensity reduction which results from the fluorescence quenching mechanism due to the creation of complex compounds between anthracene and ammonia molecules [121]. The peltier device was switched on during the measurements ensuring continuous and rapid evaporation of the ammonia solution. In Figure 5-5 the calculated evaporation rate of 25 % w/v ammonia solution is provided. The concentration of ammonia inside the chamber was calculated taking into account the evaporation rate and concentration of the solution, as well as the volume, pressure and temperature of the chamber.

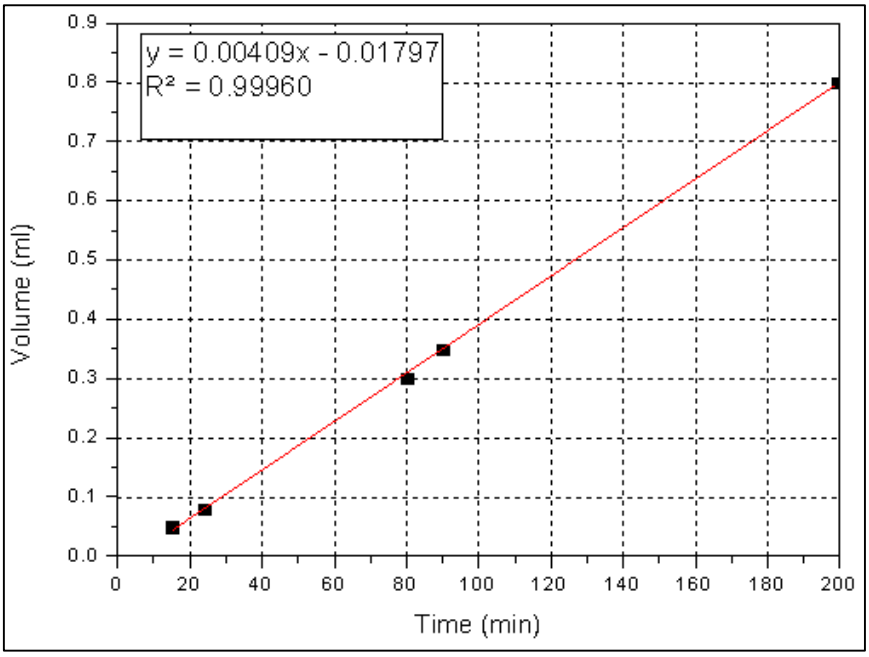

Figure 5-5. Evaporated ammonia's volume versus evaporation time exhibiting a linear relation.

Figure 5-6 (a) shows the fluorescence spectrum of the fibrous mats taken for different ammonia concentrations. Only two out of the three anthracene spectrum peaks, at λ = 419 nm and λ = 444 nm, are shown due to the use of the longpass filter. Figure 5-6 (b) shows a continuous reduction of the intensity of the two spectrum peaks, demonstrating a clear response to ammonia over an extended range of 10000 ppm. This can be attributed to their large volume, as these three-dimensional fibrous grids are able to detect high ammonia gas concentrations since they do not suffer from fast quenching mechanisms associated with the small interaction surfaces of films.

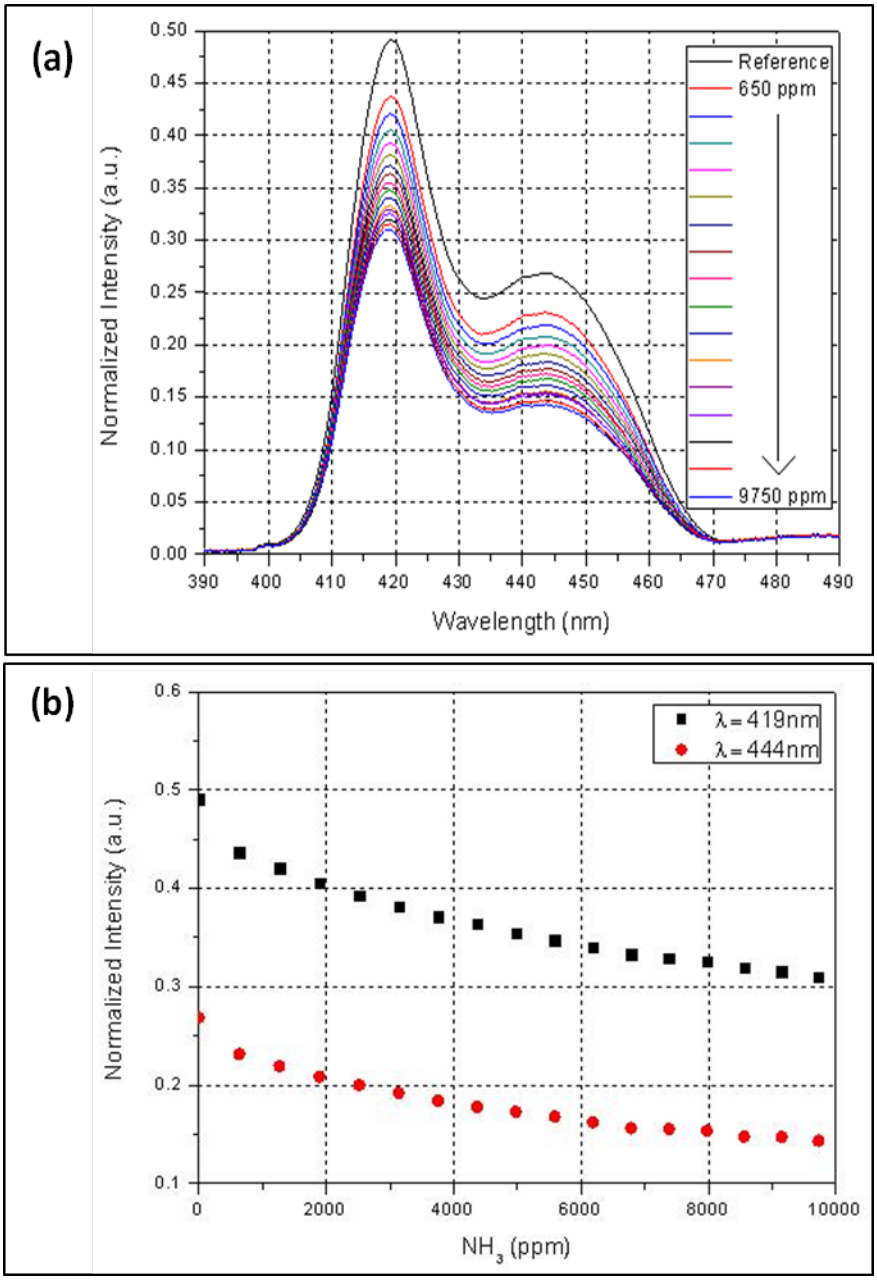

Figure 5-6. Fluorescence spectra of the fiber-containing anthracene moieties recorded in the presence of different concentrations of ammonia gas (a). Fluorescence spectra normalized intensity at the wavelength peaks of 444 nm (blue) and 419 nm (red) versus ammonia concentration (b).

Even though a clear reduction of the fluorescence intensity was observed, a quantitative evaluation of the lowest detection limit could not be performed at this study due to the simultaneous intensity reduction by the UV irradiation probably caused by the photodimerization of anthracene groups under UV exposure. However this expected effect of intensity reduction was monitored and quantified in order to validate the demonstrated results in the high ammonia concentration regime where it

exhibited negligible effect. Figure 5-7 shows the fluorescence intensity at 419 nm peak as a function of UV irradiation time, measured with a Horiba/Jobin Yvon, NanoLog fluorescence system. In the figure the presence of random noisy variations can be observed while the mean intensity is reduced only by a factor of ~2% after 30 minutes of continuous exposure. For the ammonia sensing evaluation a series of 17 measurements were taken and the UV LED was switched on for ~10 sec for each measurement. Thus the intensity reduction due to UV irradiation does not influence the ammonia detection experiments for which the total irradiation time was ~ 3 minutes.

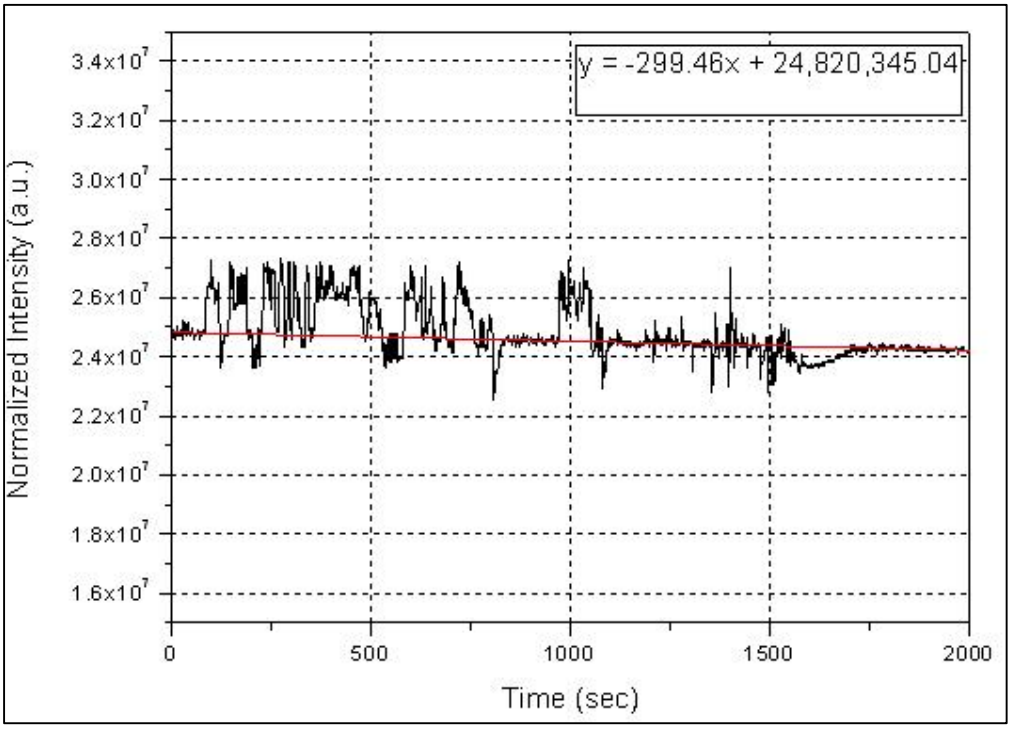

Figure 5-7. Normalized intensity at 419 nm peak versus time of UV exposure.

5.2.4 Conclusions

An electrospun fibrous nonwoven mat containing covalently-bound anthracene fluorescent moieties has been successfully employed for efficient ammonia gas sensing. Highly fluorescent PMMA/PAnMMA blended fibrous mats have been proved to be a very promising detection scheme for the potential development of inexpensive gas sensors. Such fibrous grids enable large volume interaction with gas analytes providing fast sensing in contrast to sensing mechanisms in uniform overlayers since they are free of penetration delays compared to polymeric films. Furthermore their characteristic of the large effective surface area to volume ratio allows the detection of

gas concentrations, up to 10000 ppm, thus rendering these systems highly promising in cost-effective industrial gas monitoring. In addition, the incorporation of an anthracene-containing polymer within the fibers in combination with its hydrophobic nature and thus the exclusion of leaching phenomena of the fluorescent dopant (which are commonly observed upon introducing low molecular weight fluorescent organic molecules instead) allows for their future exploitation in the fluorescence sensing of metal ions and biomolecules in aqueous media. Further exploitation of other fluorescent macromolecules in electrospun fibers are currently under investigation and may potentially lead to further sensitivity enhancement in different sensing applications in solution and in the gas phase.

5.3 Gas and pH Fluorescent Sensors based on Cellulose Acetate Electrospun Fibers decorated with Rhodamine Functionalised Core -Shell Ferrous Nanoparticles

5.3.1 Introduction

Functional inorganic nanoparticles (NPs) offer new possibilities in many research fields due to their unique size-dependent physicochemical properties, high surface areas and the possibility for surface tailoring [122], [123].

Organic – inorganic polymer-based nanocomposites in the form of thin films, 3D-networks and fibers, consisting of inorganic nanoparticles embedded within organic polymer matrices have become a major area of research and technological development owing to the remarkable properties and multifunctionalities deriving from their nanocomposite structure.

The nanoparticle-based systems that simultaneously contain more than one functional component are an active research field with the potential to have an impact on numerous technological applications [124]. Magnetic core-shell nanomaterials offer new opportunities not only in biomedical field but also in some specific technical applications such as support for heterogeneous catalysts, photocatalysts and integral part of biosensors [125]–[127]. However, the fluorescent core-shell magnetic nanoparticles have traditionally been studied most intensively in biomedicine because many research methods for investigating intracellular distribution, cellular uptake, and biological fate are based on confocal and fluorescent microscopy as well as fluorescence-activated cell sorter (FACS) using flow cytometry [128]–[133]. In this context, the silica-coated core shell magnetic nanoparticles have great potential for imaging since the fluorescent dye can be covalently anchored either onto the silica surface or doped into the matrix of the silica shell [129], [132], [134]. The possibility to integrate the fluorescent dye inside the silica matrix allows the silica surface to be

available for further dense and high quality functionalization. An important aspect for efficient labeling is the choice of proper fluorophore that do not lose the ability to fluoresce due to photon-induced chemical damage and covalent modification, i.e. photobleaching [135], [136]. However, only a few examples appear in the literature on the fabrication of nanocomposite electrospun fibers with embedded core-shell ferrous nanoparticles. In one such example, core-shell Fe/FeO nanoparticles have been incorporated within polyimide fibers aiming to produce fibrous nanocomposites exhibiting enhanced thermal stability and magnetic properties for potential use in high-temperature magnetic sensing and microwave absorption applications [137].

In another work reported by Z. Guo et al., magnetic polymer nanocomposite fibers reinforced with Fe/FeO core-shell NPs were prepared by electrospinning, followed by carbonization to obtain magnetic carbon nanocomposite fibers [138].

In the present study, ferrous core-shell nanoparticles consisting of a magnetic γ-Fe_2O_3 multi-nanoparticle core and an outer SiO_2 shell have been synthesized and further functionalized with Rhodamine B (RhB) fluorescent molecules. The latter were covalently bound in the matrix of the silica shell. The resulting RhB-functionalized ferrous nanoparticles were further incorporated within cellulose acetate (CA) electrospun fibers to yield fluorescent electrospun fibrous nanocomposites. Electrospun fibers with embedded fluorescence moieties designed for use in fluorescence sensing are considered to be advantageous compared to their film analogues, due to their larger surface-to-volume ratios. In previous reports on fluorescent-functionalized electrospun polymer fibers, the fluorophores were either covalently attached onto the polymer backbone [49], [104]–[106], [139] or they were incorporated as dopants within the fibers [107]–[111].

In one such example referring to the doping of polymer nanofibers with RhB, the fluorescent dye was added into a poly(ether sulfone) solution prepared in N,N-dimethylacetamide, and the mixture was electrospun to obtain fluorescent, RhB-doped nanofibers that were further evaluated as metal ion (Cu^{2+}) fluorescent sensors in aqueous media [140]. Furthermore, electrospun polymer fibers doped with Rhodamine B derivatives have been also successfully used as highly efficient turn-on fluorescent sensors for the detection of Hg^{2+} ions [141], [142].

In the present study, the use of RhB-functionalized core-shell ferrous nanoparticles as dopants in electrospun fibers is considered to be advantageous compared to other fabrication routes reported so far, since the leakage of the RhB fluorophore from the fibrous mat is prevented due to its covalent anchoring onto the nanoparticle surfaces. In contrast, small fluorescent molecules introduced within the polymer fibers as dopants are only held onto the polymer chains *via* weak van der Waals interactions, thus often resulting to their desorption from the polymer matrix and consequently the decrease in the fluorescence efficiency of the fibers. In addition, the covalent

anchoring of RhB molecules onto the nanoparticles' surfaces and the blending of the RhB-functionalized ferrous nanoparticles with the fibrous CA matrix, suppress self-quenching phenomena, whereas by covalently integrating RhB within the silica shell, fluorescence quenching is further prevented by avoiding direct contact with iron oxides.

Besides the above, the use of a renewable, naturally-abundant acetylated cellulose derivative as a polymer matrix exhibiting biocompatibility, biodegradability and environmental friendliness, as well as the magnetic character of the inorganic RhB-functionalized ferrous additives providing the possibility for magnetic separation by applying an external magnetic field are additional benefits of the fibrous nanocomposite fluorescent sensor described herein.

The evaluation of the dual sensing capability (i.e. ammonia gas and pH sensing) of the developed fibrous nanocomposites was carried out using a highly controllable measuring apparatus for the characterization of the fluorescence response under measurands presence. In the system an optical fiber-based setup for both the excitation of the fluorescent moieties and the collection of the emitted signal was used. Both electrospun and sprayed fibers with Fe_2O_3/SiO_2/RhB core-shell nanoparticles were evaluated for gas ammonia sensing showing a good response for very high concentrations, up to 12000 ppm. Furthermore in aquatic solutions with different pH values the electrospun fibers with embedded Fe_2O_3/SiO_2/RhB core-shell nanoparticles exhibited a fast and linear response in both alkaline and acidic environments.

5.3.2 Ammonia and pH Sensing Apparatus

In order to measure the sample's response to ammonia vapors and different pH values, the Fe_2O_3/SiO_2/RhB-functionalized CA electrospun fibers were placed in a cuvette holder having two perpendicular light paths specially designhned for free space applications. An all solid state 532 nm laser was used to excite the rhodamine moiety using a 400μm core multimode silica optical fiber. The emitted fluorescence was filtered by a Thorlabs FGL550 longpass filter with 550 nm cut-off wavelength, that blocks the excitation wavelength and it was finally collected by a 600μm core multimode optical fiber and analyzed by a Thorlabs CCS200 spectrometer. Both SMA terminated optical fibers are connected with the cuvette with SMA fiber adapters having mounted collimators. A schematic representation of the setup is shown in Figure 5-8.

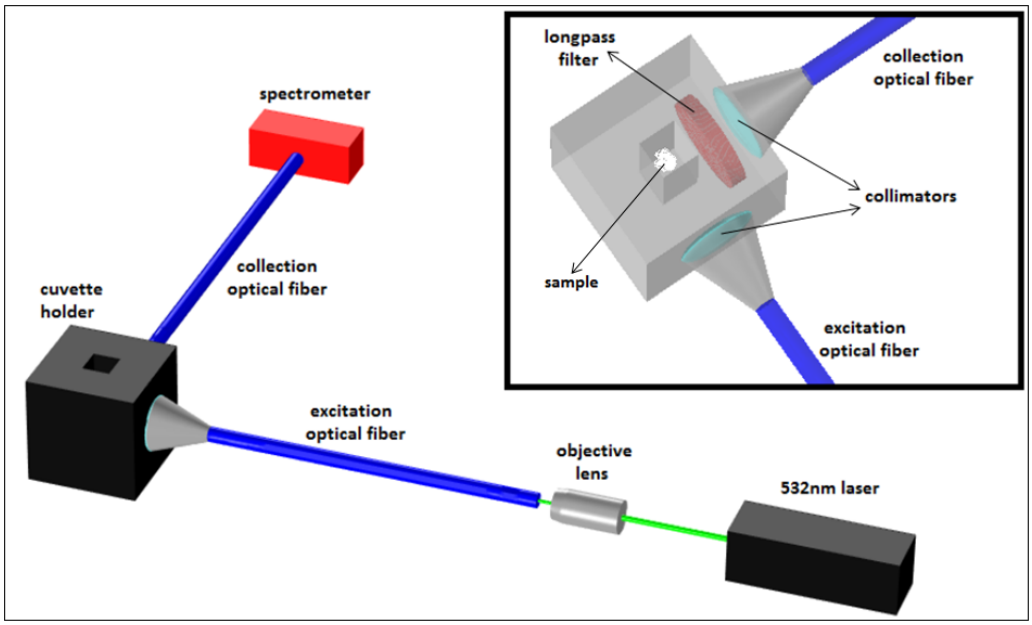

Figure 5-8. Schematic reperesentation of the experimental setup.

For the gas ammonia detection, the above described cuvette holder containing the sample was placed in a custom made sealed testing chamber of 4.3L volume. A peltier element was used for the evaporation of the 25% w/v ammonia solution drops as schematically depicted in Figure 5-9.

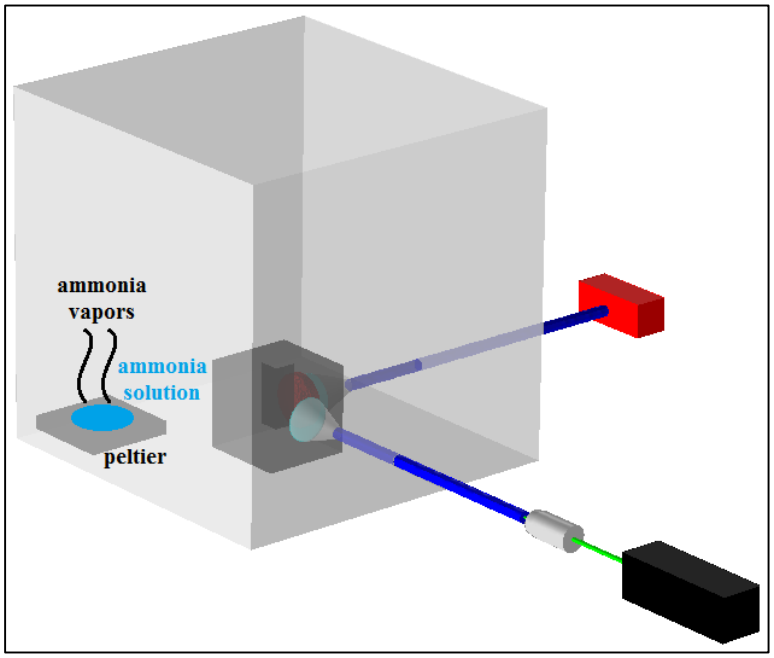

Figure 5-9. Schematic reperesentation of the ammonia sensing apparatus.

For the pH detection aquatic solutions of different pH values were used. HCl solutions with pH values ranging from 1-5 and NaOH solutions ranging from 8-13 were inserted in the cuvette where the sample was placed in order to evaluate the sample's response.

5.3.3 Results and Discussion

5.3.3.1 Rhodamine Functionalised Core -Shell Ferrous Nanoparticles

Fluorescent silica-coated nanoparticle clusters (core-shell nanoparticles) with approx. 20 nm thick silica shell were prepared as fluorescent and magnetic labels for the produced CA electrospun fibers (Dr. Slavko Kralj, Department for Materials Synthesis, Jožef Stefan Institute, Slovenia). The nanoparticle clusters were synthesized by the self-assembly of the superparamagnetic iron oxide (maghemite) nanoparticles. In the TEM images of the core-shell nanoparticles (Figure 5-10 (a) and (b)) (Dr. Slavko Kralj, Department for Materials Synthesis, Jožef Stefan Institute, Slovenia), the cluster core composed of closely packed individual maghemite nanoparticles can be clearly distinguished from the amorphous silica shell. The size of the core-shell nanoparticles was measured from the TEM images (> 100 particles counted) to be ~ 130 nm ± 30 nm. Core-shell nanoparticles showed superparamagnetic properties with a saturation magnetization Ms of ~ 37 Am^2 kg^{-1} (Figure 5-10 (c)) (Dr. Slavko Kralj, Department for Materials Synthesis, Jožef Stefan Institute, Slovenia). DLS measurements of the core-shell nanoparticles in an ethanol suspension (1.0 mg mL^{-1}) showed narrow hydrodynamic-size distribution with the average size at ~ 151 nm (SD = 2.8 %) (Dr. Slavko Kralj, Department for Materials Synthesis, Jožef Stefan Institute, Slovenia).

The core-shell particles form stable colloidal suspensions and this is verified by the fact that their DLS-determined size is in close agreement with the size determined by TEM.

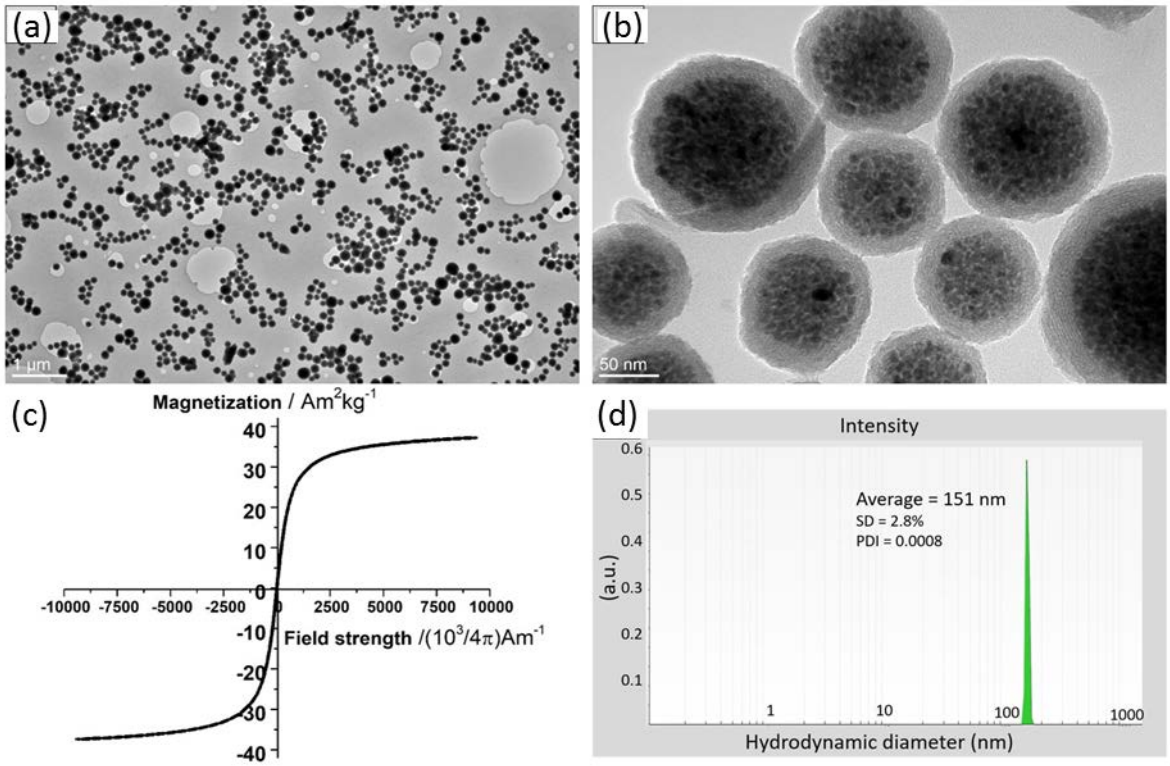

Figure 5-10. TEM images of core-shell nanoparticles at low (a) and high (b) magnification, room-temperature measurement of the magnetization as a function of magnetic field strength (c), and intensity-weighted distribution of the core-shell nanoparticles hydrodynamic diameters obtained from the DLS measurements in ethanol-based suspension at concentration 1 mg mL^{-1} (d).

In order to investigate the influence of the RhB-loading on the nanoparticles' fluorescence properties, RhB-labelled nanoparticle clusters having a lower RhB amount (i.e. only 3.11 µmol of RhB instead of 9.33 µmol per 450 mg of nanoparticle clusters – see in section 2.3) were synthesized (Dr. Slavko Kralj, Department for Materials Synthesis, Jožef Stefan Institute, Slovenia). As seen in Figure 5-11, the emission spectra of the fluorescent silica-coated nanoparticle clusters with high RhB loading showed higher relative intensity compared to the low RhB loading clusters, as expected. Most importantly, no shift in the maximum emission wavelength was observed upon altering the RhB loading.

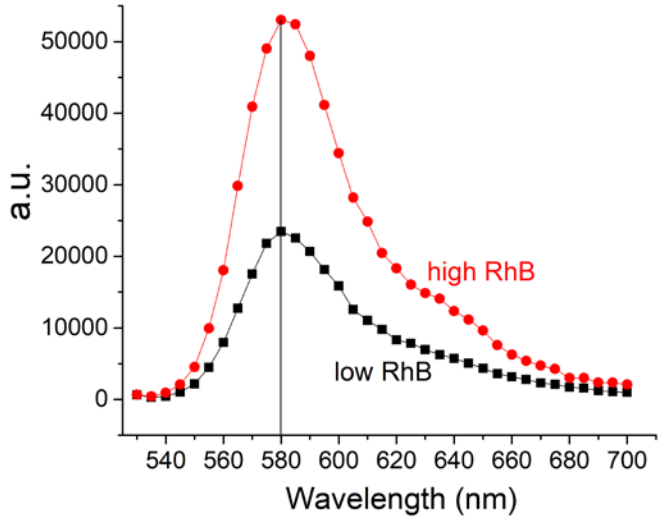

Figure 5-11. Emission spectra of fluorescent, silica-coated nanoparticle clusters (RhB-labelled silica) with high (9.33 µmol of RhB) and low (3.11 µmol of RhB) RhB loading.

In order to examine whether the optical response of RhB is influenced by the covalent linkage to the silica shell, the maximum emission wavelengths of the fluorescent silica-coated nanoparticle clusters (RhB-labelled silica) and of the RhB aqueous solution (free RhB) were compared (Dr. Slavko Kralj, Department for Materials Synthesis, Jožef Stefan Institute, Slovenia). As seen in Figure 5-12, the maximum emission wavelength of RhB aqueous solution was recorded at 585 nm, while after covalent anchoring with silica, the wavelength was shifted to 580 nm. It is noteworthy to mention at this point that when RhB was simply added to the TEOS (silica precursor) without the pre-formation of a covalent bond with the amino-silane molecule (APS), the product (silica-coated nanoparticle clusters) was not fluorescently labelled, and all RhB molecules were removed during vigorous washing.

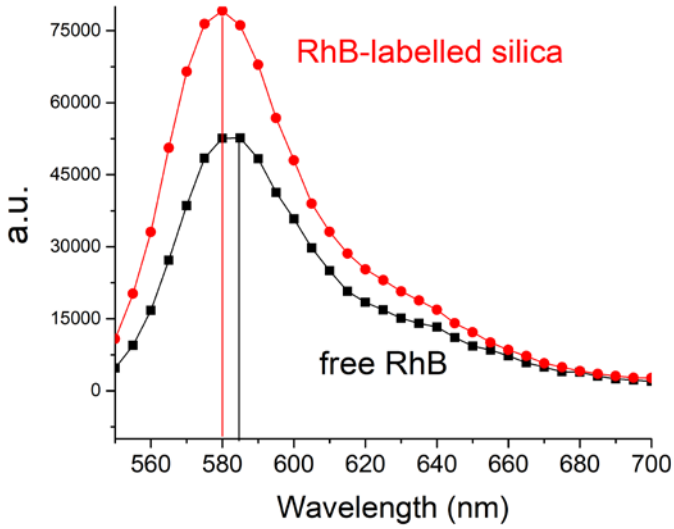

Figure 5-12. Emission spectra of the fluorescent silica-coated nanoparticle clusters (RhB-labelled silica) and of the aqueous solution containing free RhB molecules.

5.3.3.2 Fluorescent Electrospun Nanocomposite Fibers

Electrospinning was first employed in the fabrication of pristine CA fibers. A schematic of the electrospinning set-up used is provided in Figure 5-13 (Group of Dr. T. Krasia-Christoforou, Department of Mechanical and Manufacturing Engineering University of Cyprus).

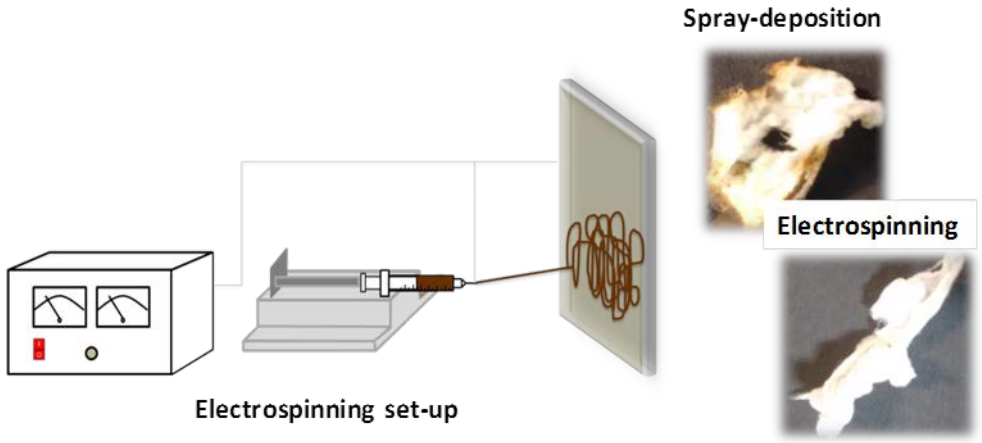

Figure 5-13. Left: Schematic of the electrospinning set-up used in the fabrication of electrospun CA fibers. Right: Indicative photographs of the γ-Fe2O3/SiO2/RhB functionalized CA fibers obtained via spray deposition of the RhB-functionalized nanoparticles onto the fibers' surfaces (up) and by mixing of the nanoparticle dispersion with the polymer solution, followed by electrospinning (down).

The morphological characteristics of the produced CA fibers were investigated by SEM (Group of Dr. T. Krasia-Christoforou, Department of Mechanical and Manufacturing Engineering University of Cyprus). As seen in the SEM images appearing in Figure 5-14, CA fibers had a belt-like (ribbon-like) morphology, a random orientation and they were characterized by a relatively broad diameter distribution within the micrometer size range. Ribbon-like morphologies in electrospun fibers based on cellulose and cellulose derivatives have been were previously reported [143]. Based on earlier reports the CA fiber morphology can be altered upon changing the solvent system and the polymer solution concentration. Under certain experimental conditions (i.e. specific solvent system, polymer solution concentration and optimum electrospinning parameters) the generation of cylindrical CA fibers is also feasible [144].

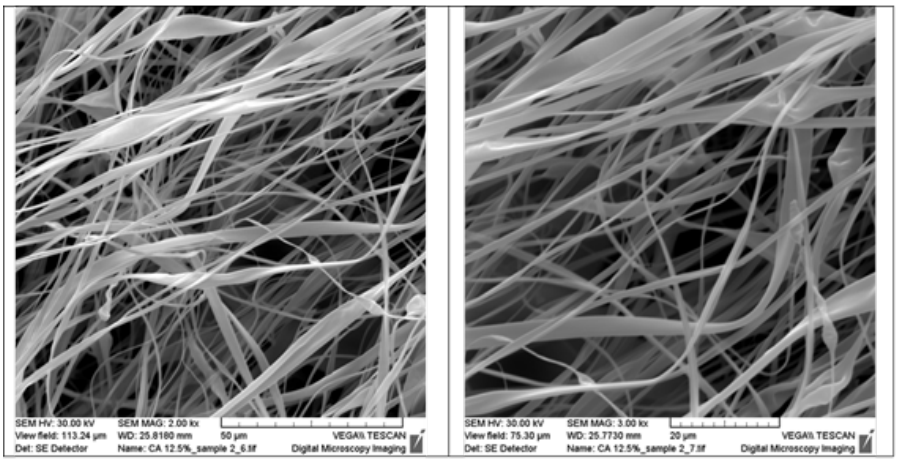

Figure 5-14. SEM images of CA electrospun fibers produced from acetone solutions (12.5 % w/v).

Although the effect of the fiber morphology on the magnetic and optical properties was not investigated in the present study, according to previous findings, the fiber diameters may have a significant influence on the materials' optical and magnetic properties. For example, N. Tomczak and co-workers fabricated electrospun poly(methyl methacrylate) (PMMA) fibers with embedded fluorescent additives (either fluorescent organic dyes or luminescent CdSe/ZnS core-shell quantum dots). Based on the single molecule approach, the fiber diameter may influence considerably the materials' optical properties. This was verified by the observation of a significant broadening of the fluorescence lifetime distribution when the fiber diameters were below the light wavelength (below 500 nm) [145]. Moreover, R. E. S. Bretas *et al.* demonstrated that the magnetic properties (i.e. saturation magnetization) of $BiFeO_3$ nanofibers produced by electrospinning increased with the decrease of the nanofibers' diameter and increase of nanofibers interconnectivity [146].

The fabrication of CA electrospun fibers decorated with RhB-functionalised core-shell ferrous nanoparticles was accomplished by following 2 different synthetic routes involving: (a) the deposition of the nanoparticles onto the fibers' surfaces *via* spraying and (b) the mixing of the nanoparticle dispersion prepared in ethanol with the CA acetone solution, followed by electrospinning (Group of Dr. T. Krasia-Christoforou, Department of Mechanical and Manufacturing Engineering University of Cyprus).

RhB was chosen to be covalently linked onto the nanoparticles' surfaces due to its high photostability compared to other fluorescent dyes introduced in previous studies as active moieties in optical sensing applications [147]. Actually, initial studies of our group involved the incorporation of FL-functionalized core-shell ferrous nanoparticles (Fe_2O_3/SiO_2/FL) within CA electrospun fibers by following the spraying deposition methodology. According to SEM analysis, the FL-functionalized nanoparticles were

homogenously deposited onto the fibers' surfaces and the resulting nanocomposite fibers exhibited strong fluorescence as demonstrated by fluorescence microscopy (Figure 5-15 (a) and (b) respectively) (Group of Dr. T. Krasia-Christoforou, Department of Mechanical and Manufacturing Engineering University of Cyprus). However, by repeating the fluorescence microscopy analysis 2 months after sample preparation, a significant decrease in the fibers' fluorescence efficiency was observed as shown in Figure 5-16, in line with previous literature references reporting the low photostability of FL [148].

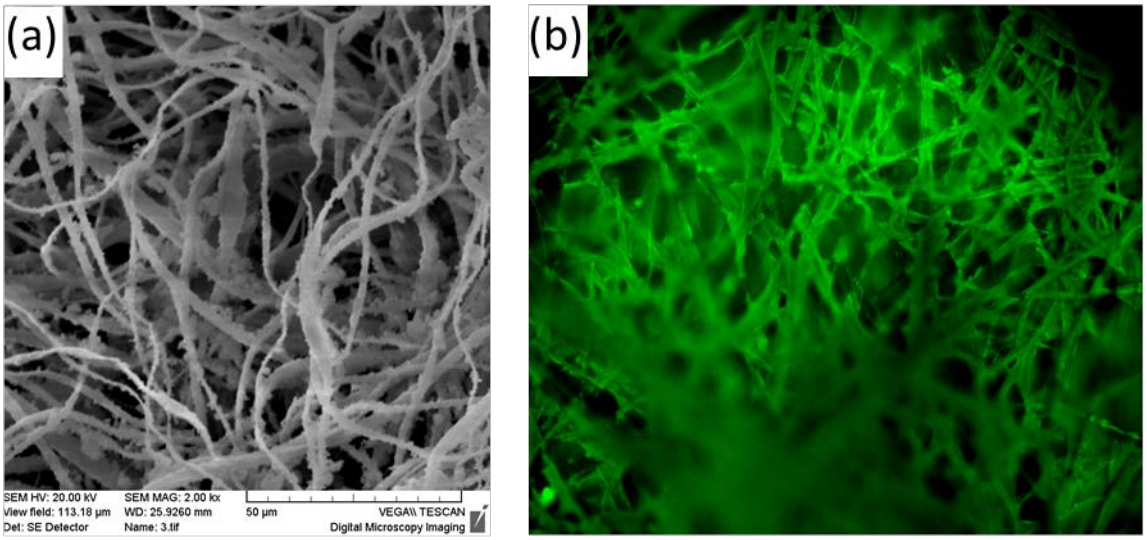

Figure 5-15. SEM image (a) and fluorescence microscopy image (b) of the FL-functionalized core-shell ferrous nanoparticles (FL/Fe_2O_3/SiO_2) deposited on the surfaces of electrospun CA via *spraying.*

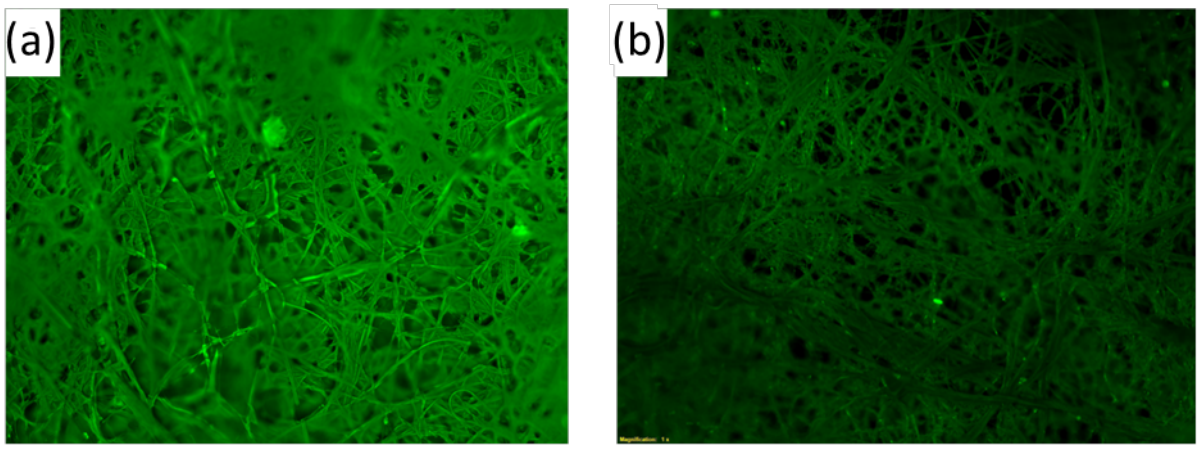

Figure 5-16. Fluorescence microscopy image of the freshly-prepared FL-functionalized CA fibers (a) and of the fibers after 2 months period (b).

The Fe_2O_3/SiO_2/RhB functionalized CA fibers were visualized by SEM and fluorescence microscopy (Group of Dr. T. Krasia-Christoforou, Department of Mechanical and Manufacturing Engineering University of Cyprus). As seen in Figure 5-17 ((a), (b)), both fabrication routes resulted to the anchoring of the nanoparticles onto the fibers' surfaces.

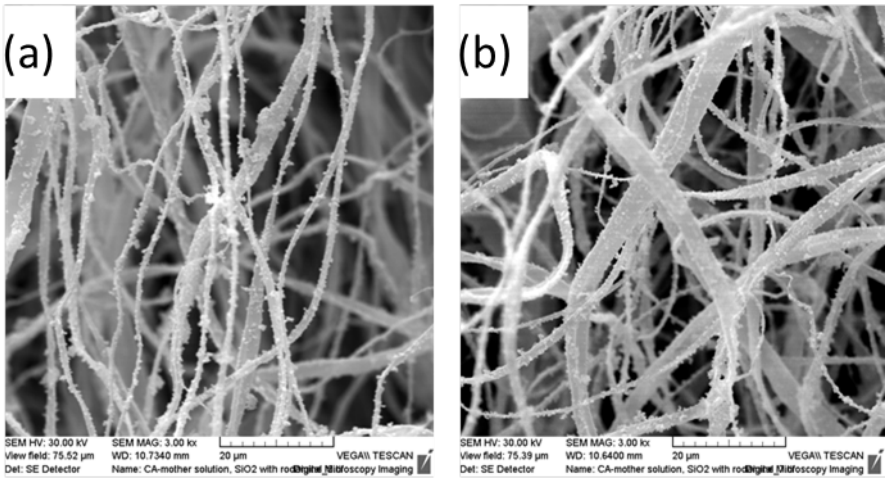

Figure 5-17. SEM images of the Fe_2O_3/SiO_2/RhB functionalized CA fibers obtained via *spray deposition of the RhB-functionalized nanoparticles onto the fibers' surfaces (a) and by mixing of the nanoparticle dispersion with the polymer solution, followed by electrospinning (b).*

Transmission Electron Microscopy (TEM) analyses confirmed the presence of γ-Fe_2O_3/SiO_2/RhB nanoparticles along the nanocomposite fibers (Figure 5-18) (Dr. Slavko Kralj, Department for Materials Synthesis, Jožef Stefan Institute, Slovenia). By comparing the TEM images of the electrospun fibrous nanocomposites ((a)-(d), Figure 5-18) with the fibrous analogues prepared via spray deposition ((e)-(h), Figure 5-18), the presence of the nanoparticles exclusively onto the fibers' surfaces can be observed in the second case, in contrary to the nanocomposite fibrous analogues prepared by electrospinning where the nanoparticles are mainly accumulated within the fibers.

In the case of the electrospun materials, the core-shell nanoparticle morphology could clearly be resolved in images at higher magnifications ((b) and (d), Figure 5-18). The core-shell ferrous nanoparticles are relatively homogeneously distributed along the fibers while on the nanoscale there is some segregation composed of up to dozen nanoparticles present in small aggregates. Due to high energy electron beam at the TEM accelerated at 200 kV, the core-shell nanoparticles deposited on or close to the surface of the fibers might immerse into partially melted CA fibers during TEM analysis and thus cannot be seen at the fiber surfaces. Additionally, since the TEM is a

transmission technique and the fibers diameter is large (up to few microns) the confirmation of the exact position of core-shell nanoparticles in/on the fibers is challenging to resolve and thus the TEM analysis is especially complementary to SEM analysis.

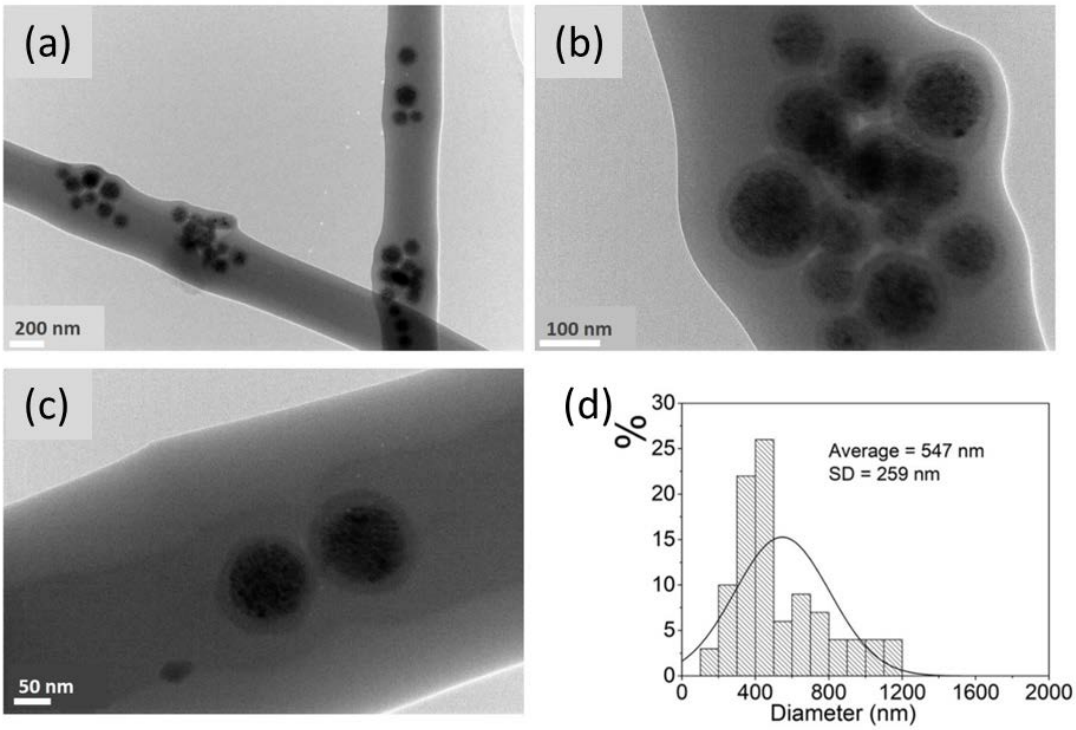

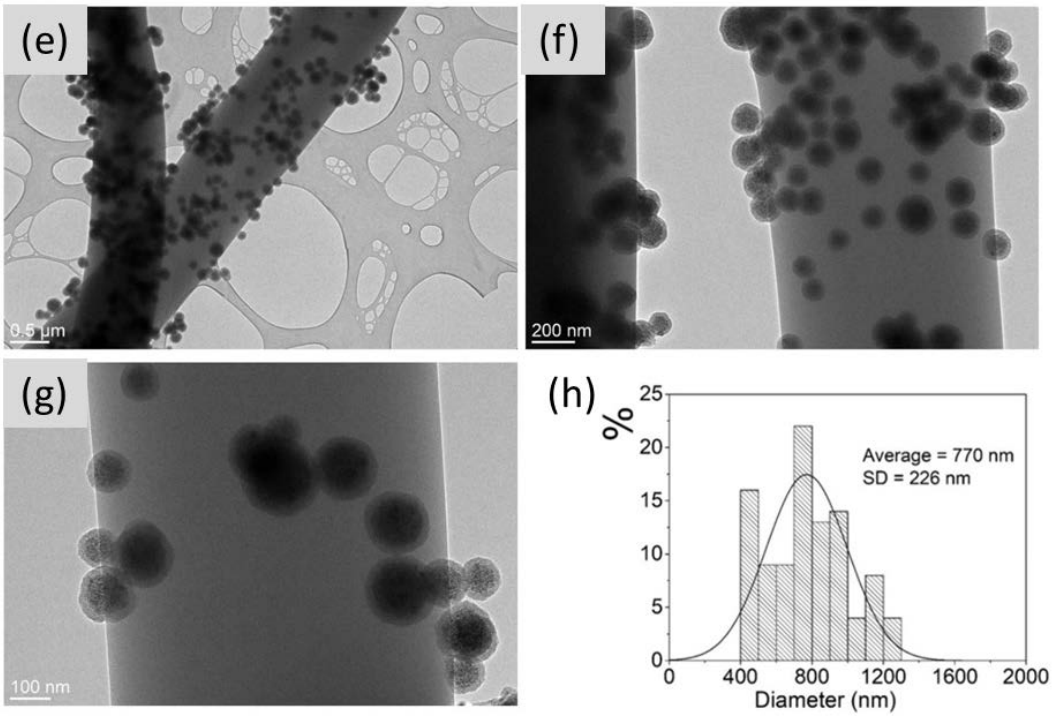

Figure 5-18. TEM images of γ-Fe2O3/SiO2/RhB functionalized CA fibers obtained by mixing of the nanoparticle dispersion with the polymer solution, followed by electrospinning (a-c) or via spray deposition of the RhB-functionalized nanoparticle solution on the surfaces of the as-prepared electrospun CA fibers (e-g). Fibers diameter distributions were determined by analysis of the TEM images corresponding to the electrospun magnetic fibers (d) and the sprayed magnetic fibers (h).

Fluorescence microscopy was used to verify the fluorescence properties of the multifunctional nanocomposite fibers. Figure 5-19 provides the fluorescence images of the produced materials (Group of Dr. T. Krasia-Christoforou, Department of Mechanical and Manufacturing Engineering University of Cyprus). By observing the fluorescence microscopy images, it can be seen that fluorescence is not homogeneous for the entire sample, particularly in the case of the fibers obtained by mixing the nanoparticle dispersion with the polymer solution, followed by electrospinning (Figure 5-19). According to the TEM data (provided in Figure 5-18), the nanocomposite fibers obtained by the spray deposition method have RhB-functionalized nanoparticles anchored all over their external surfaces. In contrary, in the case of the electrospun analogues, the nanoparticles that are embedded within the CA fibers form clusters and the presence of nanoparticle-free regions along the fibers can be clearly observed, resulting to a fluorescence “inhomogeneity” along the fibers.

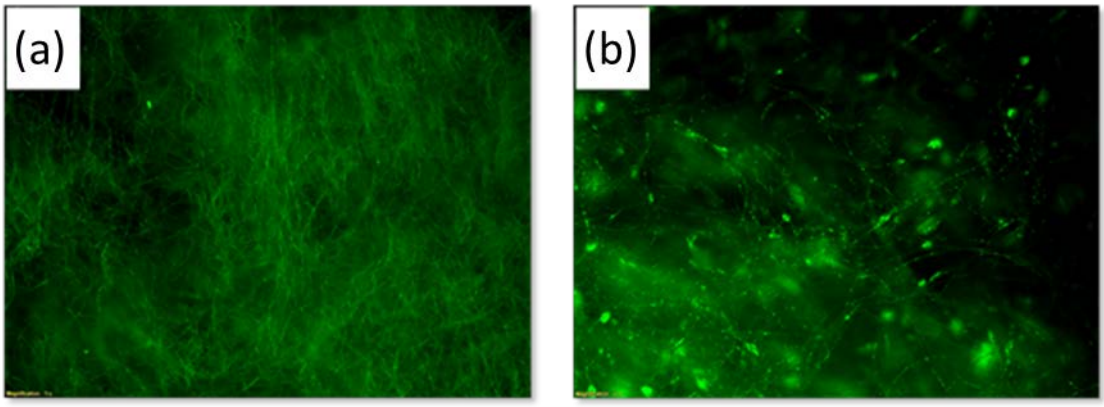

Figure 5-19. Fluorescence microscopy image of γ-Fe2O3/SiO2/RhB functionalized CA fibers obtained via spray deposition of the RhB-functionalized nanoparticles onto the fibers' surfaces (a) and by mixing of the nanoparticle dispersion with the polymer solution, followed by electrospinning (b).

The fluorescence efficiency of the RhB-functionalized ferrous nanoparticles anchored onto the CA fiber surfaces was investigated by photoluminescence spectroscopy at 520 nm excitation wavelength (Figure 5-20) (Group of Dr. T. Krasia-Christoforou, Department of Mechanical and Manufacturing Engineering University of Cyprus). The emission wavelength was recorded at 574 nm, in agreement with previous reports recording the emission wavelength of RhB within 574-577 nm [149]–[151].

Additional UV/Vis measurement spectra were not possible to be derived, as the materials were non-transparent and non-reflective, restricting thus their characterization in both transmission and reflective mode in UV/Vis spectrophotometer systems.

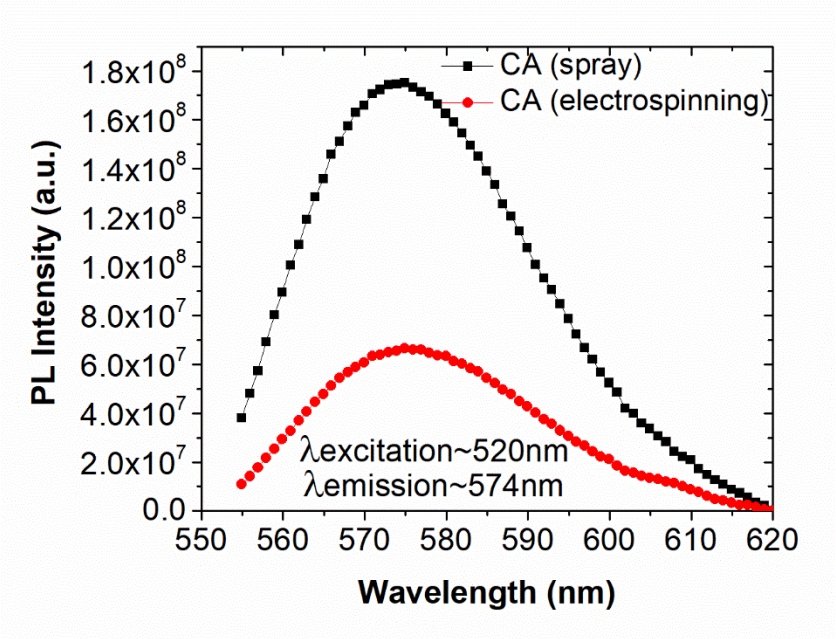

Figure 5-20. Photoluminescence spectra of the γ-Fe_2O_3/SiO_2/RhB functionalized CA fibers obtained via spray deposition of the RhB-functionalized nanoparticles onto the fibers' surfaces (a) and by mixing of the nanoparticle dispersion with the polymer solution, followed by electrospinning (b) (excitation wavelength: 520 nm).

The magnetic behaviour of the nanocomposite membranes was investigated by VSM at room temperature (Dr. Slavko Kralj, Department for Materials Synthesis, Jožef Stefan Institute, Slovenia). Figure 5-21 presents the magnetization *versus* applied magnetic field strength plots for the 2 types of the γ-Fe_2O_3/SiO_2/RhB functionalized CA nanocomposite fibers. As seen in the plots, both systems exhibited superparamagnetic behavior at ambient temperature [152], demonstrated by the symmetrical sigmoidal shape of the magnetization curves and the absence of a hysteresis loop. The fibers obtained *via* spray deposition had a higher saturation magnetization value (Ms ~ 0.82 Am^2 kg^{-1}) compared to the fibers obtained by mixing of the nanoparticle dispersion with the polymer solution, followed by electrospinning (Ms ~ 0.20 Am^2 kg^{-1}). Moreover, based on VSM magnetic measurements, the amounts of the γ-Fe_2O_3/SiO_2/RhB in the functionalized CA nanocomposite fibers were estimated to be ~ 2.2 wt. % and ~ 0.5 wt. % for the fibers obtained *via* spray deposition and the ones obtained by mixing of the nanoparticle dispersion with the polymer solution followed by electrospinning, respectively. These differences justify the differences observed in the photoluminescence spectra corresponding to the 2 cases (Figure 5-20).

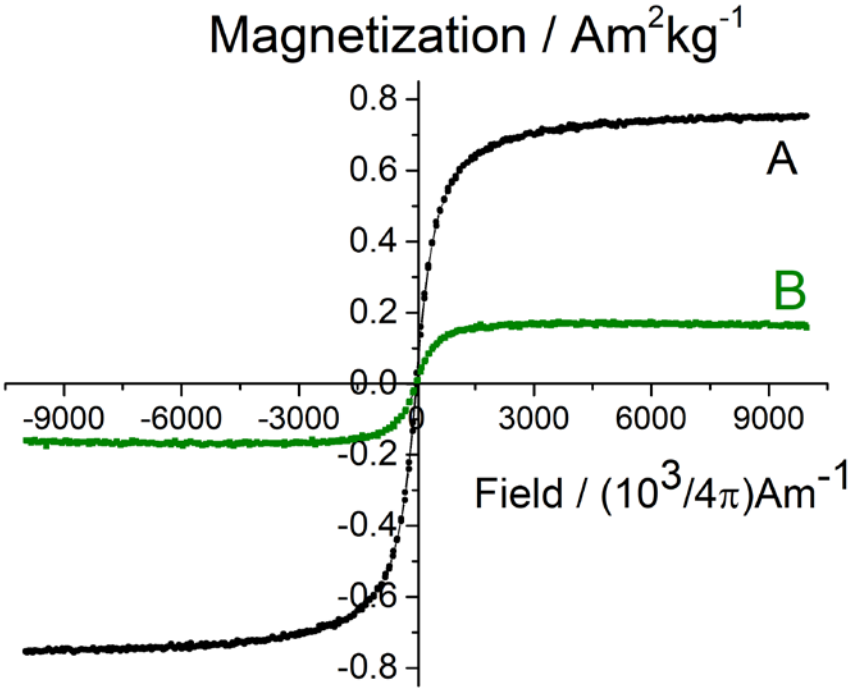

Figure 5-21. A room-temperature measurement of the magnetization as a function of magnetic field strength of the γ-Fe_2O_3/SiO_2/RhB functionalized CA fibers obtained via *spray deposition of the RhB-functionalized nanoparticles onto the fibers' surfaces (a) and by mixing of the nanoparticle dispersion with the polymer solution, followed by electrospinning (b).*

5.3.3.3 Gas (ammonia) and pH sensing

Both electrospun and spray-decorated γ-Fe_2O_3/SiO_2/RhB nanocomposite fibers were evaluated for different gas ammonia concentrations and pH values. The emission spectrum of the sample was stable upon continuous illumination, showing no self-quenching mechanisms observed with other fluorescent moieties such as anthracene [139]. For the measurements, the integration time of the spectrometer was set to 10s. The averaging method, rolling average over the last 3 acquisitions, was used. The sample was exposed for 30 s for each data point, showing fast response to the measurands. As each individual measurement corresponds to 30s, this can be an estimate of the time response which is comparable to other electrospun-based ammonia sensors [153], [154] where the response times range between 50 s – 350 s, as well as fluorescence-based sensors [155]. However, lower response times, in the ms scale, can be achieved by using porous hydrophilic sensing films with thickness at the nanoscale [156]. The time response can be also compared with ammonia sensors of different photonic technologies. In one such case, ammonia detection time response based on optical diffraction gratings comprised of $NiCl_2$ or $CuCl_2$ sol-gel composites incorporated at TMOS or TEOS matrices ranged between 150 and 270 s depending on the specific materials [33]. In another characteristic case on fiber optic sensors fabricated by thin film overlayers of diblock copolymers on the surface of polymer

optical fibers, similar response characteristics of ~300 s were exhibited for ammonia sensing [39]. In that sense, the response of the materials presented herein can be considered as fast. In order to assure the reliability of measurements for each recorded value, the sample was illuminated for 10 more minutes before changing NH_3 concentration or pH, showing no further change. This stability demonstrates that at continuous excitation, the properties of the material at constant ammonia concentration were not deteriorated, and also that the response is attributed reliably to the specific measuring conditions.

When exposed to NH_3 vapors, RhB undergoes structural changes resulting to the generation of a non-fluorescent lactone [157] (Figure 5-22). The latter explains the reduction observed in the fluorescence intensity upon exposure of the nanocomposite RhB-functionalized fibrous mats in NH_3 (Figure 5-23 (a) and Figure 5-24 (a)).

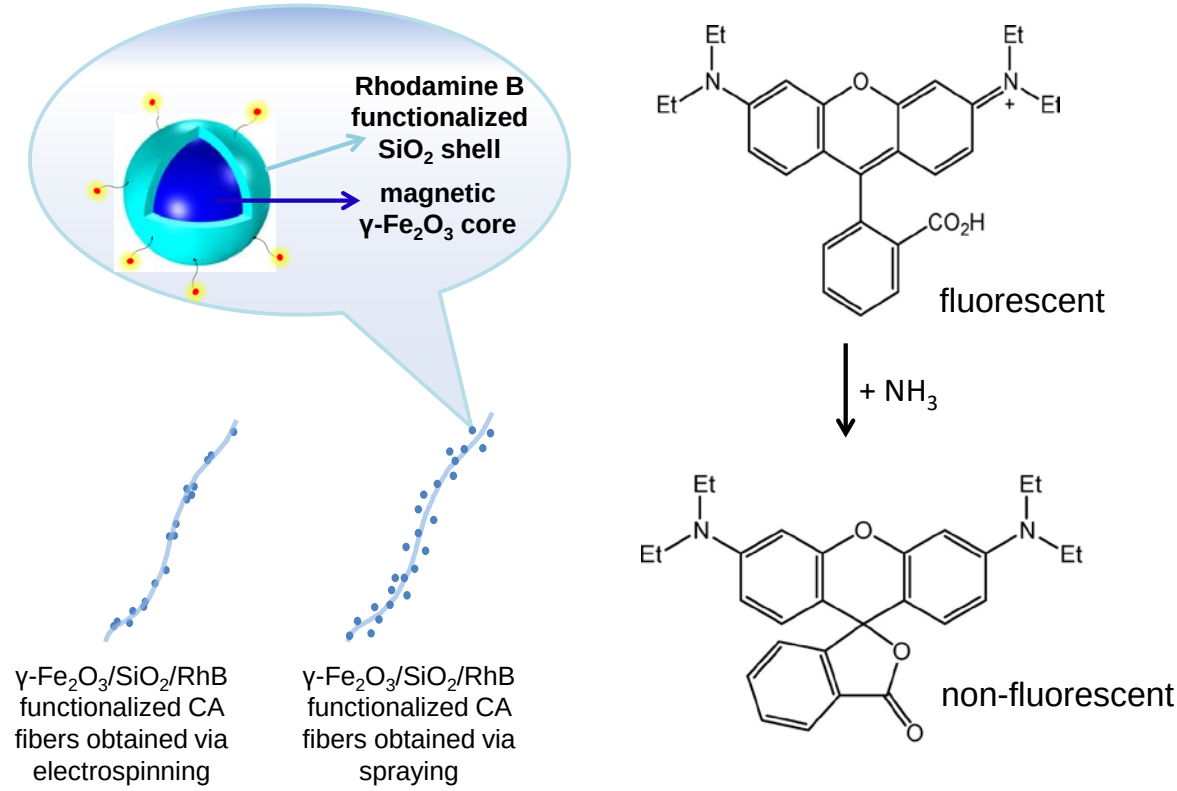

Figure 5-22. Sensing (fluorescence quenching) mechanism of RhB molecules undergoing structural changes when exposed to NH_3 vapours, resulting to the generation of the non-fluorescent lactone form.

Figure 5-23 (a) shows the fluorescence spectrum of the electrospun fibers with γ-Fe_2O_3/SiO_2/RhB core-shell nanoparticles taken for different ammonia concentrations.

A reference intensity value (I_{ref}) was taken before inserting the ammonia vapors. The fibers' response is defined as:

$$Response\ (\%) = \frac{I_{sig}-I_{ref}}{I_{ref}} \times 100 \quad (5\text{-}1)$$

where I_{sig} is the intensity measured for an ammonia concentration. Figure 5-23 (b) shows the response corresponding to the 577 nm peak, demonstrating a clear ammonia sensing for concentrations up to 11000 ppm.

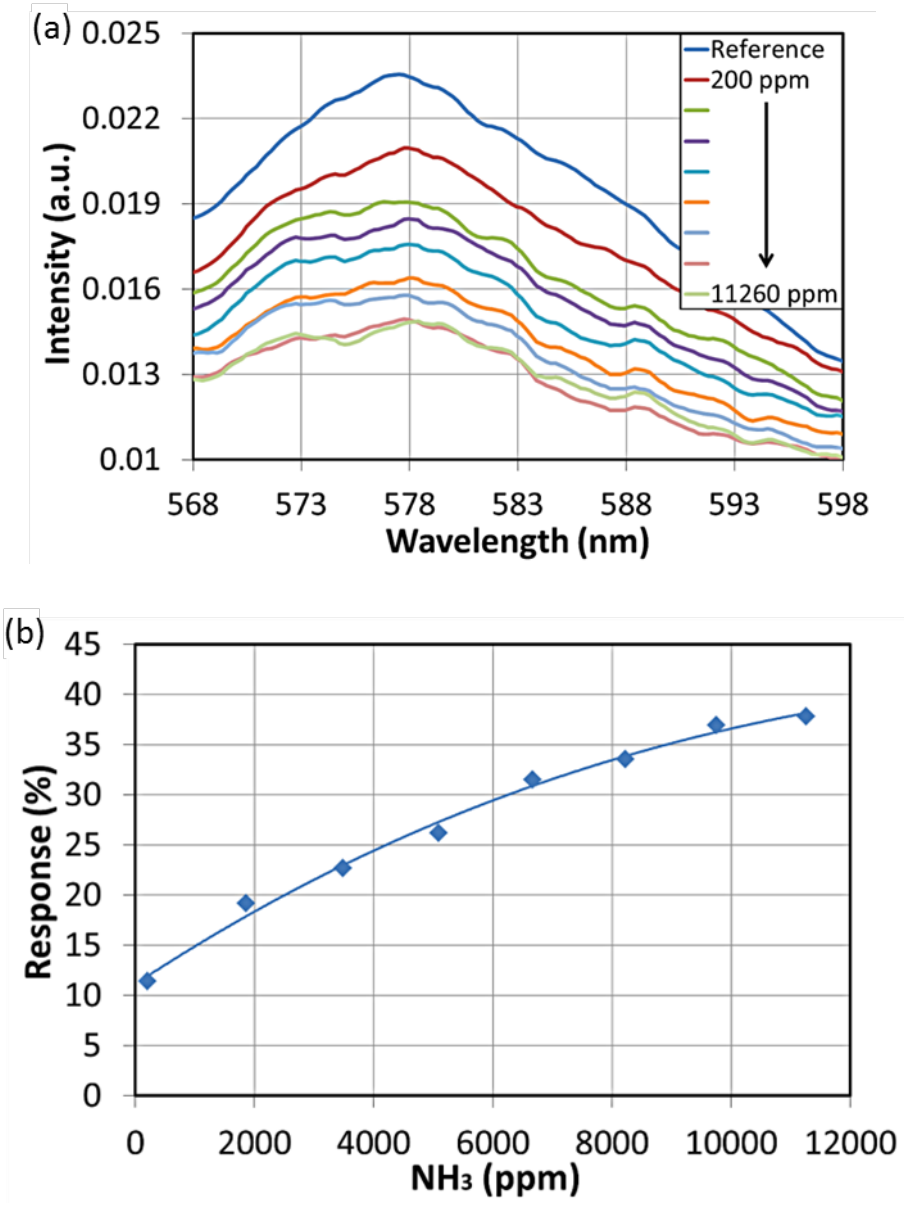

Figure 5-23. Fluorescence spectra of the electrospun fibers with γ-Fe_2O_3/SiO_2/RhB core-shell nanoparticles for different concentrations of ammonia gas (a). Response of the electrospun nanocomposite fibers at 577 nm for different ammonia concentrations (b).

The fibers decorated on their external surfaces with γ-Fe_2O_3/SiO_2/RhB core-shell nanoparticles *via* spraying, also show a clear response to the ammonia vapours as presented in Figure 5-24 for NH_3 concentrations up to ~13000 ppm. The detection of high NH_3 concentrations can be attributed to the large surface-to-volume ratio of the electrospun fibers. Previous studies have shown that due to the large surface-to-volume ratio, electrospun fiber sensors have enhanced sensitivity [157] as well as quenching efficiency [104] compared to thin films. The overall factor that enables the high concentration detection is actually the total number of sensing elements which are the γ-Fe_2O_3/SiO_2/RhB core-shell nanoparticles. Their total number in a specific volume of the material is determined by the three dimensional (3D) fibrous form and the concentration of the functionalised nanoparticles. However, the surface enhancement enabled by the fibrous morphology is the dominant factor which can be considered as a nonlinear scaling factor in a three dimensional space where the nanofibrous material is organised. The arrangement of nanoparticles in a linear shaped fiber, scales linearly but in this 3D fibrous form the total effect can be eventually characterised by a nonlinear scaling or enhancement factor.

The response of the sprayed samples is ~5% lower compared to the fibers electrospun with γ-Fe_2O_3/SiO_2/RhB nanoparticles. This could be attributed partially to the fact that in the former case the nanoparticles can easily detach from the fibers' surfaces before and during the measurements because they are only weakly attached to them.

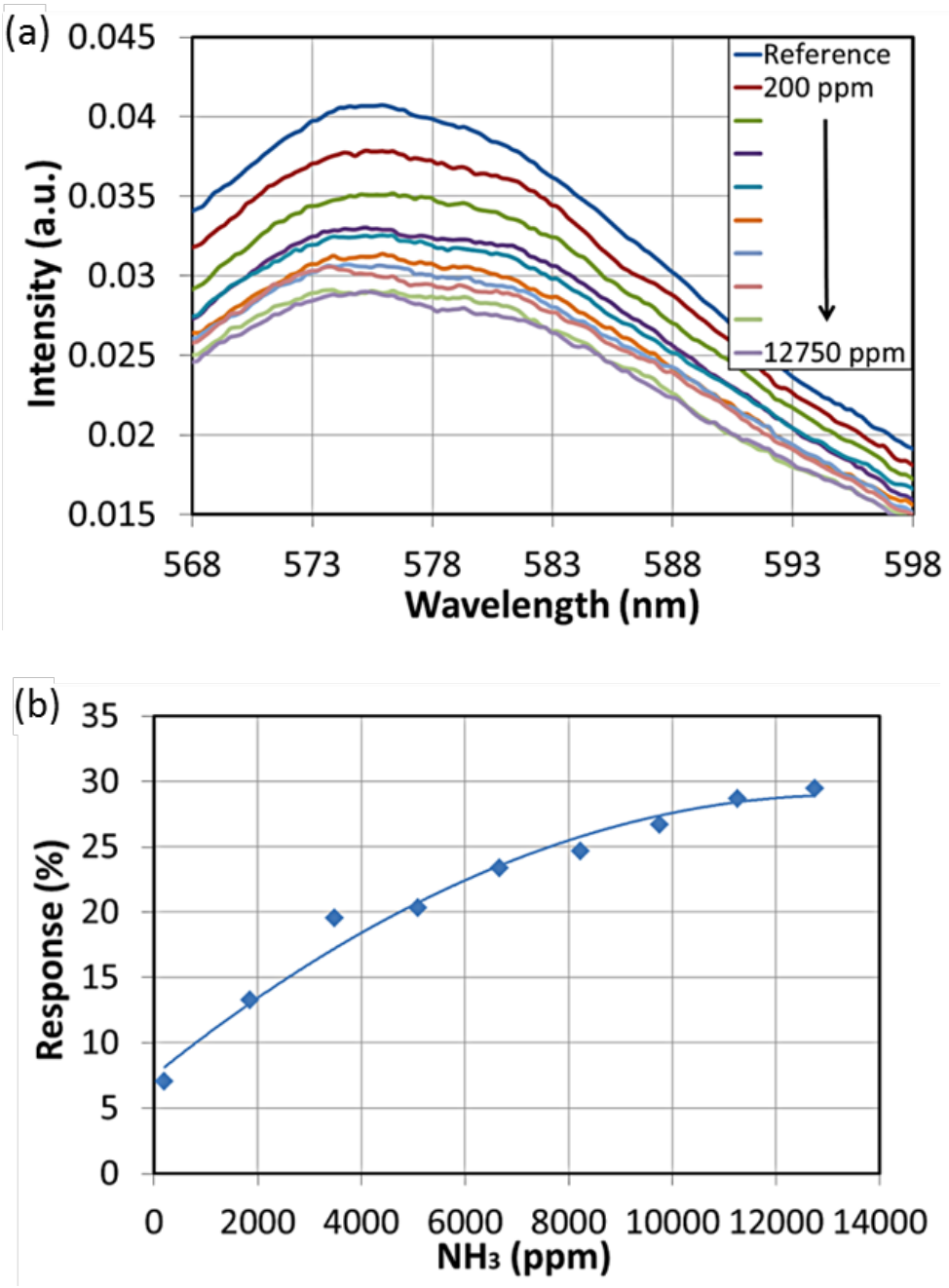

Figure 5-24. Fluorescence spectra of the fibers sprayed with γ-Fe_2O_3/SiO_2/RhB core-shell nanoparticles for different concentrations of ammonia gas (a). Response of the electrospun nanocomposite fibers at 577 nm for different ammonia concentrations (b).

The sample starts to quench above ~12000 ppm and the response curve reaches a plateau. Therefore the sensor can be used for NH_3 concentrations detection up to ~12000 ppm. Above this limit, the sensor cannot be reliably used as it becomes permanently "poisoned" and irreversible.

Furthermore, our experimental data show no consistent reversibility in ammonia sensing. This can be attributed to the high ammonia concentration, as heavy loading

(with ammonia) tends to destabilize the sensor, resulting in poor reversibility and smaller relative signal changes [158]. However, despite the non-reversible nature of the demonstrated behaviour, there are several sensing and detection applications where reversibility is not required as the purpose of the sensing element is to log/register successfully a specific high concentration of ammonia. Such cases are important in ammonia leakage monitoring especially at very high concentrations that can become toxic. Low cost sensing elements or materials can then be replaced after logging an ammonia leakage event.

Although the physical form of the electrospun fibrous materials is suitable for high concentration gas detection, it is not considered ideal for efficient collection of fluorescent light that could enable low level of detection. This is attributed to the fact that the material arrangement in the measuring cell could be vulnerable to external factors like vibrations, air flow etc., resulting to possible displacements that may alter the excitation and collection light angle. Therefore, for the optimization of the sensing performance, the development of a more robust customised miniaturised measuring apparatus is required in future studies.

The γ-Fe_2O_3/SiO_2/RhB-functionalized CA fibers were also evaluated as pH sensors in aqueous solutions with different pH values. Both electrospun and sprayed γ-Fe_2O_3/SiO_2/RhB-functionalized CA fibers were tested but only the nanocomposite fibers obtained *via* electrospinning exhibited a consistent response/behaviour in aquatic environments. On the contrary, detachment of the γ-Fe_2O_3/SiO_2/RhB core-shell nanoparticles decorating only the surface of the sprayed CA fibers was observed, when the latter were immersed in aquatic solutions, thus indicating the limited robustness of this system compared to the electrospun analogue. These results may be attributed to the weak nanoparticle/polymer matrix interactions arising from the surface functionalization *via* spray deposition. The latter is further supported by the TEM analysis provided in Figure 5-18, (e)-(h).

In Figure 5-25 (a), the fluorescent intensity of the electrospun nanocomposite fibers immersed in acidic aqueous solutions with different pH values, ranging from 5 to 1, is presented. The fibers were firstly immersed in a pH 5 solution and subsequently in solutions with lower pH values. As the pH decreases, the fluorescent intensity clearly increases.

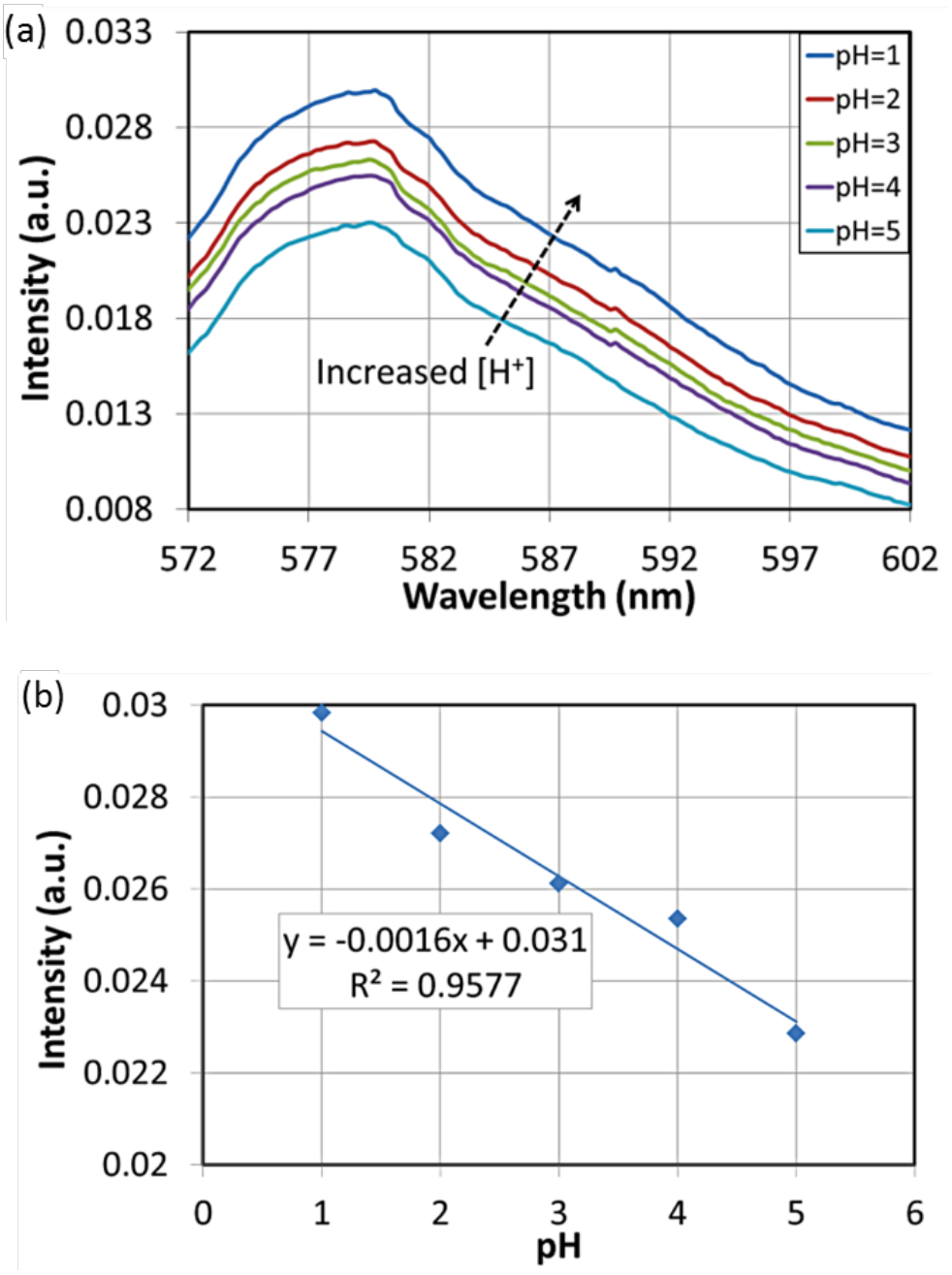

Figure 5-25. Fluorescence spectra of the fibers electrospun with γ-Fe_2O_3/SiO_2/RhB core-shell nanoparticles for acidic aqueous solutions with different pH values (a). Fluorescence intensity at 580 nm versus pH (b).

The electrospun nanocomposite fibers were also tested as fluorescent sensors in alkaline aqueous solutions with different pH values ranging from 8 to 13. The fibers were firstly immersed in a pH 8 solution and subsequently in solutions with higher pH values. As the pH increases the fluorescent intensity decreases (Figure 5-26 (a)). The intensity at the 580 nm peak is linearly depended on the pH value with R-square values of 0.9577 and 0.8817 for the acid and alkaline environments, respectively (Figure 5-25

(b) and Figure 5-26 (b)). The values of the slopes for the acid and alkaline environments are -0.00158 and -0.00165, respectively, with corresponding standard deviations of 0.0001917 and 0.0003028. The fact that the standard errors are less than 20% of the slope values, strongly indicates that the correlation is linear.

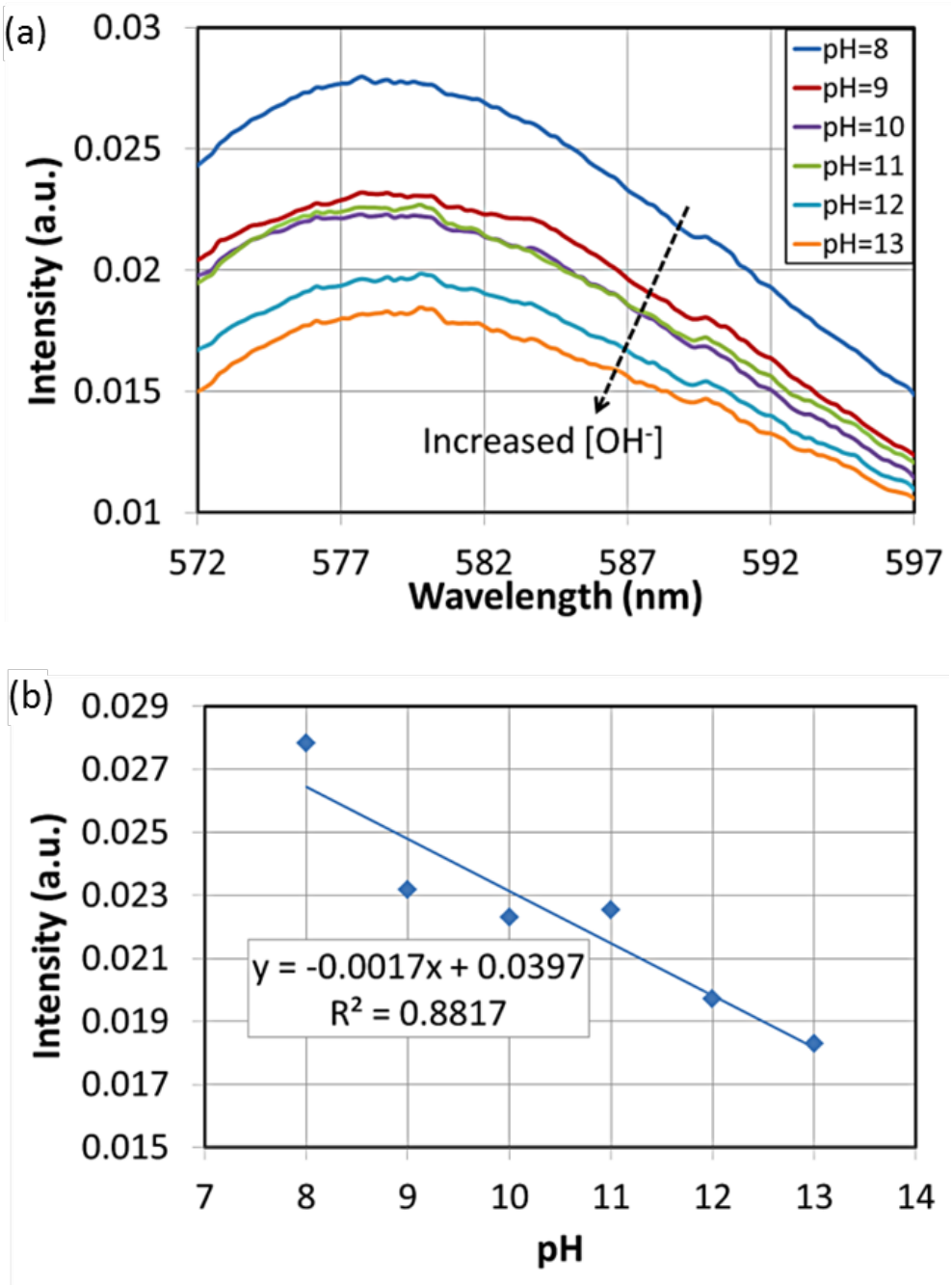

Figure 5-26. Fluorescence spectra of the fibers electrospun with γ-Fe_2O_3/SiO_2/RhB core-shell nanoparticles for basic aqueous solutions with different pH values (a). Fluorescence intensity at 580 nm versus pH (b).

The samples were also evaluated towards pH sensing reversibility, by alternating solutions with pH values of 2 and 7. The sample exhibited reversible on/off switchable fluorescence emission as presented in Figure 5-27 in accordance to the literature [159], [160]. It is noteworthy to emphasize that the γ-Fe_2O_3/SiO_2/RhB–functionalized electrospun nanocomposite fibers characterised 6 months after production towards pH sensing, exhibited a measurable response for a relatively long range of pH between 2 and 7, together with a consistent reversibility, demonstrating their stability and long term functionality.

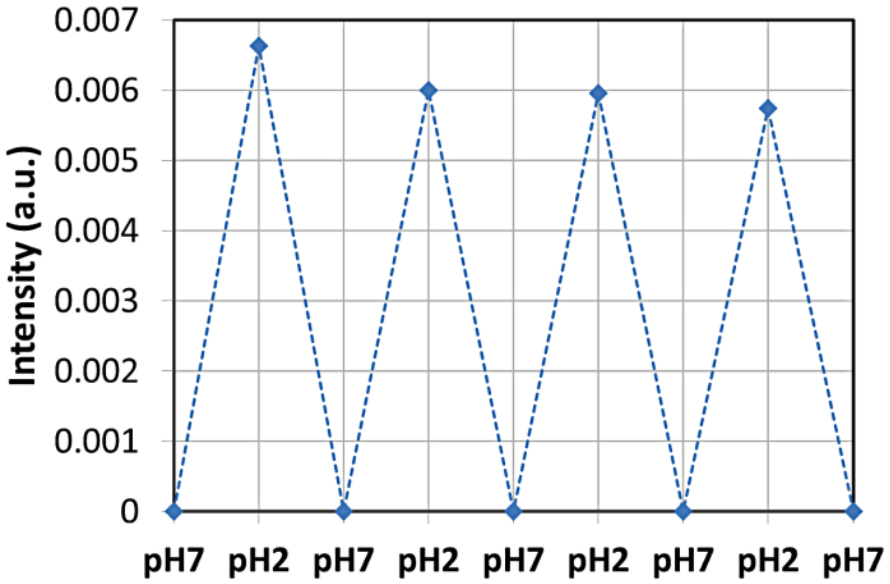

Figure 5-27. Reversibility of the pH-dependent on-off-on fluorescence intensity profile of electrospun fibers functionalized with γ-Fe_2O_3/SiO_2/RhB nanoparticles.

To summarize, concerning the ammonia sensing performance, the nanocomposite fibers obtained *via* spray deposition of the Fe_2O_3/SiO_2/RhB core-shell nanoparticles showed a ~5% lower response compared to the electrospun fibrous analogues, partially due to nanoparticle concentration differences in the two samples deriving from the fact that in the case of spray deposition, the NPs are detached from the fibers' surfaces before and during the measurements because they are only weakly attached to them.

Further to the above logical assumption, it should be underlined that the absolute value of NPs concentration and the resulted photoluminescence (Figure 5-20) of the two different fiber types should not be related to their sensing responses, as the response is calculated to a reference intensity value connected to the absolute initial photoluminescence. The absolute photoluminescence is reflected only by the absolute

values of the measured intensity in the graphs appearing in Figure 5-23 (a) and Figure 5-24 (a), which are indeed higher for the case of the sprayed fibers (Figure 5-24 (a)). Therefore, it is noteworthy to stress out that the response in the case of the electrospun fibers (Figure 5-23) is higher despite the fact that the sensing functionalized NPs are embedded in the hosting fibers and are not directly exposed to ammonia gas as in the case of the NPs deposited onto the fibers' surface *via* spraying. The adsorption mechanism of ammonia in the electrospun fibers is proved equivalent (or even more efficient), compared to the direct sensing on the sprayed NPs, because of the minimal dimension of fibers. Furthermore, the stability of the NPs is retained, since these are protected within the fibers and they are not directly exposed to external degradation factors.

Based on the above, the nanocomposite fibers obtained *via* spray deposition were found to be less robust as pH fluorescent sensors owned to the fact that the γ-Fe_2O_3/SiO_2/RhB core-shell nanoparticles decorating only the surface of the sprayed CA fibers were detached upon immersion of the fibers in aquatic solutions indicating their ineffectiveness in applications involving aquatic environments.

5.3.4 Conclusions

In this work, the fabrication of cellulose acetate electrospun fibers dopped with RhB-functionalized core-shell ferrous nanoparticles is reported. Due to the covalent anchoring of the RhB fluorophore onto the nanoparticle surfaces its leakage from the fibrous mat is prevented. Two different fabrication protocols of the CA fibers dopped with the Fe_2O_3/SiO_2/RhB core-shell nanoparticles were followed. In the first synthetic approach, the nanoparticles were sprayed on top of the fibrous mat while in the second a nanoparticle suspension in the CA polymer solution prepared in acetone was electrospun producing the fibers. The electrospun nanocomposite fibers were evaluated for both gas ammonia and pH sensing. Due to the large surface-to-volume ratio of the functionalized fibrous mats, high ammonia concentrations up to 12000 ppm were detected. Furthermore the fibers showed fast and linear response to aquatic solutions of different pH values.

Chapter 6

Summary and Future Work

6.1 Summary

Nanostructures of dimensions around the operating wavelength of light can support optical resonances enhancing the incident light by orders of magnitude and concentrating it in the nanoscale. Their integration to optical fiber tips with thin metallic claddings, forming plasmonic slot nanoresonators (PSNRs), provides ease of light coupling from the fiber's core modes to the slot and a robust platform which can find many applications in nano-optics and sensing. In Chapter 2 guiding and modal properties of metal-coated optical fiber tips with embedded PSNRs were investigated through FEM simulations towards the identification of their optimization parameters. It was found that the placement of a PSNR at the cut-off radius of a metal-coated fiber tip, where the group velocity tends to zero, leads to considerable intensity enhancement of the field confined beyond the diffraction limit. Maximum intensity enhancement of optimally placed PSNRs at different radii shows a linear dependence between excitation wavelength and radius, making it feasible to engineer the proper radius for a specific wavelength for maximum enhancement.

Metal tips are emerging plasmonic structures that can offer high field intensity at the tip apex and high confinement on the nanoscale. However, the fabrication of smooth metal tips with well-defined geometrical characteristics, crucial for optimizing the performance of the plasmonic structure, is not trivial. Furthermore, pure metal tips are exposed to the environment and fragile, thus complicating their use in real applications. A platform based on hybrid composite glass metal microwires which can offer the required robustness for device development was proposed in Chapter 2. An optimized fabrication process of high-quality all-fiber plasmonic tips by tapering such hybrid metal core/dielectric cladding microfibers is proposed and demonstrated experimentally. The presence of the dielectric cladding offers continuous re-excitation of the plasmon modes due to repeated total internal reflection at the glass/air interface, which can dramatically reduce the high losses induced by the metal core. This enables direct light coupling from the distal end of fiber instead of side excitation of the tip, allowing thus their integration in the optical fiber and planar circuits. Plasmonic tips were successfully demonstrated in a highly controllable manner, and their performance was related to simulation results predicting high field

enhancement factors up to 10^5. In order to find the optimum conditions for tapering these multicomponent optical fibers the Plateau-Rayleigh instability in such hybrid fibers was theoretically investigated by inducing surface tension perturbations and compared to Tomotika instability theory. The continuous-core breakup time was calculated via FEM simulations for different temperatures and was found to be considerably higher to Tomotika's model while the final sphere diameter is a linear function of the initial core radius. Furthermore different sinusoidal perturbations parameters were considered showing significant impact in the characteristics of formed spherical features.

Novel amphiphilic block copolymers having both hydrophobic poly(methyl methacrylate) (PMMA) and hydrophilic poly[2-(dimethylamino)ethyl methacrylate] (PDMAEMA) blocks have been designed and synthesized for efficient protein detection in photonic-based sensing and was presented in Chapter 4. Both the cationic $PMMA_{117}$-b-$PDMAEMA_{16}$ and the cationic vinyl-sulfone functionalized $PMMA_{117}$-b-P($DMAEMA_{17}$-$VSTEMA_2$) block copolymers, where VSTEMA is 2-(2-(vinylsulfonyl)ethylthio)ethyl methacrylate, were synthesized from a water insoluble hydrophobic PMMA block, which facilitated the formation of stable overlayers on the silica optical fibers surface. The well-defined structure of the co-polymers was confirmed by gel permeation chromatography (GPC). The presence of the cationic PDMAEMA block and the vinyl-sulfone double bonds led to reversible electrostatic binding of negatively charged proteins like bovine serum albumin (BSA) and non-reversible chemical binding by thiol-ene reactions with cysteine in proteins, respectively. The sensing properties of these materials were assessed and confirmed by ATR-FTIR analysis and by the characterization of fabricated sensing heads on silica optical fibers functionalized with suitably deposited overlayers. The sensing assessment revealed the requirements for deposited overlayer characteristics towards proteins' detection sensitivity and selectivity enhancement.

The fabrication of cost-effective, polymer-based electrospun fluorescent fibrous grids and their evaluation as candidates for sensing is reported in Chapter 5.1, drawing useful results on their applicability and efficiency in gas sensing applications. A well-defined, methacrylic homopolymer functionalized with anthracene moieties as fluorescent elements has been blended with a commercially available poly(methyl methacrylate) for the production of fluorescent electrospun polymer fibers. The formation of 3D grids can provide large interaction area with gas analytes and thus overcome quenching limitations induced by polymeric films, for more efficient sensing. These materials have been evaluated for ammonia sensing based on the fluorescence quenching of the anthracene fluorophores in the presence of ammonia vapors, exhibiting fast response at concentration up to 10000 ppm. The covalent bonding of the anthracene fluorophore onto a hydrophobic polymethacrylate- based backbone enables the future exploitation of the presented materials in sensing applications involving metal ions and biomolecules in aqueous media.

In Chapter 5.2 ferrous core-shell nanoparticles consisting of a magnetic γ-Fe_2O_3 multi-nanoparticle core and an outer silica shell have been synthesized and covalently functionalized with Rhodamine B (RhB) fluorescent molecules (γ-Fe_2O_3/SiO_2/RhB NPs). The resulting γ-Fe_2O_3/SiO_2/RhB NPs were integrated with a renewable and naturally-abundant cellulose derivative (i.e. cellulose acetate, CA) that was processed in the form of electrospun fibers, to yield multifunctional fluorescent fibrous nanocomposites. The encapsulation of the nanoparticles within the fibers and the covalent anchoring of the RhB fluorophore onto the nanoparticle surfaces, prevented the fluorophore's leakage from the fibrous mat, enabling thus stable fluorescence-based operation of the developed materials. These materials were further evaluated as dual fluorescent sensors (i.e. ammonia gas and pH sensors), demonstrating consistent response for very high ammonia concentrations (up to 12000 ppm) and fast and linear response in both alkaline and acidic environments. The superparamagnetic nature of embedded nanoparticles provides means of electrospun fibers morphology control by magnetic field-assisted processes and additional means of electromagnetic-based manipulation making possible their use in a wide range of sensing applications.

6.2 Future Work

The need of high field confinement beyond the diffraction limit of light has led to a remarkable progress in the field of plasmonics over the last decades. Many different plasmonic structures that can confine and enhance the electromagnetic field by orders of magnitude by exploiting the coupling between light and conductive electrons have extensively been studied. Such structures have found applications in many research fields such as data storage, microscopy, SERS and sensing.

Metal coated optical fibers and fiber tapers with embedded PSNRs, studied in this thesis, suggest a robust platform for high field confinement. FEM simulations can be performed in order to further optimize the shape and dimensions of the PSNR which could result to increased intensity enhancement, even by orders of magnitude, due to resonances corresponding to the cut-off wavelength (~700 nm). By nano-patterning the PSNR creating shapes with sharp edges the field intensity can be further enhanced. The fabrication of the optimized gold coated fiber tips with the appropriately sized PSNRs can validate the theoretical results. Cascaded PSNRs or circular grating structures on the fiber surface could be also studied.

Metal core fiber tips, as the ones studied in Chapter 3, can also be fabricated with different metals. Silver and copper core metal tips could provide a more cost-effective solution for the development of robust hybrid plasmon tips which can offer ease of light coupling from the fiber's distal end. Computational fluid dynamic simulations can help for defining the optimum parameters for the fabrication of metal core microfibers with continuous cores, as

core discontinuities can affect their post-processing resulting in cladding collapse and fiber breakage. Microfluidic simulations will be also performed for different metal cores and for even smaller initial core diameters towards the development of optimized hybrid metal tips as well as the fabrication of in-fiber uniform sized spheres which can act as microresonators. Fabrication approaches could allow the controllable placement of embedded microspheres at close proximity to plasmonic tips in order to allow excitation of microresonators.

Additionally novel polymeric materials, as the ones studied in Chapter 4, can be integrated on fiber tip PSNRs or at the apex of the developed hybrid metal tips. As discussed in Chapter 4.4 the refractive index of the polymeric materials does not affect the light enhancement at the PSNR and hence their integration can form a highly sensitive sensing platform for the adsorption or immobilization of different biomolecules decreasing the detection limits up to single molecule detection. Different polymers can be developed and integrated depending on the target to be detected.

Successfully identified electrospun materials for gas sensing studied in Chapter 5, could be suitable as overlayers in optical fibers or plasmonic structures. Adaptation of electrospinning deposition process could allow the controllable deposition of such electrospun micro/nano fibers on the surface of optical fibers for sensors development.

Bibliography

[1] M. I. Stockman, "Nanoplasmonics: past, present, and glimpse into future," *Opt. Express*, vol. 19, no. 22, pp. 22029–22106, Oct. 2011, doi: 10.1364/OE.19.022029.

[2] H. Raether, *Surface Plasmons on Smooth and Rough Surfaces and on Gratings*. Berlin Heidelberg: Springer-Verlag, 1988.

[3] S. A. Maier, *Plasmonics: Fundamentals and Applications*. Springer US, 2007.

[4] J. Burke, G. Stegeman, and T. Tamir, "Surface-Polariton-Like Waves Guided by Thin, Lossy Metal-Films," *Phys. Rev. B*, vol. 33, no. 8, pp. 5186–5201, Apr. 1986, doi: 10.1103/PhysRevB.33.5186.

[5] M. Zervas, "Surface-Plasmon Polariton Waves Guided by Thin Metal-Films," *Opt. Lett.*, vol. 16, no. 10, pp. 720–722, May 1991, doi: 10.1364/OL.16.000720.

[6] S. Albader and M. Imtaar, "Azimuthally Uniform Surface-Plasma Modes in Thin Metallic Cylindrical-Shells," *IEEE J. Quantum Electron.*, vol. 28, no. 2, pp. 525–533, Feb. 1992, doi: 10.1109/3.123282.

[7] S. Albader and M. Imtaar, "Tm-Polarized Surface-Plasma Modes on Metal-Coated Dielectric Cylinders," *J. Lightwave Technol.*, vol. 10, no. 7, pp. 865–872, Jul. 1992, doi: 10.1109/50.144906.

[8] M. Zervas and I. Giles, "Optical-Fibre Surface-Plasmon-Wave Polarizers with Enhanced Performance," *Electron. Lett.*, vol. 25, no. 5, pp. 321–323, Mar. 1989, doi: 10.1049/el:19890223.

[9] A. K. Sheridan, P. Ngamukot, P. N. Bartlett, and J. S. Wilkinson, "Waveguide surface plasmon resonance sensing: Electrochemical desorption of alkane thiol monolayers," *Sens. Actuator B-Chem.*, vol. 117, no. 1, pp. 253–260, Sep. 2006, doi: 10.1016/j.snb.2005.11.047.

[10] J. N. Anker, W. P. Hall, O. Lyandres, N. C. Shah, J. Zhao, and R. P. Van Duyne, "Biosensing with plasmonic nanosensors," *Nat. Mater.*, vol. 7, no. 6, pp. 442–453, Jun. 2008, doi: 10.1038/nmat2162.

[11] M. Bauch, K. Toma, M. Toma, Q. Zhang, and J. Dostalek, "Plasmon-Enhanced Fluorescence Biosensors: a Review," *Plasmonics*, vol. 9, no. 4, pp. 781–799, Aug. 2014, doi: 10.1007/s11468-013-9660-5.

[12] E. Di Fabrizio *et al.*, "Roadmap on biosensing and photonics with advanced nano-optical methods," *J. Opt.*, vol. 18, no. 6, p. 063003, Jun. 2016, doi: 10.1088/2040-8978/18/6/063003.

[13] T. Vo-Dinh, H.-N. Wang, and J. Scaffidi, "Plasmonic nanoprobes for SERS biosensing and bioimaging," *J. Biophotonics*, vol. 3, no. 1–2, pp. 89–102, Jan. 2010, doi: 10.1002/jbio.200910015.

[14] Y. S. Huh, A. J. Chung, and D. Erickson, "Surface enhanced Raman spectroscopy and its application to molecular and cellular analysis," *Microfluid. Nanofluid.*, vol. 6, no. 3, pp. 285–297, Mar. 2009, doi: 10.1007/s10404-008-0392-3.

[15] W. A. Challener *et al.*, "Heat-assisted magnetic recording by a near-field transducer with efficient optical energy transfer," *Nat. Photonics*, vol. 3, no. 4, pp. 220–224, Apr. 2009, doi: 10.1038/NPHOTON.2009.26.

[16] C. L. Wong and M. Olivo, "Surface Plasmon Resonance Imaging Sensors: A Review," *Plasmonics*, vol. 9, no. 4, pp. 809–824, Aug. 2014, doi: 10.1007/s11468-013-9662-3.

[17] B. Lee, I.-M. Lee, S. Kim, D.-H. Oh, and L. Hesselink, "Review on subwavelength confinement of light with plasmonics," *J. Mod. Opt.*, vol. 57, no. 16, pp. 1479–1497, 2010, doi: 10.1080/09500340.2010.506985.

[18] M. Ding, M. N. Zervas, and G. Brambilla, “Transverse excitation of plasmonic slot nano-resonators embedded in metal-coated plasmonic microfiber tips,” *Appl. Phys. Lett.*, vol. 102, no. 14, p. 141110, Apr. 2013, doi: 10.1063/1.4801945.

[19] M. Ding, G. Brambilla, and M. N. Zervas, “Plasmonic Slot Nanoresonators Embedded in Metal-Coated Plasmonic Microfibers,” *J. Lightwave Technol.*, vol. 31, no. 18, pp. 3093–3103, Sep. 2013, doi: 10.1109/JLT.2013.2279196.

[20] M. I. Stockman, “Nanofocusing of optical energy in tapered plasmonic waveguides,” *Phys. Rev. Lett.*, vol. 93, no. 13, p. 137404, Sep. 2004, doi: 10.1103/PhysRevLett.93.137404.

[21] P. Uebel, S. T. Bauerschmidt, M. A. Schmidt, and P. S. J. Russell, “A gold-nanotip optical fiber for plasmon-enhanced near-field detection,” *Appl. Phys. Lett.*, vol. 103, no. 2, p. 021101, Jul. 2013, doi: 10.1063/1.4813115.

[22] R. P. Zaccaria *et al.*, “Fully analytical description of adiabatic compression in dissipative polaritonic structures,” *Phys. Rev. B*, vol. 86, no. 3, p. 035410, Jul. 2012, doi: 10.1103/PhysRevB.86.035410.

[23] A. L. Demming, F. Festy, and D. Richards, “Plasmon resonances on metal tips: Understanding tip-enhanced Raman scattering,” *J. Chem. Phys.*, vol. 122, no. 18, p. 184716, May 2005, doi: 10.1063/1.1896356.

[24] B. Gholipour *et al.*, “Plasmonic Nanowire Continuum Light Source,” in *2014 Conference on Lasers and Electro-Optics (cleo)*, New York: Ieee, 2014.

[25] Z. Chenari, H. Latifi, S. Ghamari, R. S. Hashemi, and F. Doroodmand, “Adiabatic tapered optical fiber fabrication in two step etching,” *Opt. Laser Technol.*, vol. 76, pp. 91–95, Jan. 2016, doi: 10.1016/j.optlastec.2015.05.024.

[26] L. M. Tong *et al.*, “Subwavelength-diameter silica wires for low-loss optical wave guiding,” *Nature*, vol. 426, no. 6968, pp. 816–819, Dec. 2003, doi: 10.1038/nature02193.

[27] T. E. Dimmick, G. Kakarantzas, T. A. Birks, and P. S. Russell, “Carbon dioxide laser fabrication of fused-fiber couplers and tapers,” *Appl. Optics*, vol. 38, no. 33, pp. 6845–6848, Nov. 1999, doi: 10.1364/AO.38.006845.

[28] G. Brambilla, V. Finazzi, and D. J. Richardson, “Ultra-low-loss optical fiber nanotapers,” *Opt. Express*, vol. 12, no. 10, pp. 2258–2263, May 2004, doi: 10.1364/OPEX.12.002258.

[29] T. Birks and Y. Li, “The Shape of Fiber Tapers,” *J. Lightwave Technol.*, vol. 10, no. 4, pp. 432–438, Apr. 1992, doi: 10.1109/50.134196.

[30] L. Eldada and L. W. Shacklette, “Advances in polymer integrated optics,” *IEEE J. Sel. Top. Quantum Electron.*, vol. 6, no. 1, pp. 54–68, Feb. 2000, doi: 10.1109/2944.826873.

[31] J. S. Koo, P. G. R. Smith, R. B. Williams, C. Riziotis, and M. C. Grossel, “UV written waveguides using crosslinkable PMMA-based copolymers,” *Opt. Mater.*, vol. 23, no. 3–4, pp. 583–592, Sep. 2003, doi: 10.1016/S0925-3467(03)00025-9.

[32] V. Pruneri, C. Riziotis, P. G. R. Smith, and A. Vasilakos, “Fiber and Integrated Waveguide-Based Optical Sensors,” *Journal of Sensors*, 2009. https://www.hindawi.com/journals/js/2009/171748/ (accessed Jul. 16, 2019).

[33] N. Aspiotis *et al.*, “Diffractive Ammonia Sensors Based on Sol-Gel Nanocomposites Materials,” *Sens. Lett.*, vol. 11, no. 8, pp. 1415–1419, Aug. 2013, doi: 10.1166/sl.2013.2945.

[34] N. Aspiotis *et al.*, “Ultra Low Cost Rapid Prototyping Of Diffraction Grating Remote Point Gas Sensors,” in *Materials and Applications for Sensors and Transducers Ii*, vol. 543, E. Hristoforou and D. S. Vlachos, Eds. Stafa-Zurich: Trans Tech Publications Ltd, 2013, pp. 377–380.

[35] A. El Sachat *et al.*, “Multianalytes Gas Sensors by Soft Lithography Induced Gratings with Sol-Gel and Copolymers Nanocomposites,” in *Nanotechnology in the Security Systems*, J. Bonca and S. Kruchinin, Eds. Dordrecht: Springer, 2015, pp. 181–192.

[36] F. Poncin-Epaillard *et al.*, “Surface Treatment of Polymeric Materials Controlling the Adhesion of Biomolecules,” *Journal of Functional Biomaterials*, vol. 3, no. 3, pp. 528–543, Sep. 2012, doi: 10.3390/jfb3030528.

[37] T. G. Vladkova, “Surface Engineered Polymeric Biomaterials with Improved Biocontact Properties,” *Int. J. Polym. Sci.*, p. 296094, 2010, doi: 10.1155/2010/296094.

[38] A. El Sachat, A. Meristoudi, S. Pispas, and C. Riziotis, “Assessment of Block and Random Copolymer Overlayers on Polymer Optical Fibers Toward Protein Detection Through Electrostatic Interaction,” *J. Polym. Sci. Pt. B-Polym. Phys.*, vol. 53, no. 5, pp. 327–334, Mar. 2015, doi: 10.1002/polb.23632.

[39] L. Athanasekos, A. El Sachat, S. Pispas, and C. Riziotis, “Amphiphilic Diblock Copolymer-Based Multiagent Photonic Sensing Scheme,” *J. Polym. Sci. Pt. B-Polym. Phys.*, vol. 52, no. 1, pp. 46–54, Jan. 2014, doi: 10.1002/polb.23388.

[40] Z. Zhao and Y. Duan, “A low cost fiber-optic humidity sensor based on silica sol-gel film,” *Sens. Actuator B-Chem.*, vol. 160, no. 1, pp. 1340–1345, Dec. 2011, doi: 10.1016/j.snb.2011.09.072.

[41] P. V. Preejith, C. S. Lim, A. Kishen, M. S. John, and A. Asundi, “Total protein measurement using a fiber-optic evanescent wave-based biosensor,” *Biotechnol. Lett.*, vol. 25, no. 2, pp. 105–110, Jan. 2003, doi: 10.1023/A:1021955032291.

[42] A. El Sachat *et al.*, “Characterization of Industrial Coolant Fluids and Continuous Ageing Monitoring by Wireless Node-Enabled Fiber Optic Sensors,” *Sensors*, vol. 17, no. 3, p. 568, Mar. 2017, doi: 10.3390/s17030568.

[43] S. F. Memon, E. Lewis, M. M. Ali, J. T. Pembroke, and B. S. Chowdhry, *U-bend Evanescent Wave Plastic Optical Fibre Sensor for Minute Level Concentration Detection of Ethanol Corresponding to Biofuel Production Rate*. New York: Ieee, 2017.

[44] S. Sharifpour-Boushehri, S. M. Hosseini-Golgoo, and M.-H. Sheikhi, “A low cost and reliable fiber optic ethanol sensor based on nano-sized SnO2,” *Opt. Fiber Technol.*, vol. 24, pp. 93–99, Aug. 2015, doi: 10.1016/j.yofte.2015.05.002.

[45] Z. M. Huang and S. Ramakrishna, “Modeling inelastic and strength properties of textile laminates: a unified approach,” *Compos. Sci. Technol.*, vol. 63, no. 3–4, pp. 445–466, 2003, doi: 10.1016/S0266-3538(02)00220-8.

[46] D. H. Reneker, A. L. Yarin, E. Zussman, and H. Xu, “Electrospinning of nanofibers from polymer solutions and melts,” in *Advances in Applied Mechanics, Vol 41*, vol. 41, H. Aref and E. VanDerGiessen, Eds. San Diego: Elsevier Academic Press Inc, 2007, pp. 43–195.

[47] P. Gibson, H. Schreuder-Gibson, and D. Rivin, “Transport properties of porous membranes based on electrospun nanofibers,” *Colloid Surf. A-Physicochem. Eng. Asp.*, vol. 187, pp. 469–481, Aug. 2001, doi: 10.1016/S0927-7757(01)00616-1.

[48] X. Y. Wang, C. Drew, S. H. Lee, K. J. Senecal, J. Kumar, and L. A. Sarnuelson, “Electrospun nanofibrous membranes for highly sensitive optical sensors,” *Nano Lett.*, vol. 2, no. 11, pp. 1273–1275, Nov. 2002, doi: 10.1021/nl020216u.

[49] B. Ding, M. Wang, J. Yu, and G. Sun, “Gas Sensors Based on Electrospun Nanofibers,” *Sensors*, vol. 9, no. 3, pp. 1609–1624, Mar. 2009, doi: 10.3390/s90301609.

[50] A. Urrutia, J. Goicoechea, P. J. Rivero, I. R. Matias, and F. J. Arregui, “Electrospun nanofiber mats for evanescent optical fiber sensors,” *Sens. Actuator B-Chem.*, vol. 176, pp. 569–576, Jan. 2013, doi: 10.1016/j.snb.2012.10.009.

[51] G. Kakarantzas, S. G. Leon-Saval, T. A. Birks, and P. S. J. Russell, “Low-loss deposition of solgel-derived silica films on tapered fibers,” *Opt. Lett.*, vol. 29, no. 7, pp. 694–696, Apr. 2004, doi: 10.1364/OL.29.000694.

[52] A. Petropoulou, M. N. Zervas, and C. Riziotis, “Optimized design of metal-coated optical fiber tips with embedded plasmonic slot nano-resonators for maximum field enhancement,” in *Nanophotonics and Micro/Nano Optics Iii*, vol. 10027, Z. Zhou and K. Wada, Eds. Bellingham: Spie-Int Soc Optical Engineering, 2016, p. UNSP 100271G.

[53] A. Petropoulou *et al.*, “Robust plasmonic tips fabricated by the tapering of composite hybrid silicate microfibers with metallic core,” in *Plasmonics Ii*, vol. 10028, H. Xu, S. Kawata, D. J. Bergman, and X. Zhu, Eds. Bellingham: Spie-Int Soc Optical Engineering, 2016, p. UNSP 100280N.

[54] M. Mivelle *et al.*, “Bowtie nano-aperture as interface between near-fields and a single-mode fiber,” *Opt. Express*, vol. 18, no. 15, pp. 15964–15974, Jul. 2010, doi: 10.1364/OE.18.015964.
[55] A. El Eter *et al.*, “Fiber-integrated optical nano-tweezer based on a bowtie-aperture nano-antenna at the apex of a SNOM tip,” *Opt. Express*, vol. 22, no. 8, pp. 10072–10080, Apr. 2014, doi: 10.1364/OE.22.010072.
[56] F. I. Baida and T. Grosjean, “Double-way spectral tunability for the control of optical nanocavity resonance,” *Sci Rep*, vol. 5, p. 17907, Dec. 2015, doi: 10.1038/srep17907.
[57] J. Song, R. P. Zaccaria, G. Dong, E. Di Fabrizio, M. B. Yu, and G. Q. Lo, “Evolution of modes in a metal-coated nano-fiber,” *Opt. Express*, vol. 19, no. 25, pp. 25206–25221, Dec. 2011, doi: 10.1364/OE.19.025206.
[58] H. Guo *et al.*, “Optical resonances of bowtie slot antennas and their geometry and material dependence,” *Opt. Express*, vol. 16, no. 11, pp. 7756–7766, May 2008, doi: 10.1364/OE.16.007756.
[59] W. Zhang, X. Cui, and O. J. F. Martin, “Local field enhancement of an infinite conical metal tip illuminated by a focused beam,” *J. Raman Spectrosc.*, vol. 40, no. 10, pp. 1338–1342, Oct. 2009, doi: 10.1002/jrs.2439.
[60] S. Ravets, J. E. Hoffman, P. R. Kordell, J. D. Wong-Campos, S. L. Rolston, and L. A. Orozco, “Intermodal energy transfer in a tapered optical fiber: optimizing transmission,” *J. Opt. Soc. Am. A-Opt. Image Sci. Vis.*, vol. 30, no. 11, pp. 2361–2371, Nov. 2013, doi: 10.1364/JOSAA.30.002361.
[61] C. Riziotis and A. V. Vasilakos, “Computational intelligence in photonics technology and optical networks: A survey and future perspectives,” *Inf. Sci.*, vol. 177, no. 23, pp. 5292–5315, Dec. 2007, doi: 10.1016/j.ins.2007.06.012.
[62] A. Alchalaby *et al.*, “Investigation of Plateau–Rayleigh Instability in Drawn Metal–Polymer Composite Fibers for Metamaterials Fabrication,” *Journal of Lightwave Technology*, vol. 34, no. 9, pp. 2198–2205, May 2016, doi: 10.1109/JLT.2015.2511022.
[63] A. Petropoulou *et al.*, “All-Fiber Plasmonic Platform Based on Hybrid Composite Metal/Glass Microwires,” *J. Phys. Chem. C*, vol. 122, no. 45, pp. 26169–26176, Nov. 2018, doi: 10.1021/acs.jpcc.8b08844.
[64] O. Aktas, E. Ozgur, O. Tobail, M. Kanik, E. Huseyinoglu, and M. Bayindir, “A New Route for Fabricating On-Chip Chalcogenide Microcavity Resonator Arrays,” *Adv. Opt. Mater.*, vol. 2, no. 7, pp. 618–625, Jul. 2014, doi: 10.1002/adom.201400072.
[65] P. Bastock, “Manufacturing novel fibre,” PhD Thesis, University of Southampton, 2015.
[66] M. E. Toimil-Molares, A. G. Balogh, T. W. Cornelius, R. Neumann, and C. Trautmann, “Fragmentation of nanowires driven by Rayleigh instability,” *Appl. Phys. Lett.*, vol. 85, no. 22, pp. 5337–5339, Nov. 2004, doi: 10.1063/1.1826237.
[67] S. Karim *et al.*, “Morphological evolution of Au nanowires controlled by Rayleigh instability,” *Nanotechnology*, vol. 17, no. 24, pp. 5954–5959, Dec. 2006, doi: 10.1088/0957-4484/17/24/009.
[68] D. S. Deng, J.-C. Nave, X. Liang, S. G. Johnson, and Y. Fink, “Exploration of in-fiber nanostructures from capillary instability,” *Opt. Express*, vol. 19, no. 17, pp. 16273–16290, Aug. 2011, doi: 10.1364/OE.19.016273.
[69] D. S. Deng *et al.*, “In-Fiber Semiconductor Filament Arrays,” *Nano Lett.*, vol. 8, no. 12, pp. 4265–4269, Dec. 2008, doi: 10.1021/nl801979w.
[70] D. S. Deng, N. D. Orf, S. Danto, A. F. Abouraddy, J. D. Joannopoulos, and Y. Fink, “Processing and properties of centimeter-long, in-fiber, crystalline-selenium filaments,” *Appl. Phys. Lett.*, vol. 96, no. 2, p. 023102, Jan. 2010, doi: 10.1063/1.3275751.
[71] A. Gumennik *et al.*, “Silicon-in-silica spheres via axial thermal gradient in-fibre capillary instabilities,” *Nat. Commun.*, vol. 4, p. 2216, Jul. 2013, doi: 10.1038/ncomms3216.
[72] J. J. Kaufman *et al.*, “Structured spheres generated by an in-fibre fluid instability,” *Nature*, vol. 487, no. 7408, pp. 463–467, Jul. 2012, doi: 10.1038/nature11215.

[73] G. Tao *et al.*, “Digital design of multimaterial photonic particles,” *Proc. Natl. Acad. Sci. U. S. A.*, vol. 113, no. 25, pp. 6839–6844, Jun. 2016, doi: 10.1073/pnas.1601777113.

[74] Y. Qin, S.-M. Lee, A. Pan, U. Gosele, and M. Knez, “Rayleigh-instability-induced metal nanoparticle chains encapsulated in nanotubes produced by atomic layer deposition,” *Nano Lett.*, vol. 8, no. 1, pp. 114–118, Jan. 2008, doi: 10.1021/nl0721766.

[75] D. Handapangoda, M. Premaratne, I. D. Rukhlenko, and C. Jagadish, “Optimal design of composite nanowires for extended reach of surface plasmon-polaritons,” *Opt. Express*, vol. 19, no. 17, pp. 16058–16074, Aug. 2011, doi: 10.1364/OE.19.016058.

[76] D. K. Gramotnev, M. W. Vogel, and M. I. Stockman, “Optimized nonadiabatic nanofocusing of plasmons by tapered metal rods,” *J. Appl. Phys.*, vol. 104, no. 3, p. 034311, Aug. 2008, doi: 10.1063/1.2963699.

[77] A. Wiener, A. I. Fernandez-Dominguez, A. P. Horsfield, J. B. Pendry, and S. A. Maier, “Nonlocal Effects in the Nanofocusing Performance of Plasmonic Tips,” *Nano Lett.*, vol. 12, no. 6, pp. 3308–3314, Jun. 2012, doi: 10.1021/nl301478n.

[78] R.-H. Jiang, C. Chen, D.-Z. Lin, H.-C. Chou, J.-Y. Chu, and T.-J. Yen, “Near-Field Plasmonic Probe with Super Resolution and High Throughput and Signal-to-Noise Ratio,” *Nano Lett.*, vol. 18, no. 2, pp. 881–885, Feb. 2018, doi: 10.1021/acs.nanolett.7b04142.

[79] S. Shabahang, J. J. Kaufman, D. S. Deng, and A. F. Abouraddy, “Observation of the Plateau-Rayleigh capillary instability in multi-material optical fibers,” *Appl. Phys. Lett.*, vol. 99, no. 16, p. 161909, Oct. 2011, doi: 10.1063/1.3653247.

[80] R. Mead-Hunter, A. J. C. King, and B. J. Mullins, “Plateau Rayleigh Instability Simulation,” *Langmuir*, vol. 28, no. 17, pp. 6731–6735, May 2012, doi: 10.1021/la300622h.

[81] J. J. Kaufman *et al.*, “In-fiber production of polymeric particles for biosensing and encapsulation,” *Proc. Natl. Acad. Sci. U. S. A.*, vol. 110, no. 39, pp. 15549–15554, Sep. 2013, doi: 10.1073/pnas.1310214110.

[82] S. Tomotika, “On the Instability of a Cylindrical Thread of a Viscous Liquid Surrounded by Another Viscous Fluid,” *Proceedings of the Royal Society of London Series A*, vol. 150, pp. 322–337, Jun. 1935, doi: 10.1098/rspa.1935.0104.

[83] P. T. Barton, B. Obadia, and D. Drikakis, “A conservative level-set based method for compressible solid/fluid problems on fixed grids,” *J. Comput. Phys.*, vol. 230, no. 21, pp. 7867–7890, Sep. 2011, doi: 10.1016/j.jcp.2011.07.008.

[84] P. T. Barton, D. Drikakis, and E. I. Romenski, “An Eulerian finite-volume scheme for large elastoplastic deformations in solids,” *Int. J. Numer. Methods Eng.*, vol. 81, no. 4, pp. 453–484, Jan. 2010, doi: 10.1002/nme.2695.

[85] P. T. Barton and D. Drikakis, “An Eulerian method for multi-component problems in non-linear elasticity with sliding interfaces,” *J. Comput. Phys.*, vol. 229, no. 15, pp. 5518–5540, Aug. 2010, doi: 10.1016/j.jcp.2010.04.012.

[86] X. Fan and I. M. White, “Optofluidic microsystems for chemical and biological analysis,” *Nat. Photonics*, vol. 5, no. 10, pp. 591–597, Oct. 2011, doi: 10.1038/NPHOTON.2011.206.

[87] A. Petropoulou, M. N. Zervas, and C. Riziotis, “Design optimization of gold-coated fiber tips with embedded plasmonic slot nanoresonators,” *J. Opt.*, vol. 19, no. 5, p. 055002, May 2017, doi: 10.1088/2040-8986/aa6356.

[88] C. Caucheteur, T. Guo, and J. Albert, “Review of plasmonic fiber optic biochemical sensors: improving the limit of detection,” *Anal. Bioanal. Chem.*, vol. 407, no. 14, pp. 3883–3897, May 2015, doi: 10.1007/s00216-014-8411-6.

[89] T. Riedel *et al.*, “Hepatitis B plasmonic biosensor for the analysis of clinical serum samples,” *Biosens. Bioelectron.*, vol. 85, pp. 272–279, Nov. 2016, doi: 10.1016/j.bios.2016.05.014.

[90] W. Zhang, N. Ganesh, I. D. Block, and B. T. Cunningham, “High sensitivity photonic crystal biosensor incorporating nanorod structures for enhanced surface area,” *Sens. Actuator B-Chem.*, vol. 131, no. 1, pp. 279–284, Apr. 2008, doi: 10.1016/j.snb.2007.11.017.

[91] T.-X. Liu, L. Zhang, R.-P. Liang, and J.-D. Qiu, “Highly selective detection of disulfenylated proteins through a dimedone-based fluorescent probe and application in cells,” *Sens. Actuator B-Chem.*, vol. 238, pp. 257–263, Feb. 2017, doi: 10.1016/j.snb.2016.07.030.

[92] F. Vollmer and L. Yang, “Label-free detection with high-Q microcavities: a review of biosensing mechanisms for integrated devices,” *Nanophotonics*, vol. 1, no. 3–4, pp. 267–291, 2012, doi: 10.1515/nanoph-2012-0021.

[93] G. C. Righini and S. Soria, “Biosensing by WGM Microspherical Resonators,” *Sensors*, vol. 16, no. 6, p. 905, Jun. 2016, doi: 10.3390/s16060905.

[94] “Block Copolymers: Synthetic Strategies, Physical Properties, and Applications,” *Wiley.com*. https://www.wiley.com/en-us/Block+Copolymers%3A+Synthetic+Strategies%2C+Physical+Properties%2C+and+Applications-p-9780471394365 (accessed Jul. 16, 2019).

[95] O. Webster, “Living Polymerization Methods,” *Science*, vol. 251, no. 4996, pp. 887–893, Feb. 1991, doi: 10.1126/science.251.4996.887.

[96] J. Chiefari *et al.*, “Living free-radical polymerization by reversible addition-fragmentation chain transfer: The RAFT process,” *Macromolecules*, vol. 31, no. 16, pp. 5559–5562, Aug. 1998, doi: 10.1021/ma9804951.

[97] G. Moad, E. Rizzardo, and S. H. Thang, “Living Radical Polymerization by the RAFT Process - A Second Update,” *Aust. J. Chem.*, vol. 62, no. 11, pp. 1402–1472, 2009, doi: 10.1071/CH09311.

[98] E. Themistou, G. Battaglia, and S. P. Armes, “Facile synthesis of thiol-functionalized amphiphilic polylactide-methacrylic diblock copolymers,” *Polym. Chem.*, vol. 5, no. 4, pp. 1405–1417, Feb. 2014, doi: 10.1039/c3py01446k.

[99] P. Viswanathan, E. Themistou, K. Ngamkham, G. C. Reilly, S. P. Armes, and G. Battaglia, “Controlling Surface Topology and Functionality of Electrospun Fibers on the Nanoscale using Amphiphilic Block Copolymers To Direct Mesenchymal Progenitor Cell Adhesion,” *Biomacromolecules*, vol. 16, no. 1, pp. 66–75, Jan. 2015, doi: 10.1021/bm500671j.

[100] K. Kalli *et al.*, “Flat fibre and femtosecond laser technology as a novel photonic integration platform for optofluidic based biosensing devices and lab-on-chip applications: Current results and future perspectives,” *Sens. Actuator B-Chem.*, vol. 209, pp. 1030–1040, Mar. 2015, doi: 10.1016/j.snb.2014.12.003.

[101] T. Subbiah, G. S. Bhat, R. W. Tock, S. Pararneswaran, and S. S. Ramkumar, “Electrospinning of nanofibers,” *J. Appl. Polym. Sci.*, vol. 96, no. 2, pp. 557–569, Apr. 2005, doi: 10.1002/app.21481.

[102] Z. M. Huang, Y. Z. Zhang, M. Kotaki, and S. Ramakrishna, “A review on polymer nanofibers by electrospinning and their applications in nanocomposites,” *Compos. Sci. Technol.*, vol. 63, no. 15, pp. 2223–2253, Nov. 2003, doi: 10.1016/S0266-3538(03)00178-7.

[103] J. Xue, J. Xie, W. Liu, and Y. Xia, “Electrospun Nanofibers: New Concepts, Materials, and Applications,” *Accounts Chem. Res.*, vol. 50, no. 8, pp. 1976–1987, Aug. 2017, doi: 10.1021/acs.accounts.7b00218.

[104] A. Senthamizhan *et al.*, “Highly Fluorescent Pyrene-Functional Polystyrene Copolymer Nanofibers for Enhanced Sensing Performance of TNT,” *ACS Appl. Mater. Interfaces*, vol. 7, no. 38, pp. 21038–21046, Sep. 2015, doi: 10.1021/acsami.5b07184.

[105] W. Wang *et al.*, “Preparation of fluorescent nanofibrous film as a sensing material and adsorbent for Cu2+ in aqueous solution via copolymerization and electrospinning,” *J. Hazard. Mater.*, vol. 194, pp. 185–192, Oct. 2011, doi: 10.1016/j.jhazmat.2011.07.083.

[106] Y.-Y. Lv, J. Wu, and Z.-K. Xu, “Colorimetric and fluorescent sensor constructing from the nanofibrous membrane of porphyrinated polyimide for the detection of hydrogen chloride gas,” *Sens. Actuator B-Chem.*, vol. 148, no. 1, pp. 233–239, Jun. 2010, doi: 10.1016/j.snb.2010.05.029.

[107] Y. Yang *et al.*, "A simple fabrication of electrospun nanofiber sensing materials based on fluorophore-doped polymer," *J. Mater. Chem.*, vol. 19, no. 39, pp. 7290–7295, 2009, doi: 10.1039/b908154b.
[108] B. W. Davis, N. Niamnont, C. D. Hare, M. Sukwattanasinitt, and Q. Cheng, "Nanofibers Doped with Dendritic Fluorophores for Protein Detection," *ACS Appl. Mater. Interfaces*, vol. 2, no. 7, pp. 1798–1803, Jul. 2010, doi: 10.1021/am100345g.
[109] J. Mosinger *et al.*, "Fluorescent Polyurethane Nanofabrics: A Source of Singlet Oxygen and Oxygen Sensing," *Langmuir*, vol. 26, no. 12, pp. 10050–10056, Jun. 2010, doi: 10.1021/la1001607.
[110] X. He *et al.*, "Electrospun quantum dots/polymer composite porous fibers for turn-on fluorescent detection of lactate dehydrogenase," *J. Mater. Chem.*, vol. 22, no. 35, pp. 18471–18478, 2012, doi: 10.1039/c2jm33078d.
[111] C. Liu *et al.*, "Nanomolar fluorescent quantitative detection of formaldehyde with a 8-hydroxyquinoline derivative in aqueous solution and electrospun nanofibers," *Sens. Actuator B-Chem.*, vol. 219, pp. 185–191, Nov. 2015, doi: 10.1016/j.snb.2015.04.131.
[112] J. Hargreaves and S. Webber, "Photophysics of Anthracene Polymers - Fluorescence, Singlet Energy Migration, and Photodegradation," *Macromolecules*, vol. 17, no. 2, pp. 235–240, 1984, doi: 10.1021/ma00132a020.
[113] R. Martinez-Manez and F. Sancenon, "Fluorogenic and chromogenic chemosensors and reagents for anions," *Chem. Rev.*, vol. 103, no. 11, pp. 4419–4476, Nov. 2003, doi: 10.1021/cr010421e.
[114] H. Mori, I. Tando, and H. Tanaka, "Synthesis and Optoelectronic Properties of Alternating Copolymers Containing Anthracene Unit in The Main Chain by Radical Ring-Opening Polymerization," *Macromolecules*, vol. 43, no. 17, pp. 7011–7020, Sep. 2010, doi: 10.1021/ma100820z.
[115] J.-H. Park *et al.*, "New anthracene-thiophene-based copolymers that absorb across the entire UV-vis spectrum for application in organic solar cells," *Chem. Commun.*, vol. 46, no. 11, pp. 1863–1865, 2010, doi: 10.1039/b921691j.
[116] G. Roberts, M. Mcginnity, W. Barlow, and P. Vincett, "Electroluminescence, Photo-Luminescence and Electroabsorption of a Lightly Substituted Anthracene Langmuir Film," *Solid State Commun.*, vol. 32, no. 8, pp. 683–686, 1979, doi: 10.1016/0038-1098(79)90728-2.
[117] K. Hriz, N. Jaballah, M. Chemli, J. L. Fave, and M. Majdoub, "Synthesis and Characterization of New Anthracene-Based Semiconducting Polyethers," *J. Appl. Polym. Sci.*, vol. 119, no. 3, pp. 1443–1449, Feb. 2011, doi: 10.1002/app.32659.
[118] T. S. Li, J. F. Chen, M. Mitsuishi, and T. Miyashita, "Photolithographic properties of ultrathin polymer Langmuir-Blodgett films containing anthracene moieties," *J. Mater. Chem.*, vol. 13, no. 7, pp. 1565–1569, 2003, doi: 10.1039/b300686g.
[119] K. H. Chae, Y. W. Kim, and T. H. Kim, "Application of an anthracene containing polymer to a negative type photoresist," *Bull. Korean Chem. Soc.*, vol. 23, no. 9, pp. 1351–1354, Sep. 2002.
[120] M. Demetriou and T. Krasia-Christoforou, "Well-Defined Diblock Copolymers Possessing Fluorescent and Metal Chelating Functionalities as Novel Macromolecular Sensors for Amines and Metal Ions," *J. Polym. Sci. Pol. Chem.*, vol. 50, no. 1, pp. 52–60, Jan. 2012, doi: 10.1002/pola.24977.
[121] R. Kanya and Y. Ohshima, "Electronic spectrum of the anthracene-ammonia complex," *Phys. Chem. Chem. Phys.*, vol. 5, no. 18, pp. 3851–3858, Sep. 2003, doi: 10.1039/b305673b.
[122] M. Liong *et al.*, "Multifunctional inorganic nanoparticles for imaging, targeting, and drug delivery," *ACS Nano*, vol. 2, no. 5, pp. 889–896, May 2008, doi: 10.1021/nn800072t.
[123] S. Ma *et al.*, "Nanogenerators Begin to Light Up: A Novel Poling-Free Piezoelectric System with Multicolor Photoluminescence as an Efficient Mechatronics Development Platform," *Adv. Mater. Interfaces*, vol. 5, no. 19, p. 1800587, Oct. 2018, doi: 10.1002/admi.201800587.

[124] N. C. Bigall, W. J. Parak, and D. Dorfs, “Fluorescent, magnetic and plasmonic-Hybrid multifunctional colloidal nano objects,” *Nano Today*, vol. 7, no. 4, pp. 282–296, Aug. 2012, doi: 10.1016/j.nantod.2012.06.007.

[125] X. Le *et al.*, “Palladium nanoparticles immobilized on core-shell magnetic fibers as a highly efficient and recyclable heterogeneous catalyst for the reduction of 4-nitrophenol and Suzuki coupling reactions,” *J. Mater. Chem. A*, vol. 2, no. 46, pp. 19696–19706, 2014, doi: 10.1039/c4ta04919e.

[126] J. O. Marques Neto, C. R. Bellato, C. H. F. de Souza, R. C. da Silva, and P. A. Rocha, “Synthesis, Characterization and Enhanced Photocatalytic Activity of Iron Oxide/Carbon Nanotube/Ag-doped TiO2 Nanocomposites,” *J. Braz. Chem. Soc.*, vol. 28, no. 12, pp. 2301–2312, Dec. 2017, doi: 10.21577/0103-5053.20170081.

[127] H. D. Cancar *et al.*, “A Novel Acetylcholinesterase Biosensor: Core-Shell Magnetic Nanoparticles Incorporating a Conjugated Polymer for the Detection of Organophosphorus Pesticides,” *ACS Appl. Mater. Interfaces*, vol. 8, no. 12, pp. 8058–8067, Mar. 2016, doi: 10.1021/acsami.5b12383.

[128] S. A. Corr, Y. P. Rakovich, and Y. K. Gun’ko, “Multifunctional magnetic-fluorescent nanocomposites for biomedical applications,” *Nanoscale Res. Lett.*, vol. 3, no. 3, pp. 87–104, Mar. 2008, doi: 10.1007/s11671-008-9122-8.

[129] S. Kralj, M. Rojnik, R. Romih, M. Jagodic, J. Kos, and D. Makovec, “Effect of surface charge on the cellular uptake of fluorescent magnetic nanoparticles,” *J. Nanopart. Res.*, vol. 14, no. 10, p. 1151, Oct. 2012, doi: 10.1007/s11051-012-1151-7.

[130] S. Kralj, M. Rojnik, J. Kos, and D. Makovec, “Targeting EGFR-overexpressed A431 cells with EGF-labeled silica-coated magnetic nanoparticles,” *J. Nanopart. Res.*, vol. 15, no. 5, p. 1666, May 2013, doi: 10.1007/s11051-013-1666-6.

[131] O. Chen *et al.*, “Magneto-fluorescent core-shell supernanoparticles,” *Nat. Commun.*, vol. 5, p. 5093, Oct. 2014, doi: 10.1038/ncomms6093.

[132] J. Kim *et al.*, “Multifunctional Uniform Nanoparticles Composed of a Magnetite Nanocrystal Core and a Mesoporous Silica Shell for Magnetic Resonance and Fluorescence Imaging and for Drug Delivery,” *Angew. Chem.-Int. Edit.*, vol. 47, no. 44, pp. 8438–8441, 2008, doi: 10.1002/anie.200802469.

[133] S. Kralj, T. Potrc, P. Kocbek, S. Marchesan, and D. Makovec, “Design and Fabrication of Magnetically Responsive Nanocarriers for Drug Delivery,” *Curr. Med. Chem.*, vol. 24, no. 5, pp. 454–469, 2017, doi: 10.2174/0929867323666160813211736.

[134] X. F. Zhang, L. Clime, H. Q. Ly, M. Trudeau, and T. Veres, “Multifunctional Fe3O4-Au/Porous Silica@Fluorescein Core/Shell Nanoparticles with Enhanced Fluorescence Quantum Yield,” *J. Phys. Chem. C*, vol. 114, no. 43, pp. 18313–18317, Nov. 2010, doi: 10.1021/jp1051112.

[135] M. Beija, C. A. M. Afonso, and J. M. G. Martinho, “Synthesis and applications of Rhodamine derivatives as fluorescent probes,” *Chem. Soc. Rev.*, vol. 38, no. 8, pp. 2410–2433, 2009, doi: 10.1039/b901612k.

[136] L. Song, E. Hennink, I. Young, and H. Tanke, “Photobleaching Kinetics of Fluorescein in Quantitative Fluorescence Microscopy,” *Biophys. J.*, vol. 68, no. 6, pp. 2588–2600, Jun. 1995, doi: 10.1016/S0006-3495(95)80442-X.

[137] J. Zhu *et al.*, “Electrospun Polyimide Nanocomposite Fibers Reinforced with Core-Shell Fe-FeO Nanoparticles,” *J. Phys. Chem. C*, vol. 114, no. 19, pp. 8844–8850, May 2010, doi: 10.1021/jp1020033.

[138] J. Zhu, S. Wei, D. Rutman, N. Haldolaarachchige, D. R. Young, and Z. Guo, “Magnetic polyacrylonitrile-Fe@FeO nanocomposite fibers - Electrospinning, stabilization and carbonization,” *Polymer*, vol. 52, no. 13, pp. 2947–2955, Jun. 2011, doi: 10.1016/j.polymer.2011.04.034.

[139] A. Petropoulou, K. Christodoulou, C. Polydorou, T. Krasia-Christoforou, and C. Riziotis, “Cost-Effective Polymethacrylate-Based Electrospun Fluorescent Fibers toward Ammonia Sensing,”

Macromol. Mater. Eng., vol. 302, no. 8, p. UNSP 1600453, Aug. 2017, doi: 10.1002/mame.201600453.

[140] M. Min, X. Wang, Y. Chen, L. Wang, H. Huang, and J. Shi, "Highly sensitive and selective Cu2+ sensor based on electrospun rhodamine dye doped poly(ether sulfones) nanofibers," *Sens. Actuator B-Chem.*, vol. 188, pp. 365–371, Nov. 2013, doi: 10.1016/j.snb.2013.07.017.

[141] N. Horzum, D. Mete, E. Karakus, M. Ucuncu, M. Emrullahoglu, and M. M. Demir, "Rhodamine-Immobilised Electrospun Chitosan Nanofibrous Material as a Fluorescence Turn-On Hg2+ Sensor," *ChemistrySelect*, vol. 1, no. 5, pp. 896–900, Apr. 2016, doi: 10.1002/slct.201600027.

[142] F. J. Orriach-Fernandez, A. L. Medina-Castillo, J. E. Diaz-Gomez, A. Munoz de la Pena, J. F. Fernandez-Sanchez, and A. Fernandez-Gutierrez, "A sensing microfibre mat produced by electrospinning for the turn-on luminescence determination of Hg2+ in water samples," *Sens. Actuator B-Chem.*, vol. 195, pp. 8–14, May 2014, doi: 10.1016/j.snb.2014.01.010.

[143] M. W. Frey, "Electrospinning cellulose and cellulose derivatives," *Polym. Rev.*, vol. 48, no. 2, pp. 378–391, 2008, doi: 10.1080/15583720802022281.

[144] L. Li, Z. Jiang, M. Li, R. Li, and T. Fang, "Hierarchically structured PMMA fibers fabricated by electrospinning," *RSC Adv.*, vol. 4, no. 95, pp. 52973–52985, 2014, doi: 10.1039/c4ra05385k.

[145] N. Tomczak, S. Gu, M. Han, N. F. van Hulst, and G. J. Vancso, "Single light emitters in electrospun polymer nanofibers: Effect of local confinement on radiative decay," *Eur. Polym. J.*, vol. 42, no. 10, pp. 2205–2210, Oct. 2006, doi: 10.1016/j.eurpolymj.2006.06.017.

[146] G. H. F. Melo, J. P. F. Santos, A. J. Gualdi, C.-M. Tsai, W. M. Sigmund, and R. E. S. Bretas, "Correlation between electrospinning parameters and magnetic properties of BiFeO3 nanofibers," *Electrospinning*, vol. 1, no. 1, pp. 73–86, 2017, doi: 10.1515/esp-2017-0004.

[147] B.-X. Wei, L. Zhao, T.-J. Wang, H. Gao, H.-X. Wu, and Y. Jin, "Photo-stability of TiO2 particles coated with several transition metal oxides and its measurement by rhodamine-B degradation," *Adv. Powder Technol.*, vol. 24, no. 3, pp. 708–713, May 2013, doi: 10.1016/j.apt.2012.12.009.

[148] A. K. Gaigalas, L. Wang, and R. F. Vogt, "Frequency-domain measurement of the photodegradation process of fluorescein," *Photochem. Photobiol.*, vol. 76, no. 1, pp. 22–28, Jul. 2002, doi: 10.1562/0031-8655(2002)076<0022:FDMOTP>2.0.CO;2.

[149] A. S. Kristoffersen, S. R. Erga, B. Hamre, and O. Frette, "Testing Fluorescence Lifetime Standards using Two-Photon Excitation and Time-Domain Instrumentation: Rhodamine B, Coumarin 6 and Lucifer Yellow," *J. Fluoresc.*, vol. 24, no. 4, pp. 1015–1024, Jul. 2014, doi: 10.1007/s10895-014-1368-1.

[150] J. Arden, G. Deltau, V. Huth, U. Kringel, D. Peros, and K. Drexhage, "Fluorescence and Lasing Properties of Rhodamine Dyes," *J. Lumines.*, vol. 48–9, pp. 352–358, Feb. 1991, doi: 10.1016/0022-2313(91)90137-K.

[151] N. R. Chereddy, K. Suman, P. S. Korrapati, S. Thennarasu, and A. B. Mandal, "Design and synthesis of rhodamine based chemosensors for the detection of Fe3+ ions," *Dyes Pigment.*, vol. 95, no. 3, pp. 606–613, Dec. 2012, doi: 10.1016/j.dyepig.2012.05.025.

[152] C. Yee *et al.*, "Self-assembled monolayers of alkanesulfonic and -phosphonic acids on amorphous iron oxide nanoparticles," *Langmuir*, vol. 15, no. 21, pp. 7111–7115, Oct. 1999, doi: 10.1021/la990663y.

[153] W. Zhou, Y. Guo, H. Zhang, Y. Su, M. Liu, and B. Dong, "A highly sensitive ammonia sensor based on spinous core-shell PCL-PANI fibers," *J. Mater. Sci.*, vol. 52, no. 11, pp. 6554–6566, Jun. 2017, doi: 10.1007/s10853-017-0890-3.

[154] Y. Zhang, J. J. Kim, D. Chen, H. L. Tuller, and G. C. Rutledge, "Electrospun Polyaniline Fibers as Highly Sensitive Room Temperature Chemiresistive Sensors for Ammonia and Nitrogen Dioxide Gases," *Adv. Funct. Mater.*, vol. 24, no. 25, pp. 4005–4014, Jul. 2014, doi: 10.1002/adfm.201400185.

[155] J. He, T.-Y. Zhang, and G. Chen, “Ammonia gas-sensing characteristics of fluorescence-based poly(2-(acetoacetoxy)ethyl methacrylate) thin films,” *J. Colloid Interface Sci.*, vol. 373, pp. 94–101, May 2012, doi: 10.1016/j.jcis.2011.11.074.
[156] L. Peng *et al.*, “Gaseous ammonia fluorescence probe based on cellulose acetate modified microstructured optical fiber,” *Opt. Commun.*, vol. 284, no. 19, pp. 4810–4814, Sep. 2011, doi: 10.1016/j.optcom.2011.06.015.
[157] W.-C. Wu and H.-J. Lai, “Preparation of thermo-responsive electrospun nanofibers containing rhodamine-based fluorescent sensor for Cu2+ detection,” *J. Polym. Res.*, vol. 23, no. 11, p. 223, Oct. 2016, doi: 10.1007/s10965-016-1115-1.
[158] C. Preininger, G. J. Mohr, I. Klimant, and O. S. Wolfbeis, “Ammonia fluorosensors based on reversible lactonization of polymer-entrapped rhodamine dyes, and the effects of plasticizers,” *Analytica Chimica Acta*, vol. 334, no. 1, pp. 113–123, Nov. 1996, doi: 10.1016/S0003-2670(96)00269-3.
[159] B.-Y. Chen, C.-C. Kuo, C.-J. Cho, F.-C. Liang, and R.-J. Jeng, “Novel fluorescent chemosensory filter membranes composed of electrospun nanofibers with ultra-selective and reversible pH and Hg2+ sensing characteristics,” *Dyes and Pigments*, vol. 143, pp. 129–142, Aug. 2017, doi: 10.1016/j.dyepig.2017.04.023.
[160] C.-J. Cho, S.-T. Lu, C.-C. Kuo, F.-C. Liang, B.-Y. Chen, and C.-C. Chu, “Pyrene or rhodamine derivative-modified surfaces of electrospun nanofibrous chemosensors for colorimetric and fluorescent determination of Cu2+, Hg2+, and pH,” *React. Funct. Polym.*, vol. 108, pp. 137–147, Nov. 2016, doi: 10.1016/j.reactfunctpolym.2016.05.019.

List of Publications

[1] A. Petropoulou, S. Kralj, X. Karagiorgis, I. Savva, E. Loizides, M. Panagi, T. Krasia-Christoforou, and C. Riziotis "Multifunctional Gas and pH Fluorescent Sensors Based on Cellulose Acetate Electrospun Fibers Decorated with Rhodamine B-Functionalised Core-Shell Ferrous Nanoparticles," Scientific Reports, vol. 10, no. 1, p. 367, Jan. 2020, doi: 10.1038/s41598-019-57291-0.

[2] A. Petropoulou, G. Antonopoulos, P. Bastock, G. Kakarantzas, C. Craig, D. Drikakis, D. W. Hewak, M. N. Zervas, and C. Riziotis, "Design and Implementation of Fiber-embedded Plasmonic Structures in Microwires," in 2019 PhotonIcs Electromagnetics Research Symposium - Spring (PIERS-Spring), Jun. 2019, pp. 2951–2957, doi: 10.1109/PIERS-Spring46901.2019.9017635.

[3] A. Petropoulou, D. Drikakis, and C. Riziotis, "Microspheres Formation in a Glass–Metal Hybrid Fiber System: Application in Optical Microwires," Materials (Basel), vol. 12, no. 12, Jun. 2019, doi: 10.3390/ma12121969.

[4] A. Petropoulou, G. Antonopoulos, P. Bastock, G. Kakarantzas, C. Craig, D. W. Hewak, M. N. Zervas, and C. Riziotis, "All-Fiber Plasmonic Platform Based on Hybrid Composite Metal/Glass Microwires," J. Phys. Chem. C, vol. 122, no. 45, pp. 26169–26176, Nov. 2018, doi: 10.1021/acs.jpcc.8b08844.

[5] A. Petropoulou, T. J. Gibson, E. Themistou, S. Pispas, and C. Riziotis, "Development of amphiphilic block copolymers as silica optical fiber overlayers for BSA protein detection," Materials Chemistry and Physics, vol. 216, pp. 421–428, Sep. 2018, doi: 10.1016/j.matchemphys.2018.06.027.

[6] A. Petropoulou, K. Christodoulou, C. Polydorou, T. Krasia, and C. Riziotis, "Cost-Effective Polymethacrylate-Based Electrospun Fluorescent Fibers toward Ammonia Sensing," Macromolecular Materials and Engineering, vol. 302, p. 1600453, Aug. 2017, doi: 10.1002/mame.201600453.

[7] A. Petropoulou, M. Zervas, and C. Riziotis, "Design optimization of gold-coated fiber tips with embedded plasmonic slot nano-resonators," Journal of Optics, vol. 19, Feb. 2017, doi: 10.1088/2040-8986/aa6356.

[8] A. Petropoulou, T. J. Gibson, E. Themistou, S. Pispas, and C. Riziotis, "Amphiphilic block copolymer-based photonic platform towards efficient protein detection," in Advanced Sensor Systems and Applications VII, Nov. 2016, vol. 10025, p. 100250M, doi: 10.1117/12.2246506.

[9] A. Petropoulou, M. N. Zervas, and C. Riziotis, "Optimized design of metal-coated optical fiber tips with embedded plasmonic slot nano-resonators for maximum field enhancement," in Nanophotonics and Micro/Nano Optics III, Nov. 2016, vol. 10027, p. 100271G, doi: 10.1117/12.2246496.

[10] A. Petropoulou, G. Antonopoulos, P. Bastock, C. Craig, G. Kakarantzas, D. W. Hewak, M. N. Zervas, and C. Riziotis, "Robust plasmonic tips fabricated by the tapering of composite hybrid silicate microfibers with metallic core," presented at the SPIE/COS Photonics Asia, Beijing, China, Nov. 2016, p. 100280N, doi: 10.1117/12.2246508.

[11] A. Petropoulou, G. Antonopoulos, P. Bastock, C. Craig, G. Kakarantzas, D. W. Hewak, M. N. Zervas, and C. Riziotis, “Engineering of composite metallic microfibers towards development of plasmonic devices for sensing applications,” IOP Conf. Ser.: Mater. Sci. Eng., vol. 108, p. 012027, Mar. 2016, doi: 10.1088/1757-899X/108/1/012027.

[12] V. Aroni, G. Mountrichas, S. Pispas, A. Petropoulou, C. Riziotis, D. Hatziavramidis, “Study of irradiation time and laser flux for the synthesis of photocrosslinked PEG based hydrogels,” Proceedings of 3rd European Symposium of Photopolymer Science, 2014.

Conferences - Presentations

- A. Petropoulou, G. Antonopoulos, P. Bastock, C. Craig, G. Kakarantzas, D.W. Hewak, M.N. Zervas, C. Riziotis, "Robust plasmonic tips fabricated by the tapering of composite hybrid silicate microfibers with metallic core," *SPIE COS Photonics Asia, Beijing, China, 12-14 October 2016* (Invited Oral Presentation)
- K. Christodoulou, A. Petropoulou, C. Polydorou, T. Krasia Christoforou, C. Riziotis, "Anthracene-containing Electrospun fibers for ammonia gas sensing," *Electrospinning Conference: From Design and Processing to Advanced Nanomaterials and Applications, Cyprus 19-21 April 2017, Nicosia, Cyprus* (Oral)
- X. Karagiorgis, A. Petropoulou, I. Savva, C. Riziotis, S. Kralj, T. Krasia-Christoforou, "Fluorescent polymer-based nanocomposite electrospun fibers as optical sensors for ammonia and pH," *XXXIII Panhellenic Conference on Solid State Physics and Materials Science, University of Cyprus, 17-19 September 2018, Nicosia, Cyprus* (Poster)
- X. Karagiorgis, A. Petropoulou, I. Savva, Ch. Riziotis, S. Kralj, T. Krasia-Christoforou, “Fluorescent polymer-based nanocomposite electrospun fibers as optical sensors for ammonia and pH,” *International Conference on Nanotechnologies and Bionanoscience, Heraklion, Crete, Sep 2018, Greece* (Poster)
- A. Petropoulou, M. N. Zervas, C. Riziotis, “Study and optimization of tapered plasmonic waveguides for light nanofocusing,” *11th International Conference of Computational Methods in Sciences and Engineering, "Nonlinear Optics and Lasing in Complex Media", Athens, Greece; 20-23 March 2015* (Invited Oral Presentation).
- A. Petropoulou, K. Christodoulou, T. Krasia Christoforou, C. Riziotis, "Evaluation of fluorescent nanocomposite grids and membranes based on polymeric electrospun nanofibres towards ammonia sensing," *5th International Conference on Materials and Applications for Sensors and Transducers, IC-MAST, Mykonos, Greece, 27-30 September, 2015* (Oral)
- A. Petropoulou, G. Antonopoulos, G. Kakarantzas., D.W. Hewak, M.N. Zervas, C. Riziotis, "Engineering of composite metallic microfibers towards development of plasmonic devices for sensing applications," *5th International Conference on Materials and Applications for Sensors and Transducers, IC-MAST, Mykonos, Greece, 27-30 September, 2015* (Oral)

- A. Petropoulou, T.J. Gibson, E. Themistou, S. Pispas, C. Riziotis, "Amphiphilic block copolymer based photonic platform towards efficient protein detection," *SPIE COS Photonics Asia, Beijing, China, 12-14 October 2016* (Oral)
- A. Petropoulou, M.N. Zervas, C. Riziotis, "Optimized design of metal coated optical fiber tips with embedded plasmonic slot nano-resonators for maximum field enhancement," *SPIE COS Photonics Asia, Beijing, China, 12-14 October 2016* (Poster)
- A. Petropoulou, G. Antonopoulos, P. Bastock, G. Kakarantzas, C. Craig, D. Drikakis, D.W. Hewak, M.N. Zervas, C. Riziotis, "Design and Implementation of Fiber-Embedded Plasmonic Structures in Microwires," *Photonics & Electromagnetics Research Symposium (Progress In Electromagnetics Research Symposium), 41st PIERS, Rome, Italy, 17-20 June, 2019* (Invited)
- V. Aroni, G. Mountrichas, S. Pispas, A. Petropoulou, C. Riziotis, D. Hatziavramidis, “Study of irradiation time and laser flux for the synthesis of photocrosslinked PEG based hydrogels,” *3rd European Symposium of Photopolymer Science, Vienna, Austria; 9-12 September 2014* (Poster)